Phase-field Based Load-specific Structural Optimization and Experimental Validation of Porous Structures

Zur Erlangung des akademischen Grades eines
Doktors der Ingenieurwissenschaften (Dr.-Ing.)
von der KIT-Fakultät für Maschinenbau
des Karlsruher Instituts für Technologie (KIT)

genehmigte
Dissertation
von

M.Sc. Leonie Wallat

Tag der mündlichen Prüfung:	25. März 2025
Referent:	Prof. Dr. rer. nat. Britta Nestler
Korreferent:	Prof. Dr.-Ing. Frank Pöhler

Abstract

This study explores the potential and opportunities for load-specific optimization of porous structures, with a focus on phase-field-based optimization. Both simulation and experimental analysis are conducted to evaluate this approach. The study primarily concentrates on triply periodic minimal surfaces (TPMS), which are complex, mathematically definable cellular structures used across various application and research fields. Due to their versatility and potential for performance enhancement, these structures are primarily optimized for specific loading cases.

The first part of the investigation examines TPMS structures with varying porosity gradients. Building on this, a detailed shape optimization is carried out, utilizing a modified phase-field approach tailored to specific loading scenarios. In the subsequent part, a sheet-based gyroid structure is subjected to structural optimization. Following this, a 3D lattice structure undergoes similar optimization and is compared to TPMS structures. In the final part, the load-specific TPMS structures are experimentally investigated, with a focus on validating the phase-field based optimization.

Overall, this work demonstrates the potential and capabilities of phase-field based optimization for complex structures. It has been shown that load-specific phase-field optimization, not only preserves

characteristic properties but also enhances stiffness in the respective loading directions.

Kurzfassung

Diese Arbeit untersucht das Potenzial und die Möglichkeiten der belastungsspezifischen Optimierung zur Verbesserung der mechanischen Eigenschaften poröser Strukturen, wobei der Schwerpunkt auf einer phasenfeldbasierten Optimierung liegt. Zur Bewertung dieses Ansatzes werden sowohl numerische Simulationen als auch experimentelle Untersuchungen durchgeführt.
Diese Studie konzentriert sich hauptsächlich auf dreifach periodische Minimalflächen (TPMS), welche komplexe, mathematisch definierbare Zellstrukturen sind, die in verschiedenen Anwendungs- und Forschungsbereichen verwendet werden. Aufgrund ihrer Vielseitigkeit und ihres Potenzials zur Leistungssteigerung werden diese Strukturen für verschiedene Belastungsszenarien optimiert.
Im ersten Teil der Untersuchung werden TPMS-Strukturen mit variierenden Porositätsgradienten analysiert. Anschließend folgt eine detaillierte Formoptimierung, die auf einem modifizierten Phasenfeldansatz basiert. Der darauffolgende Teil widmet sich der strukturellen Optimierung verschiedener Zellstrukturen mittels der Phasenfeldmethode. Dabei werden Gyroid-Strukturen sowie 3D- Gitterstrukturen optimiert und anschließend mit den TPMS-Strukturen verglichen. Im letzten Abschnitt werden die belastungsspezifisch optimierten TPMS-Strukturen experimentell untersucht, wobei der

Schwerpunkt auf der Validierung der phasenfeldbasierten Optimierung liegt. Insgesamt demonstriert diese Arbeit das Potenzial und die Leistungsfähigkeit der phasenfeldbasierten Optimierung für komplexe poröse Strukturen. Es zeigt sich, dass die belastungsspezifische Phasenfeldoptimierung durch gezielte Volumenumverteilung nicht nur die charakteristischen Eigenschaften erhält, sondern auch die Steifigkeit in den jeweiligen Belastungsrichtungen erhöht.

Acknowledgments

Special thanks are due to my professors, my supervisor, and my colleagues:
Without my doctoral advisor, Prof. Dr. rer. nat. Britta Nestler, this work would not have been possible. The opportunity to conduct my research at her institute and her idea for this topic set the wheels in motion.
I am equally grateful to my doctoral father, Prof. Dr.-Ing. Frank Pöhler, who welcomed me from the beginning as if I were his own daughter. I could always count on his unwavering support with any questions or problems I encountered.
The regular meetings and discussions with my supervisor, Dr. Michael Selzer, significantly advanced my scientific development.
I would also like to extend my thanks to my colleagues. Without their support, the daily work would have been dull—thanks to them, mine was vibrant and enriching. Working at two institutes, I was fortunate to meet many wonderful colleagues on whom I could always rely. I am especially grateful to Dr. Andreas Reiter and Dr. Martin Reder, who patiently answered all my questions.
Last but not least, my deepest gratitude goes to my family. They have always believed in me and supported me during the moments when I felt like giving up. My father and siblings have consistently

encouraged me, and my special thanks go to my husband, Marcel, who I can always rely on without hesitation.

In memory of Werner, who sadly never got to read this document.

Karlsruhe, Oktober 2024 *Leonie Wallat*

Contents

1 Introduction

Sections of this chapter are based on the following publications: [1–7]

In engineering applications, lattice structures are often used to obtain lighter and high-strength materials. These structures are often copied from nature, which has produced efficient cell structures that are characterized by high stiffness and strength, such as the bones, woods, or teeth. These structures are also known as natural energy absorbers. A characteristic property of natural structures is the fact that they often have a complex shape with a density gradient [1, 2, 8, 9]. An example of a complex structures, that can be found in nature, are triply periodic minimal surfaces (TPMS).
TPMS-structures are three-dimensional cells that occur in nature in many forms, for example in butterfly wings [10] or on the skeletal plate of a sea urchin [11]. There are a variety of different structures, for example gyroid, Schwarz diamond and Schwarz primitive structures [12], which are defined by a mathematical periodic function and whose surfaces have a mean curvature of zero [2]. The mathematical formability of the structures allows for a high degree of flexibility in generating the digital model. Thus, it is possible to individually adjust the porosity or a porosity distribution through the structure, as well as the domain size and cell repetitions of a period cell [3].

The structures employed in this study are a single-cell sheet-based Schwarz diamond structure (hereinafter referred to as 'diamond'), a sheet-based gyroid structure (hereinafter referred to as 'gyroid'), and a sheet-based Schwarz primitive structure (hereinafter referred to as 'primitive'), see Figure 1.1 [3].

Figure 1.1: Examples of TPMS unit cells: a. Diamond; b. Gyroid; c. Primitive [3]

The corresponding formulas, as referenced in equations 1.1- 1.3, are as follows. The abbreviations $\tilde{x} = x/L_x$, $\tilde{y} = y/L_y$, and $\tilde{z} = z/L_z$ are used for the normalized coordinates, with respect to the unit cell lengths $\{L_x, L_y, L_z\}$ [13].

$$0 = \Big[\sin(2\pi\tilde{x})\sin(2\pi\tilde{y})\sin(2\pi\tilde{z}) + \sin(2\pi\tilde{x})\cos(2\pi\tilde{y})\cos(2\pi\tilde{z}) + \cos(2\pi\tilde{x})\sin(2\pi\tilde{y})\cos(2\pi\tilde{z}) + \cos(2\pi\tilde{x})\cos(2\pi\tilde{y})\sin(2\pi\tilde{z}) \Big]^2 - \delta^2 \tag{1.1}$$

$$0 = \Big[\sin(2\pi\tilde{x})\cos(2\pi\tilde{y}) + \sin(2\pi\tilde{y})\cos(2\pi\tilde{z}) + \cos(2\pi\tilde{x})\sin(2\pi\tilde{z}) \Big]^2 - \delta^2 \tag{1.2}$$

$$0 = \Big[\cos(2\pi\tilde{x}) + \cos(2\pi\tilde{y}) + \cos(2\pi\tilde{z}) \Big]^2 - \delta^2. \tag{1.3}$$

As mentioned before, the cell structure is characterized by the number of cell repetitions in the $x-, y-$, and $z-$direction and by the size of the unit cells $\{L_x, L_y, L_z\}$ [14]. In addition, the parameter δ controls the wall thickness of the structure [3, 15]. Thus, δ has an effect on the volume fraction (v^*) of the lattice structure [16]. According to [17, 18], the volume fraction (v^*) and the closely related parameter porosity Φ are defined in equation 1.4.

$$\Phi = (1 - v^*) \cdot 100[\%] \tag{1.4}$$

with

$$v^* = \frac{v}{v_\mathrm{s}}, \tag{1.5}$$

where v and v_s denote the volume of the pore structure and the volume of the solid structure, respectively [17, 18]. In the literature, v^* is also referred to as 'relative density' [18, 19]. As can be seen from equation (1.4), the higher the porosity, the thinner the cell walls [1]. In addition to their lightweight potential, these cell structures are characterized by unique properties and shapes that make them attractive for a wide range of engineering applications. For example, the high surface-to-volume ratio and the two-phase system are very preferable properties for the development of heat exchangers [20–22]. In particular, the work by Weihong Li et al. [21] has shown that a comparison between a printed circuit heat exchanger (PCHE) and

a heat exchanger with TPMS structures (Schwarz diamond and gyroid) shows both a higher thermal performance and a higher Nusselt number [21]. Furthermore, TPMS structures are of great interest in the field of tissue engineering, as their topological structure is similar to that of trabecular bone [2, 23].

Due to the promising and diverse applications of TPMS structures, various methods of structural optimization approaches are presented in the literature in order to further enhance specific material properties. The optimization is usually divided into three categories: size, shape, and topology [5, 24].

Shape optimization alters the geometry of the structure, whereas its topological characteristics remain unchanged. In contrast, topology optimization does also consider topological changes of the structure [25]. Thus, the resulting structure for topology optimization is independent of the initial structure, which is not the case for shape optimization [26]. However, some methods employed for topology optimization can also be used for shape optimization if the algorithm is stopped when topological changes start.

There are various objectives in optimization approaches, such as increasing the effective stiffness [27]. According to Gibson and Ashby [28], the mechanical properties of porous structures of the same topology are directly influenced by their porosity. They propose a correlation between the effective Young modulus and the relative density, which is known as Gibson-Ashby correlation. Besides the porosity, the mechanical properties are also strongly influenced by the topology of the structure [1, 14, 29].

Since the shape and topology play a crucial role in the stiffness, this work aims to optimize various cellular structures, with a particular

focus on the previously mentioned TPMS structures, using three different structural optimization approaches tailored to specific loading cases. The goal is to increase the stiffness of the structures in their respective loading directions. Particular emphasis is placed on the previously underexplored optimization of complex porous structures using a modified phase-field method. Subsequently, some of the optimized structures will be experimentally validated. The process is illustrated in Figure 1.2.

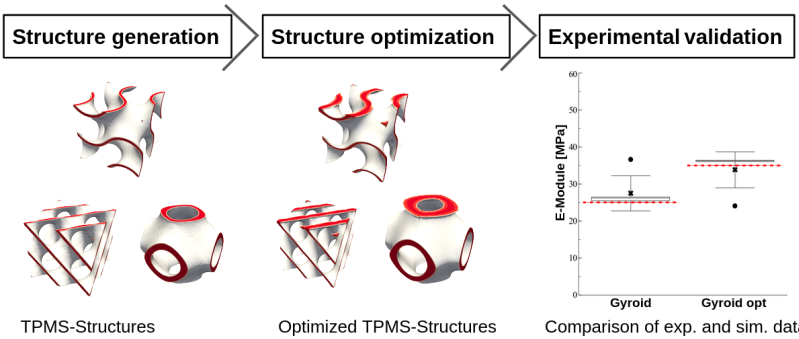

Figure 1.2: Outlined summary of the approach: 1. Structure generation, 2. Structural optimization, 3. Experimental validation.

The results are based on previously **published works [1–7]**.
In the following sections, the phase-field method, which serves as the foundation for shape optimization, is introduced in detail. Subsequently, two methods used to physically fabricate and test the simulated samples are described.
For structural optimization, three different approaches are examined in detail. The last two approaches are based on the previously introduced modified phase-field method.

1. **Manual Shape Optimization** (Chapter 4): In this approach, the porosity of the base structure is adjusted in such a way that both its distribution and, consequently, the loading profile are altered [2].

2. **Shape Optimization** (Chapter 5): In this method, the topology of the initial structure is preserved while performing shape optimization under specific load cases [3, 5].

3. **Structure Optimization** (Chapter 6): In this approach, the topology of the initial structure is first specifically adjusted according to the load requirements, followed by subsequent shape optimization [6, 7].

After the numerical analysis of the simulated structures, a selection of the structures is experimentally validated in Chapter 7 [1, 4, 6]. The primary objective of this experimental validation is to verify the efficacy of the relatively underexplored phase-field based optimization methods.

2 Methodology

The structure generation and the optimization procedure are based, unless otherwise specified, on the phase-field method and are implemented in the in-house software framework "Parallel Algorithms for Crystal Evolution in 3D" (Pace3D) [30], which is developed at the Institute for Digital Materials Science (IDM) of the Karlsruhe University of Applied Sciences, Germany and Institute for Applied Materials - Microstructure Modelling and Simulation (IAM-MMS) of Karlsruhe Institute of Technology (KIT).
As described in [2–7], the objective of Pace3D is to provide a package for large-scale multiphysics simulations, to solve coupled problems such as solidification, grain growth, mass and heat transport, fluid flow and mechanical forces (elasticity, plasticity), to name a few.
The use of dimensionless quantities enables a scale-independent representation of the results, so that the simulations are performed with a non-dimensionalization. With the help of a conversion table, physical quantities can be obtained from the results.
For the structural optimization of the structures, the framework for structural-mechanical simulations is employed for a given loading scenario, in which the geometry is varied to minimize or maximize the stored elastic energy. The phase-field based formulation depends

on its boundary conditions, as explained in more detail below. Depending on the boundary conditions, an increase in stiffness results in either energy minimization or maximization.
Accordingly, the subsequent section offers a general description of the phase-field method, followed by an analysis of the influence of the boundary conditions considered in this work on the objective function of the phase-field method. Therefore, the following subchapters are based on the methodological descriptions from the publications [3–7].

2.1 Phase-field (general)

As described in [2–7], the structural optimization is based on the phase-field method, which is a proven tool for problems such as phase transformations [31, 32] or structural mechanics in multigrain systems [33, 34] as well as porous structures [35]. For a problem with N phases, the geometry is described by the tuple $\phi = \{\phi_1, \ldots, \phi_N\}$ of phase variables $\phi_\alpha(x,t)$. These phase variables indicate whether phase α is present at a point x or not, corresponding to values of 1 or 0.
Instead of a sharp dividing surface between different phases, a smooth transition region is employed, resulting in a diffuse interface with finite thickness, where ϕ_α exhibits values between 0 and 1. Therefore, the phase variable ϕ_α can be regarded as the local volume fraction of phase α. This allows for the application of interpolation techniques at the diffuse interface, avoiding the need for body-fitted meshes in the numerical solution process [36]. The evolution of the phase-field is typically derived from a minimization of a

Ginzburg-Landau free energy density functional, which depends on the phase-field tuple and the corresponding gradients [37]. Typically, the free energy functional $\mathcal{F}(\phi, \nabla\phi) = \mathcal{F}_{\text{int}}(\phi, \nabla\phi) + \mathcal{F}_{\text{bulk}}(\phi, \dots)$ is additively split into an interfacial contribution $\mathcal{F}_{\text{int}}$ and a contribution of the bulk regions $\mathcal{F}_{\text{bulk}}$ [38, eq. (1)]. The latter contribution may arise from the mechanical strain energy, cf. [39]. If the elastic energy is the only bulk contribution, like it is the case for the present work, it is written as

$$\mathcal{F}_{\text{bulk}} = \mathcal{F}_{\text{el}}(\phi, \vec{u}) = \int_{\Omega} f_{\text{el}}(\phi, \vec{u}) \, \mathrm{d}V = V \bar{f}_{\text{el}}(\phi, \vec{u}) \tag{2.1}$$

The interfacial contribution is expressed as

$$\mathcal{F}_{\text{int}}(\phi, \vec{u}) = \int_{\Omega} f_{\text{grad}}(\phi, \nabla\phi) + f_{\text{pot}}(\phi) \, \mathrm{d}V \tag{2.2}$$

comprising a gradient energy density f_{grad} and a potential energy f_{pot}. Accordingly, the energy functional for the subsequent analysis is given by:

$$\mathcal{F}(\phi, \vec{u}) = \mathcal{F}_{\text{int}}(\phi, \nabla\phi) + \mathcal{F}_{\text{el}}(\phi, \vec{u}) + F_{vol}(\phi) \tag{2.3}$$

An additional positive contribution $\mathcal{F}_{vol}$ is incorporated which ensures the volume preservation. The free energy minimization requires the variation of $\mathcal{F}$ to vanish, thus $\delta\mathcal{F} = 0$. Variational calculus can be used to obtain governing equations for all occurring solution variables. With respect to the phase-field, an additional ansatz regarding the relaxation to equilibrium allows obtaining phase-field evolution equations. Thereby, one way to derive evolution equations is to use an Allen-Cahn approach [40] which can be formulated with

a constraint of volume preservation of phases [41].
An Allen-Cahn type phase-field method is employed in this work, unless otherwise specified.

2.2 Modified phase-field method for structural optimization

As previously described, for the phase-field based load-specific optimization, the objective of the functional is not only to minimize the phase-field energy $\mathcal{F}_{\text{int}}$ but also to account for the strain energy $\mathcal{F}_{strain}$. The strain energy $\mathcal{F}_{strain}$ is defined as follows:

$$\mathcal{F}_{\text{el}}(\phi, u(\phi)) := \mathcal{F}_{strain}(\phi, u(\phi)) = \int_{\Omega} \frac{1}{2} C(\phi)[\epsilon(u(\phi))] \cdot \epsilon(u(\phi)) dx \tag{2.4}$$

The stress contribution u and strain ϵ are dependent on the solution of the elasticity equation with respect to ϕ. Consequently, the choice of loading cases is crucial for the energy development. In the following, the different loading cases considered in this study are distinguished. In the first case, the structure loses its periodicity in the loading direction. In the other two cases, the periodicity in the loading directions is maintained. Both boundary conditions of average strain $\bar{\epsilon}$ and average stress $\bar{\sigma}$ are considered for each case.

2.2.1 Boundary condition: non-periodic in all direcitons

In the loading case depicted in Figure 2.1 and discussed in 5.1 (based on publication [3]), a stress $\sigma \cdot n = t$ is applied to the upper boundary in one direction, and a displacement of $u = 0$ is set on the lower boundary. The side boundaries have periodic boundary conditions.

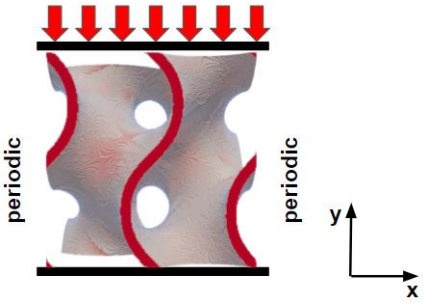

Figure 2.1: Representation of the stress boundary condition, according to the publication [3]

Based on the previously stated assumptions, the following stress equilibrium conditions (Eqc) are derived:

$$Eqc = \begin{cases} -\nabla \cdot (C(\phi)[\epsilon]) = 0 & \text{weight force vector} \\ \vec{u} = 0 & \text{displacement on the lower boundary } \Gamma_u \\ C(\phi)[\epsilon] \cdot n = t & \text{stress on the upper boundary } t = \sigma \cdot n \end{cases} \tag{2.5}$$

The first condition specifies that the elastic stress depends on the phase-field variable ϕ. Additionally, the adjustment of the phase

ϕ, as carried out within the optimization process, must be in equilibrium with the elastic tensor. This equilibrium condition applies similarly to the subsequent two boundary conditions in subchapter 2.2.2 and 2.2.3.
For the following analysis, it is necessary to consider the directional derivative of the objective function 2.3 with respect to changes in $\delta\phi$. This consideration must also be included in the equilibrium condition, such that $\delta u = \delta u(\phi)$ and $\delta\epsilon = \epsilon(\delta\phi) = \epsilon(u(\delta\phi))$ hold. The corresponding derivative of the local equilibrium condition for the force vector is given by:

$$\delta G g w = \begin{cases} -\nabla \cdot ((C'(\phi)\delta\phi)[\epsilon] + C(\phi)[\delta\epsilon]) = 0 & \text{weight force vector} \\ \delta\vec{u} = 0 & \text{on the boundary } \Gamma_u \\ (C'(\phi)\delta\phi)[\epsilon] \cdot n + C(\phi)[\delta\epsilon] \cdot n = 0 & \text{under constant boundary stress} \end{cases} \tag{2.6}$$

Similarly, the change in u and ϵ with respect to ϕ from $\mathcal{F}_{strain}$ 2.4 must be examined. By differentiating, we obtain:

$$\delta\mathcal{F}_{strain} = \int_\Omega \frac{1}{2}(C'(\phi)\delta\phi)\,[\epsilon] \cdot \epsilon dx + \int_\Omega C(\phi)\,[\epsilon] \cdot \delta\epsilon dx, \tag{2.7}$$

While the first term of Equation 2.7 represents the driving force for elasticity, the second term, with its dependencies, presents a challenge.

This challenge is addressed by considering the first equilibrium condition in Equation 2.6 and multiplying it by the displacement field u

$$0 = \int_\Omega [-\nabla \cdot ((C'(\phi)\delta\phi)[\epsilon] + C(\phi)[\delta\epsilon])] \cdot u dx \tag{2.8}$$

The subsequent partial integration results in:

$$\begin{aligned} 0 = \\ \int_\Omega ((C'(\phi)\delta\phi)[\epsilon] + C(\phi)[\delta\epsilon]) \cdot \epsilon(u) dx - \\ \int_{\delta\Omega} [(C'(\phi)\delta\phi[\epsilon] + C(\phi)[\delta\epsilon] \cdot n] \cdot u ds \end{aligned} \tag{2.9}$$

The boundary integral $\int_{\delta\Omega}$ at the lower boundary is zero due to the previously specified boundary condition that the displacement is zero there. The integral at the lateral boundaries also vanishes due to periodicity. At the upper boundary, the prefactor of u vanishes by the third equation in 2.6. Exploiting the symmetry, this allows the following transformation:

$$\int_\Omega C(\phi)[\epsilon] \cdot \delta\epsilon dx = \int_\Omega C(\phi)[\delta\epsilon] \cdot \epsilon dx = -\int_\Omega (C'(\phi)\delta\phi)[\epsilon] \cdot \epsilon dx \tag{2.10}$$

Back to the derivation problem of the strain energy in equation 2.7: here it is now recognizable from the equation just transformed that the unpleasant 2nd term can be eliminated by using the equation 2.10.

$$\delta\mathcal{F}_{strain} = \int_\Omega \frac{1}{2}(C'(\phi)\delta\phi)\,[\epsilon]\cdot\epsilon dx - \int_\Omega (C'(\phi)\delta\phi)[\epsilon]\cdot\epsilon dx, \quad (2.11)$$

$$= -\int_\Omega \frac{1}{2}(C'(\phi)\delta\phi)\,[\epsilon]\cdot\epsilon dx, \quad (2.12)$$

This transformation shows that the optimization with the previously described boundary conditions corresponds to the driving force of the phase-field method with sign change.

2.2.2 Boundary condition: macro_strain

In contrast to the previous subchapter, a strain is specified for the load case considered here, which leads to an increase in elastic energy if the stiffness is increased as desired. Furthermore, the periodicity keeps constant in all room directions. The loading case considered and described here is based on the publication [5] and is practically illustrated in Chapter 5.2 using porous structures. This corresponds to a minimization of $-\mathcal{F}_{strain}$, accordingly the energy functional changes as follows:

$$\mathcal{F}(\phi, u(\phi)) = \mathcal{F}_{\text{int}}(\phi, u(\phi)) - \mathcal{F}_{strain}(\phi, u(\phi)) + F_{vol}(\phi) \quad (2.13)$$

As before, the gradient of $\mathcal{F}(\phi, u(\phi))$ with respect to changes in ϕ is sought. In this case of load optimization, the boundary condition *periodic_ macro* is considered. The idea behind this is that the

periodicity is maintained despite an imposed macroscopic average strain. This corresponds to the following equilibrium conditions:

$$\begin{cases} -\nabla \cdot C(\phi)[\epsilon] = 0 & \text{in } \Omega \\ u_{upper} = u_{lower} + \bar{\epsilon} \cdot x & \text{on } \delta\Omega \end{cases} \tag{2.14}$$

Here, u_{upper} and u_{lower} correspond to the respective opposite edges/sides, and $\bar{\epsilon}$ represents the mean prescribed strain that is applied.
To resolve the issue that periodicity is theoretically lost due to the application of a macroscopic strain $\bar{\epsilon} \cdot x$, $\widetilde{u} = u - \bar{\epsilon} \cdot x$ is introduced. As a result, the boundary condition $\widetilde{u}_{upper} = \widetilde{u} - \bar{\epsilon} \cdot x = (u_{lower} + \bar{\epsilon} \cdot x) - \bar{\epsilon} \cdot x = u_{lower}$ becomes truly periodic. Additionally, the following relationship applies accordingly:

$$\epsilon(u) = \underbrace{\epsilon(\widetilde{u})}_{:=\widetilde{\epsilon}} + \bar{\epsilon} \tag{2.15}$$

After substituting $\widetilde{u}$ and the corresponding relationship from Equation 2.15 into the equilibrium condition 2.14, the following result is obtained:

$$\begin{cases} -\nabla \cdot C(\phi)[\epsilon(\widetilde{u}) + \bar{\epsilon}] = -\nabla \cdot C(\phi)[\widetilde{\epsilon} + \bar{\epsilon}] = 0 & \text{on } \Omega \\ \widetilde{u} \text{ periodic} & \text{on } \delta\Omega \end{cases} \tag{2.16}$$

Accordingly, by substituting into the strain energy 2.4, the following strain energy $\widetilde{\mathcal{F}}_{strain}$ is obtained for the problem under consideration:

$$\widetilde{\mathcal{F}}_{strain}(\phi, \widetilde{u}(\phi), \bar{\epsilon}) = \int_{\Omega} \frac{1}{2}(C(\phi)[\epsilon(\widetilde{u}(\phi)) + \bar{\epsilon}] \cdot (\epsilon(\widetilde{u}(\phi)) + \bar{\epsilon})dx \tag{2.17}$$

In this case, one has the following relation of the solution $\widetilde{u}$ with the objective function:

$$\begin{aligned} \widetilde{u} = \widetilde{u}(\phi) \in \operatorname{argmin}_{v,periodic} \widetilde{\mathcal{F}}_{strain}(\phi, v) = \\ \operatorname{argmin}_{v,periodic} \int_{\Omega} \frac{1}{2}(C(\phi)[\epsilon(v) + \bar{\epsilon}] \cdot (\epsilon(v) + \bar{\epsilon})dx \end{aligned} \tag{2.18}$$

This follows by differentiating $\widetilde{\mathcal{F}}_{strain}$ with respect to $\widetilde{u}$ and an integration by parts. When considering the equilibrium condition of the system, taking into account the elastic deformations and an externally applied macroscopic strain,

$$\int_{\Omega} C(\phi)[\epsilon(\widetilde{u}) + \bar{\epsilon}] \cdot \epsilon(\delta\widetilde{u})dx = \tag{2.19}$$

$$\int_{\Omega} (-\nabla \cdot C(\phi)[\epsilon(\widetilde{u}) + \bar{\epsilon}]) \cdot \delta\widetilde{u}dx + \int_{\delta\Omega} (C(\phi)[\epsilon(\widetilde{u}) + \bar{\epsilon}] \cdot n) \cdot \delta\widetilde{u}ds = 0 \tag{2.20}$$

where the boundary integral $\int_{\delta\Omega}(\sigma \cdot n) \cdot \delta\widetilde{u} ds$ vanishes due to periodicity, leading to the term being simplified as follows:

$$\int_{\Omega} C(\phi)[\epsilon(\widetilde{u}) + \bar{\epsilon}] \cdot \epsilon(\delta\widetilde{u}) dx = \int_{\Omega} (-\nabla \cdot C(\phi)[\epsilon(\widetilde{u}) + \bar{\epsilon}]) \cdot \delta\widetilde{u} dx = 0 \tag{2.21}$$

Since the derivative $\tilde{\mathcal{F}}_{strain}$ vanishes in all directions for all periodic $\delta\tilde{u}$ and the change $\delta\tilde{u}(\delta\phi)$ is necessarily periodic due to the imposed boundary conditions, the directional derivative of $\delta\tilde{u}(\delta\phi)$ disappears.

It follows that

$$\frac{d}{d\phi}\mathcal{F}_{strain}(\phi, u(\phi)) = \frac{\delta}{\delta\phi}\mathcal{F}_{strain}(\phi, u(\phi)) \tag{2.22}$$

This results in a correspondence between the total and partial derivatives.

$$\begin{aligned} \frac{d}{d\phi}\mathcal{F}(\phi, u(\phi)) = \\ \frac{d}{d\phi}\mathcal{F}_{int}(\phi, u(\phi)) - \frac{\delta}{\delta\phi}\mathcal{F}_{strain}(\phi, u(\phi)) + F'_{vol}(\phi) = \\ \frac{d}{d\phi}\mathcal{F}_{\text{int}}(\phi, u(\phi)) - \frac{1}{2}C'(\phi)[\epsilon] \cdot \epsilon + F'_{vol}(\phi) \end{aligned} \tag{2.23}$$

From this derivation, it becomes clear that, unlike in the previous section, differentiating the function does not result in a sign change due to the boundary conditions chosen here. Therefore, the same driving force can be used for both cases, even though in the former

one, the strain energy is minimized due to the sign change in the derivative, while in our current case, the strain energy is maximized since there is no sign change in the differentiation process.
In the following subsection, the mean stress is specified instead of the mean strain, while maintaining periodicity in all spatial directions.

2.2.3 Boundary condition: macro_stress

The stress boundary condition considered here applies the mean stress instead of the mean strain. This subsection is based on the publications [6, 7]. Accordingly, a displacement field u and a stress field σ are generated, which should satisfy the condition of periodicity and, additionally, for a given $\bar{\sigma}$, the following holds:

$$\frac{1}{|\Omega|}\int_{\Omega}\sigma(\phi, u(\phi))dx = \bar{\sigma} \tag{2.24}$$

In this approach, the mean stress is generated indirectly through the selection of the mean strain via the displacement boundary conditions. This is done by iteratively solving the elastic equilibrium for a given $\bar{\epsilon}^{(n)}$ and then updating it for the next time step $(n+1)$ according to:

$$\bar{\epsilon}^{(n+1)} = \bar{\epsilon}^{(n)} + (\bar{C}(\phi))^{-1} \cdot (\bar{\sigma} - \frac{1}{|\Omega|}\int_{\Omega}\sigma(\phi, u^{(n+1)})dx) \tag{2.25}$$

until the resulting mean stress has converged to the desired value.

$\bar{\epsilon}^{(n)}$ is initially initialized from the initial value of $(\bar{C}(\phi))^{-1}\bar{\sigma}$.
Since the mean stress is determined by choosing the mean strain, as described in the previous chapter, the driving force is selected as the elastic energy contribution $\tilde{\mathcal{F}}_{strain}$. To account for the new dependencies, the displacement field is decomposed into $\tilde{u}$ and $\bar{\epsilon} \cdot x$ for the further analysis, leading to the functional from equation 2.17 now depending additionally on $\bar{\epsilon}$ with respect to ϕ, as $\tilde{\mathcal{F}}_{strain}(\phi, \tilde{u}(\phi), \bar{\epsilon}(\phi))$:

$$\tilde{\mathcal{F}}_{strain}(\phi, \tilde{u}(\phi), \bar{\epsilon}(\phi)) = \tag{2.26}$$

$$\frac{1}{2} C(\phi)[\epsilon(\tilde{u}(\phi) + \bar{\epsilon}(\phi)] \cdot (\epsilon(\tilde{u}(\phi)) + \bar{\epsilon}(\phi)) dx \tag{2.27}$$

The total derivative of $\tilde{\mathcal{F}}_{strain}$ depends first on the partial derivative with respect to ϕ , which — as in the previous case — leads to the standard phase-field term, the local density $\frac{1}{2} C'(\phi)[\epsilon] \cdot \epsilon$.
The second dependency, through $\tilde{u} = \tilde{u}(\phi)$ and $\bar{\epsilon} = \bar{\epsilon}(\phi)$, leads to the term $\int_\Omega C(\phi)[\epsilon(\tilde{u}) + \bar{\epsilon}] \cdot (\epsilon(\delta\tilde{u}) + \delta\bar{\epsilon}) dx$. In contrast to the previous case, this term does not vanish, but instead results in a sign reversal. This can be explained as follows:

By differentiating with respect to the parameters $\phi, \tilde{u}$ and $\bar{\epsilon}$ in the equilibrium condition $-\nabla \cdot (C(\phi)[\epsilon(\tilde{u}) + \bar{\epsilon}]) = 0$, the following expression is obtained:

$$-\nabla \cdot (C(\phi)[\epsilon(\delta\tilde{u}) + \delta\bar{\epsilon}]) - \nabla \cdot ((C'(\phi)\delta\phi)[\epsilon(\tilde{u}) + \bar{\epsilon}]) = 0 \quad (2.28)$$

By multiplying with $\tilde{u}$ and subsequently integrating, the following results:

$$\int_\Omega C(\phi)[\epsilon(\delta\tilde{u}) + \delta\bar{\epsilon}] \cdot \epsilon(\tilde{u})dx = -\int_\Omega (C'(\phi)\delta\phi)[\epsilon(\tilde{u}) + \bar{\epsilon}] \cdot \epsilon(\tilde{u})dx \quad (2.29)$$

as the boundary terms disappear during partial integration due to periodicity.
Furthermore, differentiating the condition in equation 2.24 yields:

$$\int_\Omega C(\phi)[\epsilon(\delta\tilde{u}) + \delta\bar{\epsilon}]) + (C'(\phi)\delta\phi)[\epsilon(\tilde{u}) + \bar{\epsilon}]dx = 0 \quad (2.30)$$

By subsequently multiplying with the constant $\bar{\epsilon}$, it follows that:

$$\int_\Omega C(\phi)[\epsilon(\delta\tilde{u}) + \delta\bar{\epsilon}] \cdot \bar{\epsilon}dx = -\int_\Omega (C'(\phi)\delta\phi)[\epsilon(\tilde{u}) + \bar{\epsilon}] \cdot \bar{\epsilon}dx \quad (2.31)$$

To obtain the expression for the driving force, one can first make use of the symmetry properties of $C(\phi)$ to express the contributions of the changes in $\tilde{u}(\delta\phi)$ and $\bar{\epsilon}(\delta\phi)$ to the strain energy as

$$\int_\Omega C(\phi)[\epsilon(\tilde{u})+\bar{\epsilon}])\cdot(\epsilon(\delta\tilde{u})+\delta\bar{\epsilon})dx = \int_\Omega (C(\phi)[\epsilon(\delta\tilde{u})+\delta\bar{\epsilon}]\cdot(\epsilon(\tilde{u})+\bar{\epsilon})dx. \tag{2.32}$$

In a second step, one can then eliminate the contributions due to $C(\phi)[\epsilon(\delta\tilde{u}) + \delta\bar{\epsilon}] \cdot \epsilon(\tilde{u})$ and $C(\phi)[\epsilon(\delta\tilde{u}) + \delta\bar{\epsilon}] \cdot \bar{\epsilon}$ from the expression in equations 2.29 and 2.31, leading to

$$\begin{aligned}\int_\Omega C(\phi)[\epsilon(\delta\tilde{u}) + \delta\bar{\epsilon}]) \cdot \epsilon(\tilde{u})dx + \int_\Omega (C(\phi)[\epsilon(\delta\tilde{u}) + \delta\bar{\epsilon}] \cdot \bar{\epsilon})dx = \\ - \int_\Omega (C'(\phi)\delta\phi)[\epsilon(\tilde{u}) + \bar{\epsilon}] \cdot \epsilon(\tilde{u}) \cdot \bar{\epsilon}dx - \int_\Omega (C'(\phi)\delta\phi)[\epsilon(\tilde{u}) + \bar{\epsilon}] \cdot \epsilon(\tilde{u})dx = \\ - \int_\Omega (C'(\phi)\delta\phi)[\epsilon(\tilde{u}) + \bar{\epsilon}] \cdot (\epsilon(\tilde{u}) + \bar{\epsilon})dx\end{aligned} \tag{2.33}$$

Consequently, the second part of the differentiation problem results in a factor of -2 of the contribution from the partial derivative, leading to the conclusion that, as in the first considered cases, the total derivative is given by the negative of the partial derivative:

$$\frac{d}{d\phi}\tilde{F}_{strain}(\phi, \tilde{u}(\phi), \bar{\epsilon}(\phi)) = -\frac{\delta}{\delta\phi}\tilde{F}_{strain}(\phi, \tilde{u}(\phi), \bar{\epsilon}(\phi)) \tag{2.34}$$

This leads, after returning to the original unknown u, to:

$$\frac{d}{d\phi}\tilde{F}_{strain}(\phi, u(\phi)) = -\frac{d}{d\phi}\tilde{F}_{strain}(\phi, u(\phi)) = -\frac{1}{2}C'(\phi)[\epsilon(u)] \cdot \epsilon(u). \tag{2.35}$$

For the structural optimization process, the boundary condition "macro_stress" described herein is integrated with the "hole nucleation" approach presented in Chapter 6.

2.2.4 Hole Nucleation

The process of "hole nucleation" is used for targeted, load-specific topology modification, as described in publications [6, 7]. Here is the idea to remove material from less stresses regions. For the stress-specific volume reduction, material is removed from regions where the von Mises stress, σ_{vM}, of the loaded initial lattice structure falls below a certain percentage value ρ_{Nuc}. Firstly, the initial structure is discretized using a Cartesian grid and linear elastic simulations to mechanical equilibrium are performed under the considered loading conditions and thus the stress field is obtained. The maximum $\max(\sigma_{\mathrm{vM}})$ of the von Mises stress across the entire simulation domain of the initial structure is determined. Nucleation is considered if

$$\mathrm{vM} < \rho_{\mathrm{Nuc}} \max(\mathrm{vM}) \tag{2.36}$$

holds. Thus in cells of the computational grid, where the von Mises stress is below the threshold value $\rho_{\mathrm{Nuc}} \max(\mathrm{vM})$ the porous phase

is assigned by setting the phase-field values $\phi_p = 0$ and $\phi_s = 1$. The topology adjustment of the structure is carried out in a single step. Since volume preservation is not enforced in this step, a stress-specific volume reduction of the structure occurs.

The phase-field based optimization approaches described above are also experimentally validated. The results of the experimental validation are summarized in the separate chapter 7.

2.3 Experimental validation

For the experimental validation compression tests are conducted. The "Inspekt 200" machine from *Hegewald & Peschke* is used for this purpose. The testing speeds and the dimensions of the test specimens comply with international standards and vary depending on the material of the manufactured samples. In this study, both porous test specimens made of metal and plastic are used.
For the metallic porous structures discussed in Chapter 7.1.1, the sample dimensions and test conditions follow the ISO 13314:2011 standard [42]. For the components made of plastic, the international ASTM D1621 standard [43] is used as a reference. Detailed information on the sample sizes and test settings used is provided in the relevant chapters.

Before the structures can be experimentally validated, the fabrication of the specimens is essential. The investigations into the fabrication methods employed in this study are described in detail

in the following chapter, where two distinct methods are introduced, varying according to the selected material.

3 Structure manufacturing

The structure generation for the experimental validation of the structurally optimized samples was conducted using either a metallic material or a polymer. Depending on the material, the manufacturing process and the corresponding standard for sample testing are different.
For the manufacturing of polymer-based samples, the stereolithography (SL) process was used, while the microcasting process was employed for the metallic samples. The individual processes will be discussed in more detail below.

3.1 Stereolithography Apparatus

Stereolithography Apparatus (SLA) is an additive manufacturing process that was patented by Charles Hull in 1984. In the stereolithography (SL) process, a part is created by computer-controlled laser curing of a resin, with layer thicknesses typically ranging between 25-100μm.
Generally, a CAD file is used for stereolithography, which is then sliced into virtual layers that can be used in the fabrication process and transmitted to the stereolithography apparatus (SLA). The final part creation is based on the curing of a liquid resin (see figure

3.1.3) through photo-initiated polymerization. This polymerization is triggered by a computer-controlled laser beam (see figure 3.1.2) and mirrors (see figure 3.1.1), or a digital light projector with a computer-driven build platform. The corresponding layer is projected onto the surface of the resin. Subsequently, the platform (see figure 3.1.4) is moved upwards by the thickness of the cured layer. This cycle is repeated numerous times until the desired object is formed. A simplified diagram of a stereolithography apparatus is shown in Figure 3.1 [44, 45].

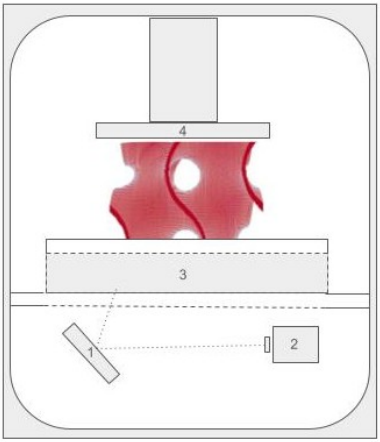

Figure 3.1: Schematic representation of stereolithography apparatus (SLA), based on a gyroid structure: 1. Mirror; 2. Laser; 3. Resin; 3. Inverted Bed

For the production of metallic samples, the microgravity technique was employed.

3.2 Microcast processing

This chapter is based on the publication: [1]

In addition to additive manufacturing processes such as selective laser melting (SLM) or selective laser sintering (SLS), generative microcast processing can also be used to manufacture complex components. This method offers the possibility to produce primitive and very complex structures, such as TPMS structures, with a wall thickness of at least 0.12 mm in large quantities, in a weight range between 0.01 g to approximately 30 g. Furthermore, it is suitable for the development and prototype phase of a product, as different geometry, design and material variants of a product can be produced in one manufacturing step. The special feature is that the original metal alloy such as copper-based, aluminum and zinc alloys or steels are used for the cast processing. The manufacturing steps of the cast processing are shown in Figure 3.2, using a gyroid structure.

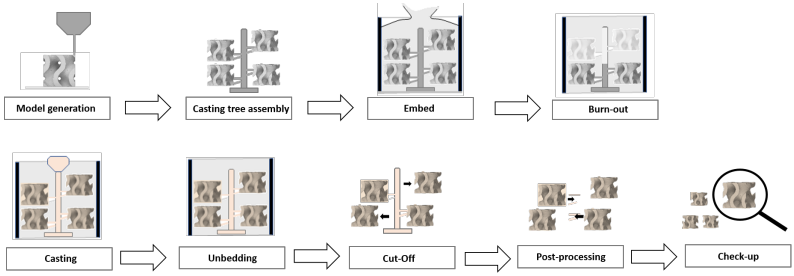

Figure 3.2: Schematic representation of microcast processing, based on a gyroid structure [1]

First, wax models are produced, using a 3D printing process, which are then attached to a casting tree. In the further manufacturing process, the casting tree with the added components serves as a lost model, in which the structures are embedded in a ceramic mass (in our case gypsum) and burnt out. Then, molten metal is poured into the negative molds, created by the firing process. After the destruction of the ceramic mold, the metal parts can be removed. To achieve complete removal of the investment material in the narrow corridors of the TPMS structure, the structure is first blasted with water. Then the parts are placed in an ultrasonic bath. These two steps are repeated until no investment material is left.

This manufacturing process is utilized throughout the study to produce the test specimens for the experimental validation of the manually shape-optimized gyroid structures with gradients. The procedure for manual shape optimization is elaborated upon in the subsequent Chapter 4.

4 Manual Shape Optimization

For the manual shape optimization, gyroid structures are adjusted by modifying parameters such as cell size and porosity during the generation phase. In this context, we specifically focus on adjusting the porosity distribution.

4.1 Computational design and characterisation of gyroid structures with different gradient functions for porosity adjustment

This chapter is based on the publication: [2]

4.1.1 Computational design

Before mechanical simulations of the structures can be performed, the digital structures are created on the basis of a spatial algorithm. For the structure creation, a MatLab [46] source was programmed, which enables the creation of TPMS structures with and without

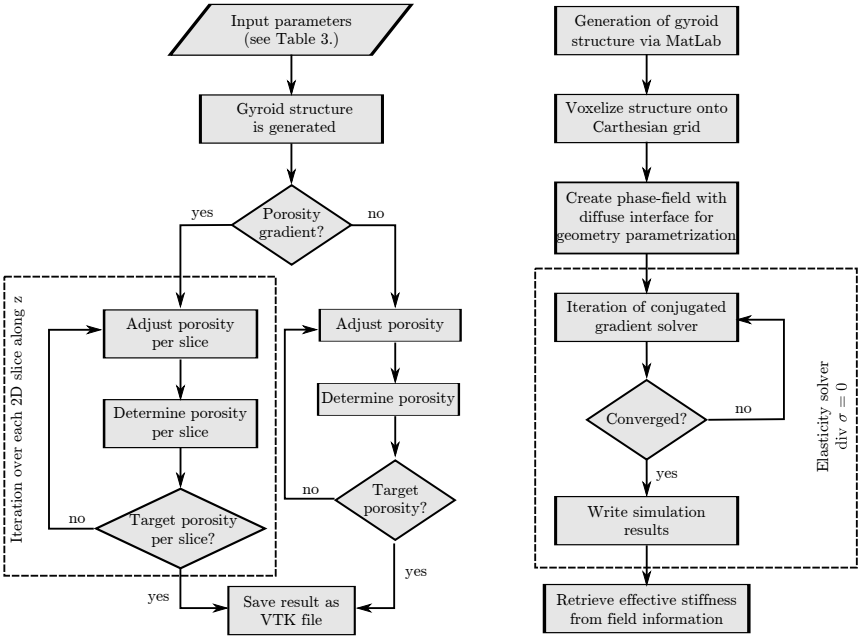

Figure 4.1: Schematic representation of the computational design of the structures. Generation of the gyroid structures in the MatLab program (left) and the workflow for the mechanical simulations with PACE3D (right).

gradients. The aim of the MatLab program is to create gyroid structures with adjustable porosities and definable porosity gradients, using mathematical functions. The TPMS structures are stored in vtk files, while the further preprocessing of the structures as well as the simulations are realized with the simulation framework PACE3D [30], which is presented in Chapter 2.

The corresponding flowchart from the creation of the structures in the MatLab program to the mechanical simulation is summarized in Figure 4.1.

4.1.2 Structure generation

The input parameters used for structure generation, along with the corresponding algorithm, will be examined separately in the following sections.

4.1.2.1 Input parameters

The MatLab program offers the possibility to create structures with constant and graded porosity. Table 4.1 lists and briefly describes the required input parameters for the structure generation, while the individual parameters and their influence are discussed more specifically in the following.

Table 4.1: Input parameters of the MatLab program and their function for the creation of a gyroid structure.

Input parameter	Function
num_{x}	Number of unit cells to be repeated in
num_{y}	the x-, y- and z-direction
num_{z}	
$unitCellSize$	Size of the unit cells (in mm)
n_{steps}	Resolution of the unit cell
Φ_{max}	Maximum and minimum porosity of
Φ_{min}	the cell
$func$	Gradient function
$grad$	With/without gradient function (1,0)
$delta$	Tolerance range

The input parameters num_{x}, num_{y} and num_{z} specify the number of unit cells to be repeated in the corresponding direction, while the parameter $unitCellSize$ defines the physical dimension of the created gyroid unit cell. By multiplying $unitCellSize$ with the input parameters num_{x}, num_{y} and num_{z}, the quantities L_{x}, L_{y} and L_{z} of

equation (1.2) are obtained, which also represent the total domain size of the resulting structure in physical dimensions. The parameter n_{steps} defines the number of voxels that are used to discretize the gyroid in all directions of one spatial unit cell.
With Φ_{min} and Φ_{max}, the range of the minimum and maximum porosity is defined. In the MatLab program, the porosity is specified in the range between [0;1], which represents the more commonly used expression of 0 % and 100 % for the porosity. When creating a gyroid structure with a constant overall porosity, the value from Φ_{max} is used. The porosity function is defined with the parameter *func*. The polynomial degree of the gradient function can be selected between 0 and 2, corresponding to a constant (0), a linear (1) and a quadratic (2) representation. The input parameter *grad* determines whether the gyroid structure is generated with or without gradient by the integer values 1 and 0, respectively. Per default, the gradient occurs in z-direction.
The parameter *delta* is mainly responsible for the iterative adjustment of the actual porosity to the target porosity. A tolerance range is defined that describes the maximum permissible deviation between the actual porosity of the current layer and the target porosity. For instance, if the parameter is set to a value of 0.02, this corresponds to a deviation of the actual data of 2 %, compared to the target porosity function. The smaller the number of this parameter, the more accurate and longer the program takes to calculate. The target porosity per cell layer is calculated by the gradient function.
Figure 4.2 shows four different gyroid unit cell structures with a cell size of 2.5 mm, which is generated with 200 steps and a *delta* parameter of 0.02. Figures 4.2.a and 4.2.d illustrate a gyroid unit cell with a constant porosity of 0.8 (a) and 0.4 (d). By looking at

the two structures, the influence of the porosity on the cell thickness becomes evident. The higher the porosity, the thinner the wall thickness. The structures 4.2.b and 4.2.c refer to different gradient functions: linear (b) and quadratic (c) functions. The structures are in a porosity interval between 0.4 and 0.8.

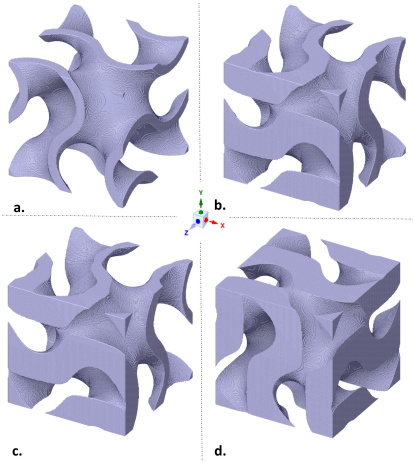

Figure 4.2: Unit cell of the gyroid structure; gradient with (**a**) constant function, with a porosity of 0.8; (**b**) linear function, with a porosity from 0.4 to 0.8; (**c**) quadratic function, with a porosity from 0.4 to 0.8; (**d**) constant function, with a porosity of 0.4.

4.1.2.2 Algorithm

In the algorithm, the porosity is adjusted step by step. First, the total volume of an initially generated cell structure is calculated as a starting point, while the discrete voxel values in the domain vary between -1 and 1, according to equation 1.2. Once the gradient function is selected, the superimposition begins in an iterative

process. Three encapsulated for-loops are used to iterate over the spatial domain, and a while-loop is responsible for adjusting the porosity to the target porosity. The adjustment is made by applying a threshold with values between -1 and 1, which divides the domain into structure space and tunnels. The specified tolerance limits are used as the termination criterion of the while loop. In this way, the target porosity for each 2D layer of the 3D structure can be adjusted according to the gradient function. If no gradient is selected, the porosity adjustment is not applied per layer but to the entire cell structure. For the definition of the gradient function (Φ_{target}), a choice between the following three functions is possible so far:

Constant function:

$$\Phi_{\text{target}} = \Phi_{\text{max}} \tag{4.1}$$

Linear function:

$$\Phi_{\text{target}} = -\frac{\Phi_{\text{max}} - \Phi_{min}}{n_{\text{steps}_z}} \cdot q + \Phi_{\text{max}} \tag{4.2}$$

Quadratic function:

$$\Phi_{\text{target}} = -\frac{\Phi_{\text{max}} - \Phi_{min}}{(n_{\text{steps}_z} - 3)^2} \cdot (q-2)^2 + \Phi_{\text{max}} \tag{4.3}$$

The constant function calculates a structure with a constant porosity along each spatial direction. For the linear cell gradient, a linear function with the usual linear structure $y = a * x + b$ is used. The first part of the equation calculates the stepwise increase of the cell

volume in each cell level (or the decrease of the porosity). Here, the calculation depends on the number of discrete points (n_{steps}) in whose direction the gradient is imposed. In this case, the gradient extends into the z-direction. The second part of the formula is used to determine the initial porosity Φ_{max}. In the first layer, the structure has the porosity of Φ_{max}, which is gradually decreased until the final porosity Φ_{min} is reached. q is the index parameter for the outermost for-loop and at the same time the spatial position of the current 2D layer.
For the quadratic cell gradient, a quadratic function of the structure $y = a * x^2 + b * x + c$ is used with $(b = 0)$. As with the linear function, a stepwise decrease in the porosity (increase of the cell volume) is determined at each cell level, except that the decrease should be quadratic. Since the quadratic gradient is defined as an inverted parabola with an offset on the y-axis, at the level of maximum porosity, the gyroid structure with a quadratic gradient is thickened more slowly than those with a thickening linear structure, as can be seen in Figure 4.3.
In Figure 4.3, the three different gradients (constant, linear and quadratic) are compared with their target and actual values of a single-cell gyroid structure. In each case, 50 actual and 50 target values per porosity function (input parameter: $n_{steps} = 50$) are mapped over 'Cell size' [5 mm], in the z-direction [x-axis], and 'Porosity' [y-axis]. The maximum porosity is 0.6 and the minimum porosity is 0.4. The actual values are an approximation of the target values. As already mentioned, the fit of the objective function mainly depends on the *delta* parameter.

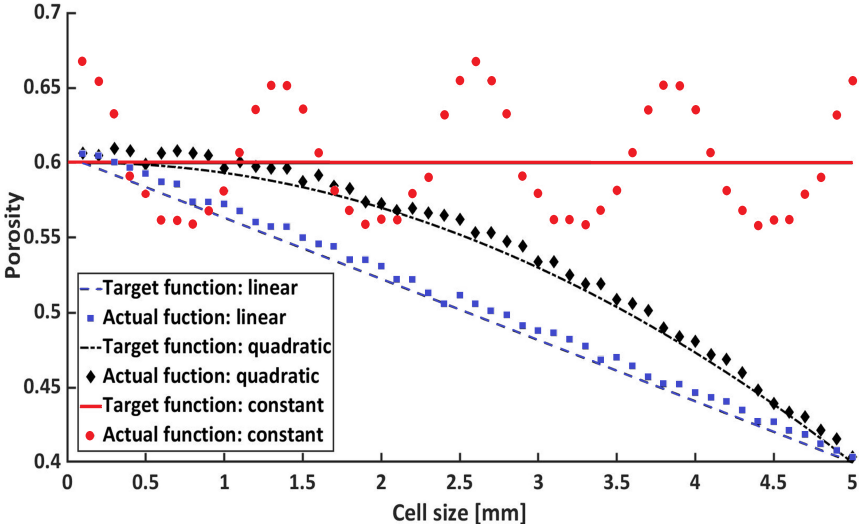

Figure 4.3: Porosity function of the constant, linear and quadratic function.

4.1.3 Model and setup for mechanical simulations

For the mechanical simulations, the static momentum balance in the small deformation regime is solved with a finite element discretization. This is done using the PACE3D framework, which employs a phase-field method for the geometry parametrization. Therefore, the structures generated in the MatLab program (see chapter 4.1.2) are discretized on a Cartesian grid and a diffuse interface is employed between the metal and the surrounding air.
From the micromechanics-microstructure simulations, the stress tensor $\boldsymbol{\sigma}$ and the strain tensor $\boldsymbol{\epsilon}$ are obtained as full field information. This gives rise to the normalized von Mises stresses σ_{VM}, whose maximum value determines the start of local plastification, if it reaches

the yield strength of the materials. Through homogenization, an effective Young modulus can additionally be obtained from the stress and strain field [47]. This is done using the volume-averaged stress and strain over the whole computational domain and relating them via the effective Young modulus.

Simulations of compression tests are performed with the specified stress σ_{BC}, which is applied in the z-direction, as the boundary condition on both sides of the simulation domain. All other boundaries are set to be stress-free. The domain is discretized using a Cartesian grid with $200 \times 200 \times 200$ elements. The air phase between the structure is modelled with a stiffness of zero, while the solid phase is considered to exhibit an isotropic elastic material behavior.

4.1.4 Results and discussion

Using the previously described algorithm, various gyroid structures with and without porosity gradients are generated. The following section provides a detailed examination and simulation analysis of these structures.

4.1.4.1 Structure consideration

Table 4.2 lists all 13 gyroid unit cells created for the subsequent investigation by mechanical simulations. Overall, the structures differ only in their porosity and gradient function. As can be seen from Table 4.2, the structures range in porosity from 0.4 to 0.8. For the structures with graded porosity (linear and quadratic), the

thickening of the structures always ends at a porosity of 0.4. It should be mentioned that, when the volume decreases, the influence on the mechanical stability should be considered, to optimize the lightweight potential. Since the porosity has a significant influence on the surface-to-volume ratio, and thus on the mechanical stability, it is also taken into account. The other input parameters that do not change are listed in Table 4.3. Assuming that the gyroid structures are characterized by the periodicity of their unit cell in all directions, it should be possible to apply the results of the mechanical simulation to multicell structures. In all three directions (x, y, z), the size of the analyzed cell is set to 2.5 mm. A unit cell is divided into 200 voxels per spatial direction ($n_{steps} = 200$). The possible deviation from the target function is 2 % ($delta = 0.02$).

Table 4.2: Created gyroid structures: constant gradient - linear gradient - quadratic gradient.

Constant gradient	**Linear gradient**	**Quadratic gradient**
0.4	-	-
0.5	0.4 to 0.5	0.4 to 0.5
0.6	0.4 to 0.6	0.4 to 0.6
0.7	0.4 to 0.7	0.4 to 0.7
0.8	0.4 to 0.8	0.4 to 0.8

Table 4.3: Non-varying input parameters across all structures.

Input parameter	Value
num_x	1
num_y	1
num_z	1
$unitCellSize[mm]$	2.5
n_{steps}	200
$delta$	0.02

4.1.4.2 Surface area-to-volume ratio

The surface area-to-volume (SA/V) ratio is an important technical aspect. A high SA/V ratio, for example, favors more efficient heat exchange [48], but usually has negative effects on the mechanical properties, which is why the SA/V ratio of the gyroid cells is investigated. To calculate the surface area-to-volume ratio, the stl files created in the MatLab program were imported into the Ansys workbench [49], where the volume and surface area of each structure were output.
The bar chart 4.4 lists the SA/V ratio from the gyroid structures in ascending order, with and without gradients. There, it can be seen that a high porosity favors the ratio. For this reason, the gyroid cell with a constant porosity of 0.8 has the highest SA/V ratio

of all structures. In contrast, the gyroid with a porosity of 0.4 has the lowest ratio. The structures with a quadratic gradient have a higher SA/V ratio than those with a linear gradient. This is due to the fact that the structure with a quadratic gradient thickens more slowly, as can be seen in Figure 4.3. Between the gyroid structures with a constant porosity of 0.5 and 0.6, there are four structures with gradients. In the further course of this work, a possible correlation between the SA/V ratio and the mechanical properties will be considered.

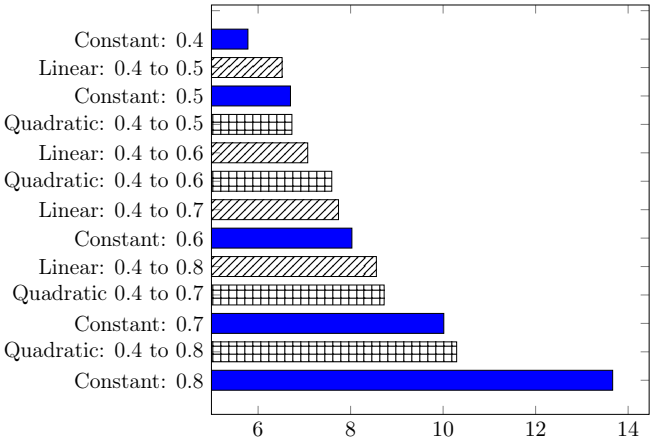

Figure 4.4: Surface [mm^2] / volume [mm^3] of gyroid structures in ascending order

4.1.4.3 Mechanical simulation

Material-independent and relative statements depending on the porosity type can be made about the structures with the same load

scenario. For this reason, scaled data are used. For the analysis of the structures, a steady-state case with an applied load of $\sigma_{\mathrm{BC}} = 400\,\mathrm{MPa}$ is considered. Since the simulations are performed within the linear-elastic regime, the results are independent of the structure material and the characteristic length, due to the linear scalability. The effective Young modulo as well as the maximum and mean values of the von Mises stress are evaluated. The latter values respectively correspond to the volume average of the von Mises equivalent stress field $\bar{\sigma}_{\mathrm{VM}}$ and its maximum value $\sigma_{\mathrm{VM,max}}$ within the domain. Note that both quantities are given normalized with the load σ_{BC} and can thus be interpreted as mean and maximum values of a stress amplification factor. Dividing the yield strength of the material under consideration (e.g. AlMg7Si0.6) by this amplification factor gives the actual limit for local plastification and thus an effective yield strength. The effective Young modulus is given normalized with the one of the structure material. In order to obtain physical quantities, a multiplication can be carried out with the material value under consideration. For example, $\bar{E}_{AlMg7Si0.6} = E_{AlMg7Si0.6}\bar{E}$, with $E_{AlMg7Si0.6} = 59\,\mathrm{GPa}$, if the structure is made of the alloy AlMg7Si0.6. The use of these normalized quantities allows a comparison between the structures, without specifying the material or length scale.

Tables 4.4-4.6 represent the material-independent and scaled values of the respective structures. For a better clarity and comprehensibility of the results, they are also shown in the bar charts 4.5-4.7. The structures in the charts are all labelled according to the following pattern: '*Type of gradient function: Porosity interval*'. 'Quadratic: 0.4 to 0.8', for example, means that a gyroid structure

with a quadratic gradient function and a porosity interval between 0.4 and 0.8 is considered.

Table 4.4: Scaled results of the gyroid structure with a constant gradient [dimensionless] of the normalized effective Young modules $\bar{E}$, a mean von Mises stress $\bar{\sigma}_{\mathrm{VM}}$ and a maximum von Mises stress $\sigma_{\mathrm{VM,max}}$, which is given for different porosities.

Porosity	$\bar{E}$	$\bar{\sigma}_{\mathrm{VM}}$	$\sigma_{\mathrm{VM,max}}$
0.4	0.10	0.88	10.40
0.5	0.05	0.99	14.92
0.6	0.03	1.09	19.50
0.7	0.02	1.18	23.94
0.8	0.01	1.24	28.74

Table 4.5: Scaled results of the gyroid structure with a linear gradient [dimensionless] of the normalized effective Young modules $\bar{E}$, a mean von Mises stress $\bar{\sigma}_{\mathrm{VM}}$ and a maximum von Mises stress $\sigma_{\mathrm{VM,max}}$, which is given for different porosities.

Porosity	$\bar{E}$	$\bar{\sigma}_{\mathrm{VM}}$	$\sigma_{\mathrm{VM,max}}$
from 0.4 to ...0.5	0.06	0.97	14.99
...0.6	0.04	1.02	18.94
...0.7	0.03	1.07	22.82
...0.8	0.02	1.11	28.01

Table 4.6: Scaled results of the gyroid structure with a quadratic gradient [dimensionless] of the normalized effective Young modules $\bar{E}$, a mean von Mises stress $\bar{\sigma}_{\mathrm{VM}}$ and a maximum von Mises stress $\sigma_{\mathrm{VM,max}}$, which is given for different porosities.

Porosity	$\bar{E}$	$\bar{\sigma}_{\mathrm{VM}}$	$\sigma_{\mathrm{VM,max}}$
from 0.4 to ...0.5	0.06	0.99	15.07
...0.6	0.04	1.05	18.75
...0.7	0.02	1.11	23.86
...0.8	0.02	1.16	29.64

In Figure 4.5, the blue bars represent the maximum normalized stresses ($\sigma_{\mathrm{VM,max}}$) of the gyroid structures, sorted in ascending order. In addition, the corresponding SA/V ratio is shown in striped bars.

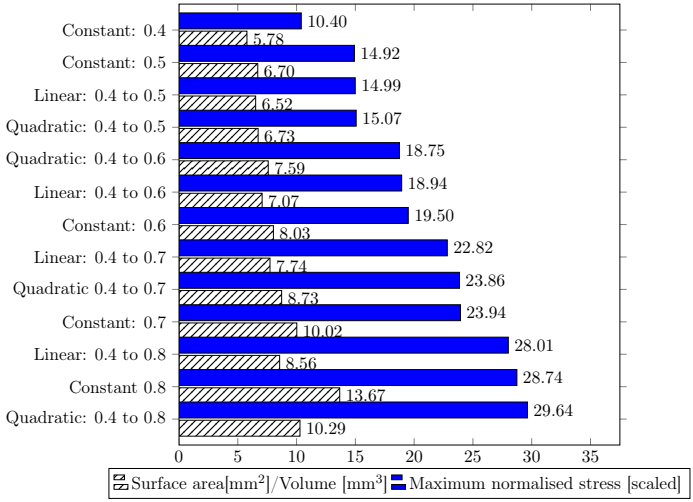

Figure 4.5: Dimensionless, scaled maximum normalised stress $\sigma_{\mathrm{VM,max}}$ [scaled] of gyroid structures in ascending order, in comparison to the SA/V ratio of the same structure.

The gyroid structures with a quadratic porosity have the highest (*quadratic: 0.4 to 0.8*) and the gyroid structure with constant porosity has the lowest (*constant: 0.4*) maximum stresses, respectively. In addition, the bar graph illustrates that the linear gradient structures have lower scaled normalized maximum stresses than the quadratic gradient structures, but higher than the constant gradient structures. A structure with a linear porosity of 0.4 to 0.6 corresponds to an average of a constant porosity of 0.5. Here it becomes clear that by adjusting the gradient, a higher SA/V ratio is achieved, but also higher maximum stresses. This observation also applies to the structure with a linear porosity from 0.4 to 0.8, which corresponds to an average porosity of 0.6.

As in Figure 4.5, the dimensionless, scaled and normalised stresses

[$\bar{\sigma}_{\mathrm{VM}}$] of the structures are also sorted in ascending order in Figure 4.6. This allows a faster comparison of the diagrams. The structural arrangements of the two diagrams are not in the same order, since there is a deviation between the highest and the lowest values of the maximum normalized stress and the mean normalized stress.

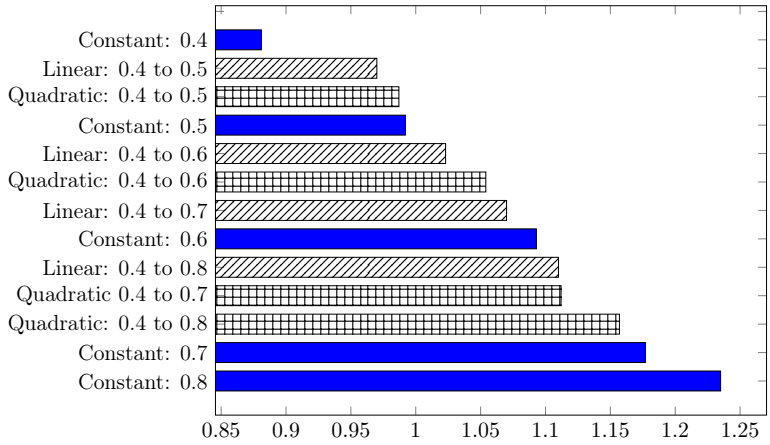

Figure 4.6: Dimensionless, scaled mean normalised stress $\bar{\sigma}_{\mathrm{VM}}$ of gyroid structures in ascending order.

Compared to the structures with quadratic or linear porosity, the structures with constant porosity have higher normalized stresses. The higher the porosity level of the structures, the higher the normalized stresses. This may indicate a more uniform stress distribution in the structures with gradients, or that the structure has more unstressed regions. The gyroid structure '*quadratic: 0.4 to 0.8*', for example, has a higher SA/V ratio than '*constant: 0.7*', but a lower mean normalized stress.

The structures with a linear gradient generally exhibit the lowest

mean stresses, compared to the other structures, which is also reflected in the scaled, dimensionless elastic modulus (see Figure 4.7).

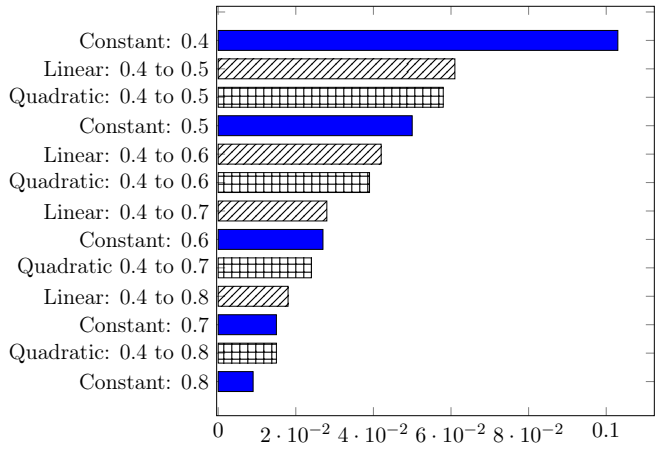

Figure 4.7: Dimensionless, scaled effective Young modules $\bar{E}$ of gyroid structures in decreasing order.

The structures with a linear gradient have a higher effective Young modulus $[\bar{E}]$ than the other structures in the same porosity range. This can be partly explained by the fact that the linear gradient structures are thickened more quickly and more evenly, which means that the initiating force can be better distributed. The Figure 4.7 lists the scaled and dimensionless effective Young modulus of the considered structures in decreasing order. It becomes clear that the porosity has a high influence on the effective Young modulus. Between the structures '*constant: 0.4*' and '*constant: 0.8*', for example, the effective Young modulus is reduced by a factor of about 11. In contrast, the effective Young modulus for the structures '*quadratic: 0.4 to 0.5*' ('*linear: 0.4 to 0.5*') and '*quadratic: 0.4 to 0.8*' ('*linear:*

0.4 to 0.8') decreases by a factor of 3.9 (quadratic) or 3.4 (linear). A clear relationship between the SV/A ratio and the effective Young modulus can be seen when comparing Figures 4.4 and 4.7. The sorted effective Young modulus is almost in the same order as the sorted SV/A ratio.

The evaluation of the von Mises stress field on the gyroid structures revealed that it is generally located at the rounded edges of the structure. It was noticed that the stress peaks for the gyroid structures with gradients are on the side with the highest porosity, due to the difference in porosity, while the stress peaks for the structures with constant porosity are on both sides, which can be seen in Figure 4.8. The stressed areas are marked in red and are located at the rounded edges, as described previously. Accordingly, the loaded edges are likely to fail first in compression tests. In addition, the one-sided loading of the structures with gradients would explain the higher stress distributions given in Figure 4.5.

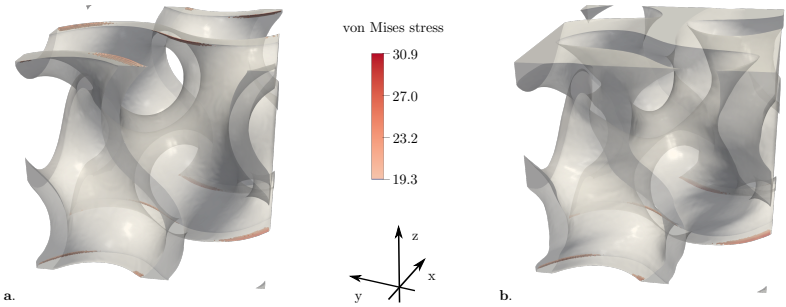

Figure 4.8: Maximum stresses on the surface of the gyroid structure with (**a**) a constant porosity of 0.8; (**b**) a quadratic porosity function between 0.4 and 0.8.

The mechanical simulation has shown that the structures with gradients enable new design and lightweight construction possibilities. The structures with gradients can be better adapted to the required properties. Depending on the choice of the new and the original structure, one property can be specifically improved, while another property can be reduced. In general, it can be said that the SA/V ratio increases with increasing porosity, while the effective Young modulus decreases. By choosing the structure '*linear: 0.4 to 0.5*', for example, instead of '*constant: 0.5*', the effective Young modulus increases by about 22 % [quadratic gradient 16 %], while the surface to SA/V ratio and the mean normalized stress would decrease by about 2 % [quadratic about 0 %].
If only the mechanical stability is of interest and not the lightweight potential or the surface area-to-volume ratio, the gyroid with the lowest porosity - in our case 0.4 - is still unbeatable.
Likewise, the gyroid with a constant porosity of 0.8 would be interesting for applications where only the surface to volume-ratio is of central importance, but not the mechanical properties.

4.1.5 Conclusions

In this study, gyroid structures, which are associated with the TPMS family, were investigated. In addition to the used structures with constant porosity, graded structures were produced. For the graded structures, a distinction was made between structures with linear and quadratic gradients. For the mechanical simulation, the created structures were imported into PACE3D. The results were converted into dimensionless, material-independent indices, so that a general

statement can be made. In addition to the mechanical simulation, the SV/A ratio was also analyzed.
The mechanical simulation shows that the introduction of the gradient multiplies the range of engineering design possibilities. Depending on the desired property and application, it is worthwhile to integrate a gradient into the structure. In general, it can be said that the structures with gradients usually have higher stress peaks, but lower mean normalized stresses.
In Chapter 7.1.1, different gradient patterns of 10x10x10-cell gyroid structures are experimentally investigated.

The investigation into the behavior of TPMS structures within the framework of load-specific phase-field based shape optimization is addressed in Chapter 5, with a focus on optimization under various loading scenarios.

5 Phase-Field Based Shape Optimization

This chapter addresses the shape optimization of TPMS-structures using the phase-field method. Various stress boundary conditions applied to the structures are investigated.
In the first section, a stress boundary condition is considered where the structures to be optimized lose their periodicity in the respective loading direction. In the subsequent section, the initial and optimized structures are experimentally validated.
In the last of the three sections, a stress boundary condition is employed that maintains periodicity in all spatial directions during the optimization process. These results are also experimentally validated in Chapter 7.

5.1 Shape optimization of porous structures by phase-field modelling with strain energy density reduction

This chapter is based on the publication: [3]

5.1.1 Setup for mechanical simulations

In order to optimize the shape, a unit cell sheet-based diamond-, gyroid-, and primitive structure with a porosity of approximately 85 % is utilized. The initial structure is then subjected to unilateral compressive loading, resulting in an energetically optimized shape, as illustrated in Figure 5.1.

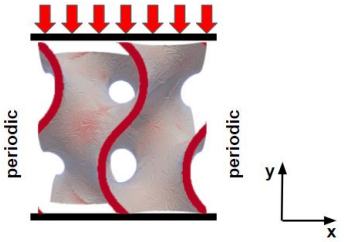

Figure 5.1: Boundary conditions of the initial structure.

The load on the structure is applied in the y-direction, with a constant stress of 400 MPa, while periodic boundary conditions are assumed in both x- and z-directions.
A pseudo-time records the process in which the structure geometry changes successively toward the optimal shape.
According to equation (2.5), a stationary structure-mechanical solution is calculated for each time step. Subsequently, $200 \times 200 \times 200$ grid cells are initialized for three-dimensional microstructure simulations, while the two-dimensional examples are discretized with 200×200 cells. Isotropically elastic behavior is assumed for the structural material, while the pore phase is modeled with a residual stiffness of one thousandth of the solid material.

The TPMS structure is considered to consist of an isotropic material with a mass density of $2680\,\mathrm{kg\,mm^{-3}}$, a Young's modulus of 59 GPa, and the Poisson ratio 0.35. In addition, a homogenization is performed, in which the effective stiffness of the structure is determined from the stress and strain field [47, 50]. If the effective stress is constant, as is the case in this work, structures that minimize the elastic free energy yield a maximum effective stiffness. A homogenization approach allows the transfer of results from the micro to the macro level *cf.*, *e.g.*, [35].
The following mechanical analysis values, such as the effective Young's modulus, are accordingly given in dimensionless values.

5.1.2 Results and discussion

The computational optimization is based on the phase-field method, which reduces the total energy density in the system by shifting the interface to the energetically more favorable region. For further details, please refer to Subchapter 2.2. Consequently, the initially considered structures evolve over time into structures with a new topology. The optimized structure no longer resembles the initial structures.
Since we are interested in TPMS-like structures, the simulation is terminated as soon as the topology of the initial structure is changed. Figure 5.2 shows the shape-optimized structures of the last simulation step, frame 10. Thus, one frame step corresponds to fifty time steps.

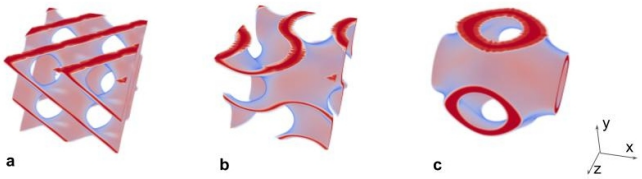

Figure 5.2: Shape-optimized structures - a. Diamond; b. Gyroid; c. Primitive.

When looking at the shape-optimized structures, it becomes evident that a volume redistribution has taken place during the shape optimization. As can be seen from the diagrams 5.3 - 5.5, volume was added to highly energetic (and correspondingly loaded) areas, while volume was subtracted from less stressed areas, resulting in energy minimization in the overall system.

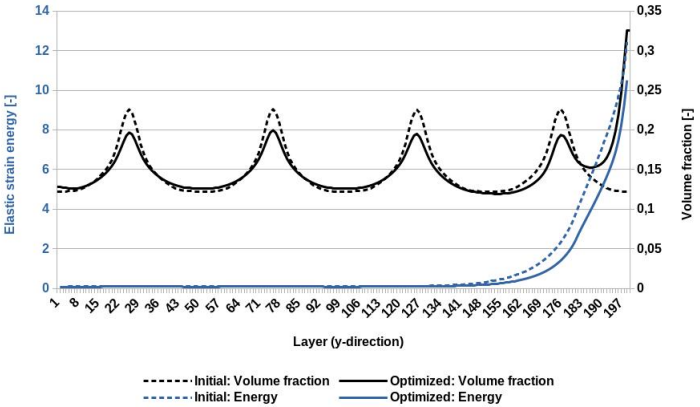

Figure 5.3: Energy (primary axis) and volume (secondary axis) distribution of the diamond structure in the y-direction of the initial structure (dashed line) and the optimized structure (solid line), as well as the volume difference of the two structures.

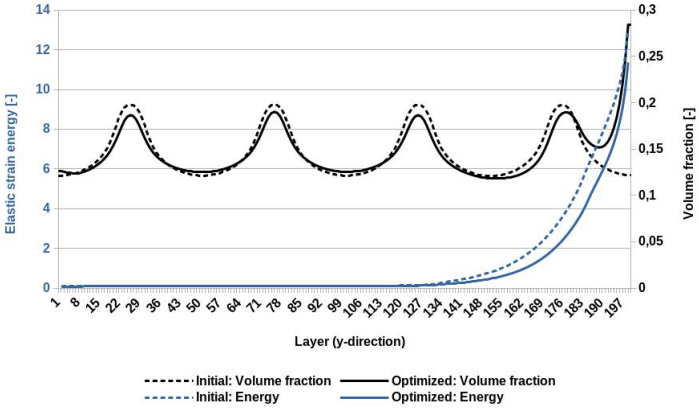

Figure 5.4: Energy (primary axis) and volume (secondary axis) distribution of the gyroid structure in the y-direction of the initial structure (dashed line) and the optimized structure (solid line), as well as the volume difference of the two structures.

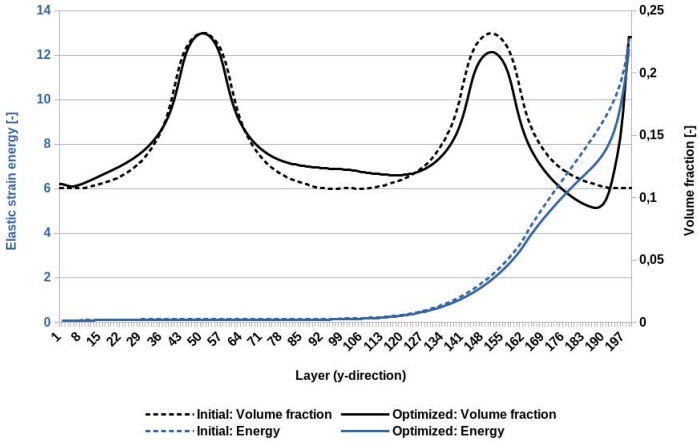

Figure 5.5: Energy (primary axis) and volume (secondary axis) distribution of the primitive structure in the y-direction of the initial structure (dashed line) and the optimized structure (solid line), as well as the volume difference of the two structures.

The energy is plotted on the primary x-axis, while the volume fraction is plotted on the secondary x-axis, across the layers. The initial structure is shown with a dotted line, while the optimized structure is shown with a solid line. From the volume distribution of the initial structure, the characteristic periodic shape, which progresses in the y-direction, can be seen for all three structures. After shape optimization, the volume fraction of the uppermost layers is increased for all three structures in the y-direction, while it is removed from less energetic regions. The temporal energy reduction, which takes place for all three structures, is shown comparatively in the bar chart 5.6.

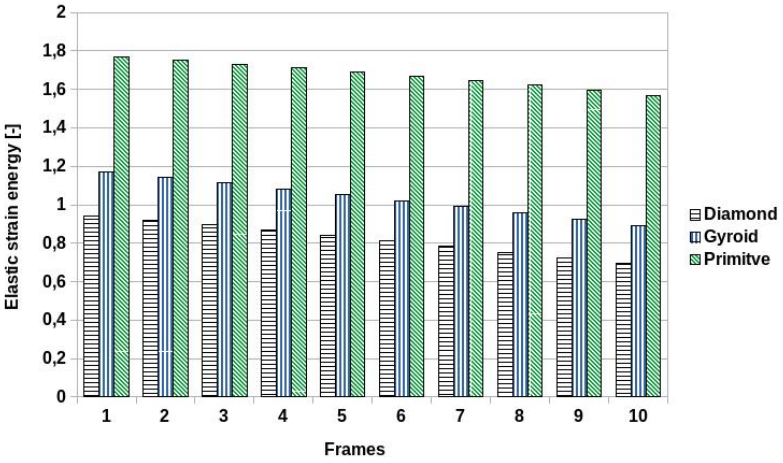

Figure 5.6: Course of the decrease of the internal energy of the shape-optimized TPMS.

The diagram shows that after each simulation step, the energy in the system is reduced. The primitive structure has the highest initial energy, followed by the gyroid structure. The diamond structure

has the lowest energy. In the case of the diamond structure, shape optimization reduces the energy in the overall system by about 38 %, while for the gyroid structure, the energy is reduced by about 34 % and for the primitive structure by about 13 %. As a result, the diamond structure has the highest energetic reduction in the overall system.

Table 5.1 compares the development of the volume fraction, the surface-to-volume ratio, and the effective Young's modulus during the shape optimization process of all three structures. Frame 0 represents the initial structure. Since the surface-to-volume ratio is important in engineering applications, such as heat exchangers [51], this property was selected.

Table 5.1: Development of the structural and mechanical properties of the initial structures (frame 0), up to the shape-optimized structure (frame 10).

	Diamond			**Gyroid**			**Primitive**		
Frame	Volume fraction	Surface/ volume ratio	Young's modulus (dim.less)	Volume fraction	Surface/ volume ratio	Young's modulus (dim.less)	Volume fraction	Surface/ volume ratio	Young's modulus (dim.less)
0	**0.148**	**0.258**	**2.186**	**0.146**	**0.211**	**1.748**	**0.143**	**0.164**	**0.989**
1	0.148	0.258	2.244	0.146	0.210	1.800	0.143	0.164	1.005
2	0.148	0.258	2.321	0.146	0.210	1.853	0.143	0.164	1.022
3	0.148	0.258	2.403	0.146	0.211	1.909	0.143	0.165	1.029
4	0.148	0.258	2.493	0.146	0.211	1.970	0.143	0.166	1.057
5	0.148	0.258	2.594	0.146	0.211	2.034	0.143	0.166	1.077
6	0.148	0.258	2.706	0.146	0.211	2.104	0.143	0.166	1.097
7	0.148	0.258	2.954	0.146	0.212	2.180	0.143	0.166	1.118
8	0.148	0.258	3.091	0.146	0.212	2.262	0.143	0.166	1.141
9	0.148	0.258	3.240	0.146	0.213	2.350	0.143	0.166	1.165
10	0.148	0.258	3.403	0.146	0.213	2.444	0.143	0.167	1.190

The volume fraction, which is about 85 % in porosity for all structures, is kept constant during shape optimization. Between the

structures, a porosity variation of about 4 % can be observed.
Comparing the energy with the effective modulus of elasticity in Table 5.1, the structure with the highest energy has the lowest effective Young's modulus and vice versa. Accordingly, the diamond cell has the highest effective Young's modulus and the primitive cell the lowest. In general, the effective Young's modulus could be increased from 20 % (primitive) to 55 % (diamond). The ranking of the Young's modulus of the initial structures can be confirmed by various studies [52] [53]. In the publication by Naghavi *et al.* [53], for example, the mechanical properties of gyroid and diamond structures of Ti6Al4V were compared for later use as bone implants. It was discussed that the diamond structure also has a higher Young's modulus than the gyroid structure. This order is maintained during shape optimization.
In general, the diamond cell has the highest surface-to-volume ratio, followed by the gyroid structure and the primitive structure. For both the diamond structure and the primitive structure, no reduction in the surface-to-volume ratio was observed during the shape optimization process. For the primitive structure, a slight increase from 0.164 to 0.167 was observed. At the beginning of the shape optimization process, the gyroid structure results in a slight decrease in the surface-to-volume ratio. From frame 9, however, a slight increase from 0.211 to 0.213 can be observed.
As a consequence, the TPMS structures lose their property of periodicity in all spatial directions. Due to the previously mentioned "periodic" boundary condition in the x- and z-directions, the periodicity in these directions could be preserved. This means that a later multiplication in the respective spatial directions and a later adaptation to the geometry would be possible for later applications.

5.1.3 Conclusion

In this work, a shape optimization based on the phase-field method is performed on TPMS structures. It is shown that while maintaining the topology of the respective TPMS structures, their structure could be shape-optimized by minimizing the energy in the system, using the phase-field method. Overall, an increase of the effective Young's modulus could be achieved by the interfacial displacement, with the same volume and a simultaneous partial increase in the surface-to-volume ratio. For all three structures, the effective Young's modulus was increased by at least 20 %. The largest improvement is found for the diamond structure, which showed an increase of 55 %.
The characteristic property of the TPMS unit cell, which is periodic in all spatial directions, is no longer preserved after the shape optimization. This periodicity could only be maintained in the $x-$ and $z-$directions. However, by preserving the shape, other characteristics such as the high surface-to-volume ratio, which is of interest for certain engineering applications, could be retained.
In general, these results open up new design possibilities, especially in areas where stability and low weight are required. The structures for sandwich cores, whose periodicity could be maintained in the x- and z-direction, and the fact that an arbitrary duplication of the optimized structures in the respective spatial directions is possible, are very interesting for further research.
The corresponding experimental validation of the shape-optimized structures presented here can be found in Chapter 7.2.1.

Building on previous discussions, Chapter 5.2 will also explore the

shape optimization of TPMS structures. This time, the focus will be on conducting both uni- and multi-loading-specific shape optimization, while maintaining the periodicity of the structures in the loading directions.

5.2 Phase-field based shape optimization of uni- and multiaxially loaded nature-inspired porous structures while maintaining characteristic properties

This chapter is based on the publication: [5]

Within this work, single-cell gyroid structures with a porosity of 85 %, 80 % and 75 % in a three-dimensional domain Ω are considered, each with 200 cells in each spatial direction. Figure 5.7 illustrates the sheet-based gyroid structure with three different porosities (ρ) of 75 %, 80 %, and 85 %, which will be the focus of this investigation.

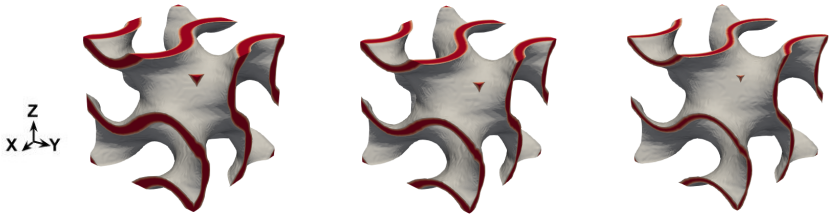

(a) $\rho = 75\,\%$ **(b)** $\rho = 80\,\%$ **(c)** $\rho = 85\,\%$

Figure 5.7: Sheet-based gyroid structures with porosities ρ of a) 75 %, b) 80 %, and c) 85 %.

With the modified phase-field method described in subsection 2.2.2, gyroid unit cells are shape optimized while maintaining periodicity. Initially, these cells are subjected to unidirectional loading, followed by optimization under multidirectional loading conditions.
The goal is to enhance the stiffness for the given load case. The process continues until the volume distribution results in a significant topological change. The simplified sequence of this process is illustrated in Figure 5.8.

5.2.1 Results and discussion

In the following, gyroid unit cells with a volume fraction of $0.25\,[-]$, $0.2\,[-]$, and $0.15\,[-]$ are shape optimized under loading with a predefined effective strain. This chapter is divided into two parts. The first part addresses shape optimization of the structures under unidirectional, the second part focuses on multidirectional load scenarios and provides a discussion on the corresponding simulation results.
Moreover, Chapter 7.2.2 examines the experimental validation of the original and optimized structures subjected to unidirectional loading. The findings from simulations and experiments are then compared.

5.2.1.1 Unidirectional loading

The structures resulting from the shape optimization for the respective volume fraction of $0.25\,[-]$, $0.2\,[-]$, and $0.15\,[-]$ under a uniaxial load in x-direction can be found in Figure 5.9.

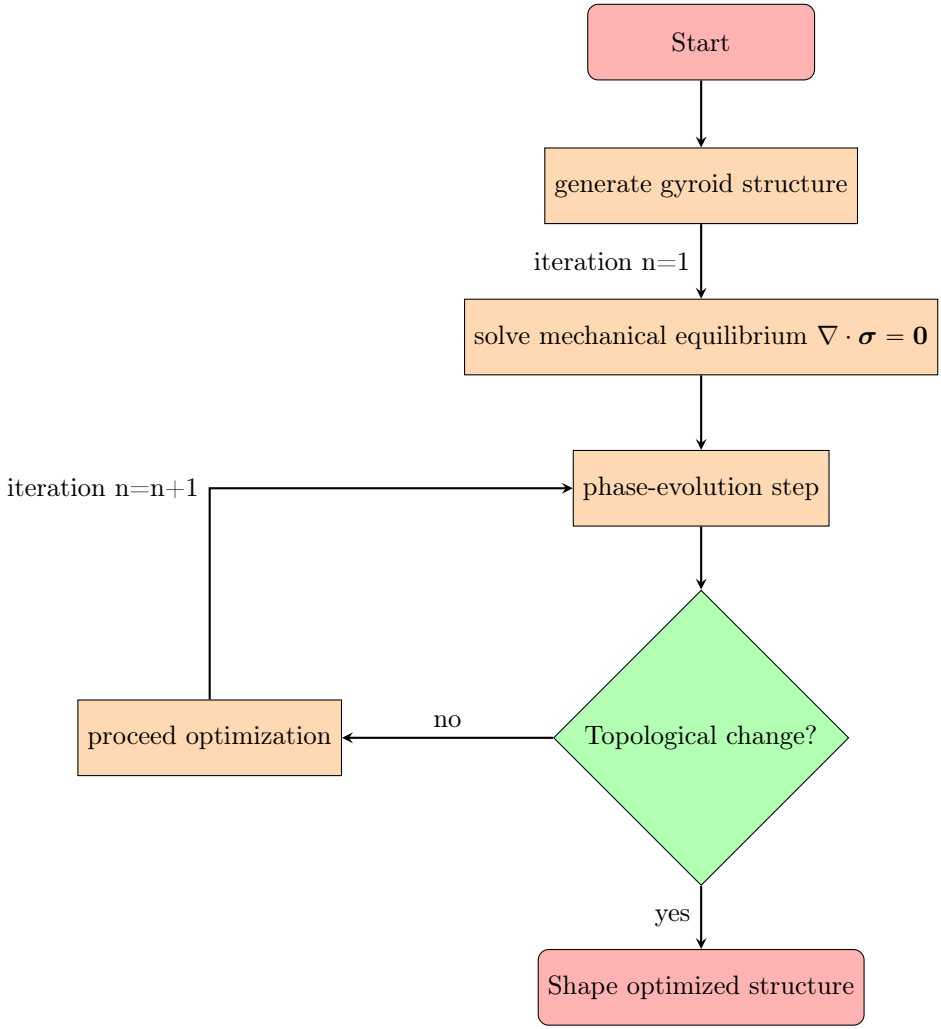

Figure 5.8: Flow chart of the shape optimization process.

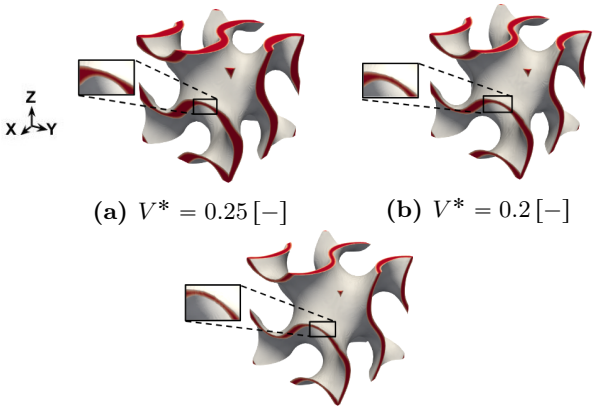

(a) $V^* = 0.25\,[-]$ **(b)** $V^* = 0.2\,[-]$

(c) $V^* = 0.15\,[-]$

Figure 5.9: Shape-optimized sheet-based gyroid structures with volume fractions V^* of a) $0.25\,[-]$, b) $0.2\,[-]$, and c) $0.15\,[-]$.

According to the objective of shape optimization, the original form of the unit cell is preserved. Moreover, the periodicity of the unit cell is maintained, which allows for a later multiplication of the unit cells in the respective spatial directions. During the optimization process, among other things, the cross-braces in the x-direction have thinned, which is highlighted in the marked area.

To analyze the volume distribution through the optimization process in more detail, in the x-direction, the altered layer-wise volume fraction from the initial structure (solid green line) compared to the optimized structure (dotted grey line) is shown in Figures 5.10 - 5.12. Additionally, the solid red line shows the difference in volume fraction between the original structure and the optimized structure. In this context, the black zero line separates the areas where a positive difference is above, and a negative difference is below the line. A positive difference indicates an increase in material addition, while

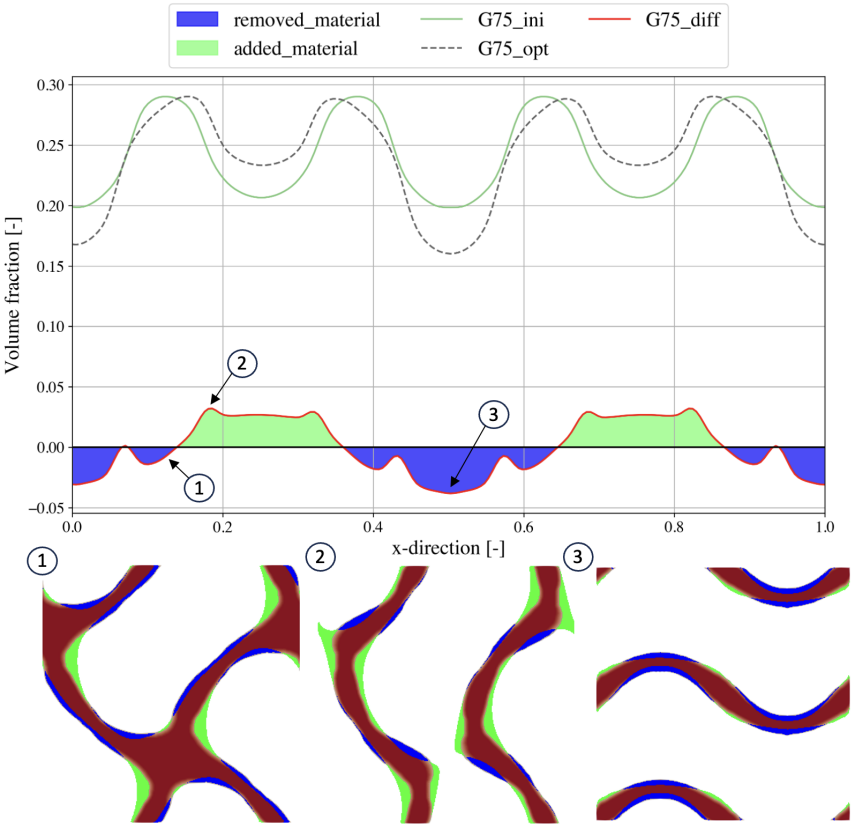

Figure 5.10: Comparison of the plane-wise volume fraction (on the yz-axis) along the x-direction between the initial (G75_ini, solid line) and the optimized (G75_opt, dashed line) gyroid structure, illustrating the areas where material is added (light-green) and removed (blue) during the optimization process.

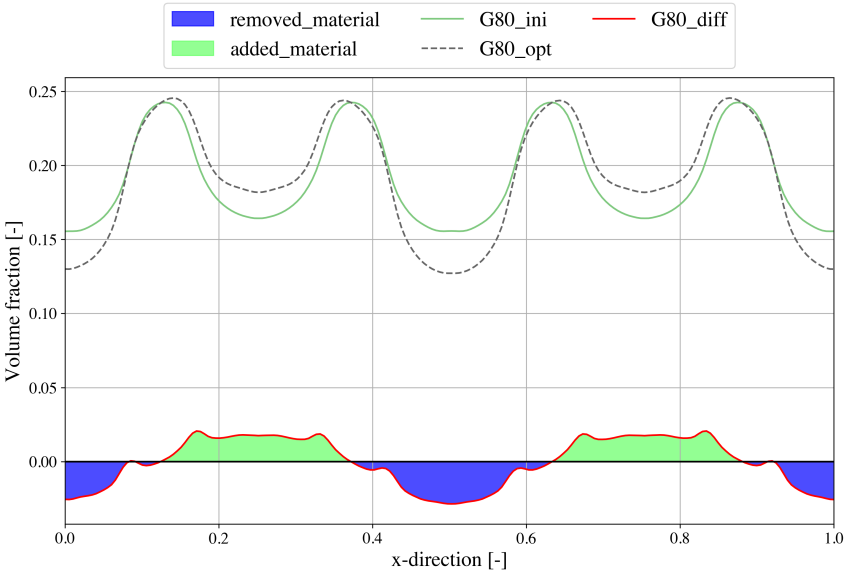

Figure 5.11: Comparison of the plane-wise volume fraction (on the y-axis) along the x-direction between the initial (G80_ini, solid line) and the optimized (G80_opt, dashed line) gyroid structure, along with a representation of areas where material is added (green) or removed (blue) during the optimization process, depicted by the difference (red line).

a negative difference indicates a predominant removal of material. The blue-marked areas below the difference line indicate the planes where more material is removed compared to the original structure due to the displacement of the interfaces. The green-marked area above the difference line shows the planes where material is added. The x-direction represents the normalized coordinate x/L.
When examining the difference curves of the structures, it becomes clear that the material redistribution has taken place in the same

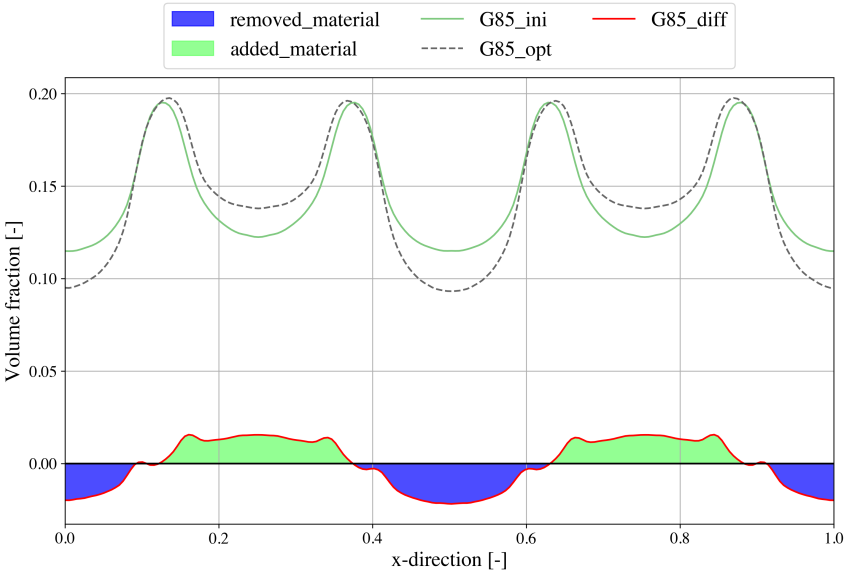

Figure 5.12: Comparison of the plane-wise volume fraction (on the y-axis) along the x-direction between the initial (G85_ini, solid line) and the optimized (G85_opt, dashed line) gyroid structure, along with a representation of areas where material is added (green) or removed (blue) during the optimization process, depicted by the difference (red line).

areas for all three structures, and the difference curve has a periodic course. Comparing the three diagrams of the gyroidal unit cells with a volume fraction of $0.25\,[-]$, $0.2\,[-]$, and $0.15\,[-]$ shows that the volume redistribution occurred in the same places. Due to the larger initial volume, a higher volume change is observed in the gyroid structure, with a volume fraction of $0.25\,[-]$.
Therefore, this structure is chosen to illustrate the volume redistribution based on three different planes, which are shown in Figure 5.10

in connection with the difference. Since continuous shape optimization would lead to the complete removal of the webs, the simulation process is terminated at this point. Cross-sectional image 1 of Figure 5.10 corresponds to an area between the maximum and minimum difference. Here, it is evident that material is added at the branches and material is removed from the cross-braces.
The displayed layers of the extreme points from the Figure 5.10 correspond to where a lot of material has been added or removed. The respective planes of the structure, where the global maximum and minimum of the changed volume fraction from the gyroid structure with a porosity of 75 % in comparison with the initial structure, is shown in cross-sectional images 2 and 3 in Figure 5.10. In image 3, it is evident that the cross-braces in the non-loading direction are reduced. This observation can also be made in the marked areas of Figure 5.9. The previously presented load-specific changes lead to structural and mechanical property changes, which are listed in Table 5.2.

Generally, from the column for the volume fracion (V^*), it is observable that the target volume fraction of $0.25\,[-]$, $0.2\,[-]$, and $0.15\,[-]$ is not precisely achieved. The gyroid cell with a volume fraction of $0.2\,[-]$ deviates from its target volume fraction by about 2 % the least, while the other two structures deviate by approximately 4 % from the set target volume fraction. Increasing the cell area, enhances the accuracy of the structuring, but requires significantly larger computation times for the simulation. Additionally, it is noticeable that structures with a higher volume fraction have a smaller surface area. Through the shape optimization process, the surface area decreases by about 1 % for the unit cell with a volume

Table 5.2: Structural and mechanical properties of the initial and shape-optimized gyroid-structure.

Structure:	85 %			80 %			75 %		
	V^*	**Surface**	$\bar{E}/E_s$ **(dim.less)**	V^*	**Surface**	$\bar{E}/E_s$ **(dim.less)**	V^*	**Surface**	$\bar{E}/E_s$ **(dim.less)**
Initial	0.243	5.976	0.050	0.192	6.027	0.064	0.144	6.044	0.087
Optimized	0.243	5.981	0.067	0.192	5.993	0.089	0.144	5.974	0.128

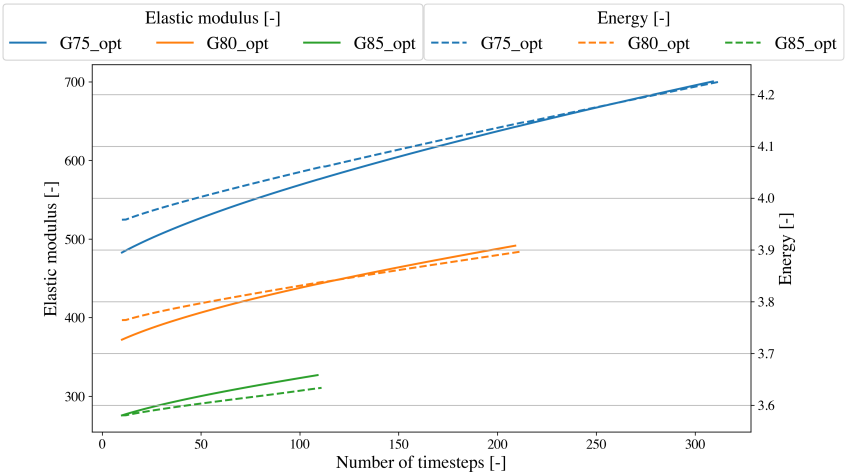

Figure 5.13: Relationship between the energy evolution (dashed line) and the modulus of elasticity (solid line) across the simulation of the three considered gyroidal unit cells with a volume fraction of 0.25 [−] (G75_opt), 0.2 [−] (G80_opt), and 0.15 [−] (G85_opt).

fraction of 0.2 [−] and 0.15 [−]. Only for the gyroid structure with a volume fraction of 0.15 [−] a slight increase in surface area is observed. Additionally, it is observable that an increase in the effective dimensionless Young's modulus is achieved through the interface displacement for all three structures. For the structure with a volume fraction of 0.25 [−], the highest increase in the Young's modulus of about 45 % is achieved. From the Figure 5.13, the relationship between the increase in energy (dashed line) and the resulting increase in the effective Young's modulus (solid line) throughout the entire simulation process (number of time steps) is shown.

The modulus of elasticity is given in dimensionless form by $\bar{E}/E_s$, and similarly the dimensionless energy $\bar{f}_{\mathrm{el}}/E_s$ is used. The transformation into dimensionless parameters enables material-independent statements, which is possible due to linearity. As already explained in Chapter 2.2.2, it is noticeable that the displacement of the interfaces results in an increase in energy, which simultaneously leads to an increase in stiffness. Accordingly, an increase in stiffness could be achieved for all three structures. Moreover, the diagram reveals that the energy and the Young's modulus have different slopes. This can be attributed to the weighting during the simulation process. It is also striking that, depending on the different porosities, the structures under consideration are characterized by different numbers of iterations during the optimization process. Since the simulation is terminated just before a topology change occurs due to interface displacement, the largest amount of optimization iterations to reach this point occurs for the gyroid structure with a volume fraction of $0.25\,[-]$ is the longest. As a result, the highest energy change and accordingly the highest increase in stiffness are achieved.
Following the demonstration that shape optimization of complex porous structures while maintaining periodicity is feasible for unidirectional loading cases, the focus now shifts to an examination of the case for multidirectional loading scenarios.

5.2.1.2 Multidirectional loading

In practical applications, multiple loading conditions in different spatial directions are often relevant [54]. In the following, gyroid unit

cells with a volume fraction of 0.15 % are subjected to multidirectional loading and optimized for each loading case. Diverse optimization possibilities are illustrated using the phase-field method. Similar to the unidirectional case, the volume fraction is kept constant, resulting in volume redistribution during the simulation. To consider more complex loading scenarios, shear loading is prescribed in addition to uni-axial strain. As in previous simulations, the simulation is terminated once the topology changes. Three different combinations of loading cases are considered, applying the macroscopic strain $\varepsilon = 0.01$ in different directions according to

$$\bar{\boldsymbol{\epsilon}}_{\text{case1}} = \begin{bmatrix} 0 & -\varepsilon & 0 \\ -\varepsilon & -\varepsilon & 0 \\ 0 & 0 & -\varepsilon \end{bmatrix}, \quad \bar{\boldsymbol{\epsilon}}_{\text{case2}} = \begin{bmatrix} 0 & -\varepsilon & 0 \\ -\varepsilon & -\varepsilon & -\varepsilon \\ 0 & -\varepsilon & 0 \end{bmatrix}, \quad \bar{\boldsymbol{\epsilon}}_{\text{case3}} = \begin{bmatrix} 0 & 0 & 0 \\ 0 & -\varepsilon & -\varepsilon \\ 0 & -\varepsilon & 0 \end{bmatrix}. \tag{5.1}$$

The respective shape-optimized structures corresponding to the load cases depicted in Formula 5.1 are shown in Figure 5.14.

Similarly to the one-dimensional loading case, the topology is not disrupted during the shape optimization process under multidirectional loading.
Figure 5.15 illustrates the volume redistribution for the three considered cases along the x-direction.

The initial volume fraction distribution of the structure is included in the diagram as reference data (solid black line). The diagram reveals that the volume is redistributed differently depending on the loading case, resulting in load-specific volume fraction profiles with

(a) Case 1 **(b)** Case 2 **(c)** Case 3

Figure 5.14: Load-specific shape-optimized, sheet-based gyroid structures under multidirectional loading with a volume fraction of 0.15 [−], based on the load cases Case 1 to Case 3 as presented in equation 5.1.

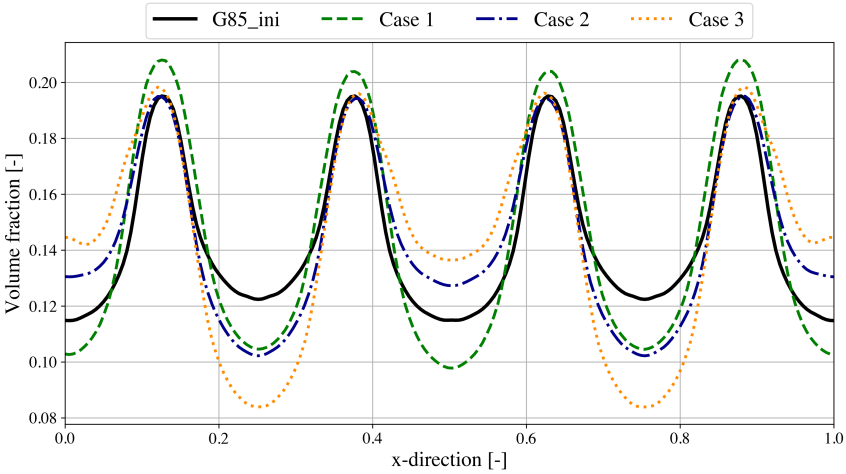

Figure 5.15: Volume fraction distribution in the x-direction of the initial structure and the shape-optimized structures under multi-axial loading for three different cases: Case 1, Case 2 and Case 3.

locally varying volume increases or decreases along the considered x-direction.
While the redistribution of volume led to an increase in the stiffness of the respective structures in the corresponding loading directions, the periodicity of the unit cell could simultaneously be maintained. Consequently, an increase in the effective modulus of elasticity is achieved in all three structures, as indicated in Table 5.3.

When comparing the effective modulus of the initial structures, it becomes evident that it lies within similar ranges for the three considered loading cases. The largest increases in the modulus of elasticity are achieved through optimization in loading cases 1 and 3. This is attributed to the need to terminate the simulation for case 2 prematurely to prevent a change in the structure's topology. While a percentage increase of the dimensionless effective modulus of elasticity of up to approximately 60 % (case 3) is achieved, there is a slight reduction in surface area of up to 2.1 %.
These three examples illustrate that the phase-field method is a suitable approach for stress-specific optimization of complex porous structures under multidirectional loading, while maintaining the volume and periodicity during the optimization process.

5.2.2 Conclusion

Under the constraints of constant volume fraction and preserving periodicity of the structure, a modified phase-field method for the shape optimization process is applied to computationally determine

shape optimized complex porous structures. During the shape optimization process, volume redistribution occurs by shifting the interface. In contrast to the conventional phase-field method, where the goal is to minimize energy, the objective is to maximize energy to achieve higher stiffness.
It is demonstrated that shape optimization of complex porous structures while maintaining characteristic properties such as periodicity is feasible using a modified phase-field equation under both unidirectional and multidirectional loading conditions.
The ability to perform optimization while retaining periodicity, even in the direction of loading, opens up a wide range of applications, such as the precise adjustment of mechanical properties for specific loading scenarios or the development of customized lightweight structures with enhanced performance characteristics.
In Chapter 7.2.2, the unidirectionally loaded structures will be experimentally validated to confirm the efficiency and accuracy of the simulation-based optimization.

The following chapter is dedicated to the targeted structural optimization of porous structures under load using the phase-field method. In this process, the topology of the initial structures is systematically modified in a way that ensures the periodicity of the structures is preserved.

Table 5.3: Structural and mechanical properties of the original and shape-optimized gyroid structure with a volume fraction of 0.15 [–] under multiaxial loading in the specified direction with a predetermined strain ϵ and shear τ of 1 %.

Structure:	**Case 1:** xy**-direction;** yy**-direction;** zz**-direction**			**Case 2:** xy**-direction;** yy**-direction;** yz**-direction**			**Case 3:** yy**-direction;** yz**-direction**		
	V^*	Surface	$\bar{E}/E_s$ (dim.less)	V^*	Surface	$\bar{E}/E_s$ (dim.less)	V^*	Surface	$\bar{E}/E_s$ (dim.less)
Initial	0.144	6.045	0.051	0.144	6.045	0.051	0.144	6.045	0.051
Optimized	0.144	5.915	0.081	0.144	5.975	0.073	0.144	5.936	0.081

6 Phase-Field Based Structural Optimization

In the structural optimization considered here, structures are first topologically modified under specific loading conditions and subsequently shape-optimized. This optimization method enables the development of new periodic lightweight structures tailored to specific load conditions.
In the first study 6.1, gyroid structures are structurally optimized under unidirectional loading. In the following Chapter 6.2, a lattice structure is optimized under uni- and multidimensional shear loading, with the goal of generating new load-specific periodic cell structures.
Both investigations employ the modified phase-field method, as introduced in Subchapter 2.2.3. To achieve targeted topological modifications, the hole nucleation process described in Subchapter 2.2.4 is utilized.

6.1 Phase-field based load-specific structural optimization of sheet-based gyroid-structures

This chapter is based on a manuscript that is currently under review: [6].

6.1.1 Approach and method

The following compares a sheet-based gyroid structure with a porosity of approximately 80 % both through simulations and experimental analysis with two different load-modified gyroid structures.
In the first approach, a sheet-based gyroid structure with an initial porosity of 75 % is topologically modified under unidirectional loading in the linear-elastic range through the hole nucleation process, as described in the Subchapter 2.2.4. This modification is load-specific, resulting in a final porosity of 80 %.
In the second method, the comparison structure with a porosity of 80 % is directly reduced in volume by approximately 5 % through the nucleation process under unidirectional loading. Subsequently, a phase-field based shape optimization is carried out while maintaining the periodicity of the structure. Since no volume-preserving approach is applied during the shape optimization process, the volume increases. The optimization is terminated once the initial volume of the structure is restored. For the mathematical derivation of

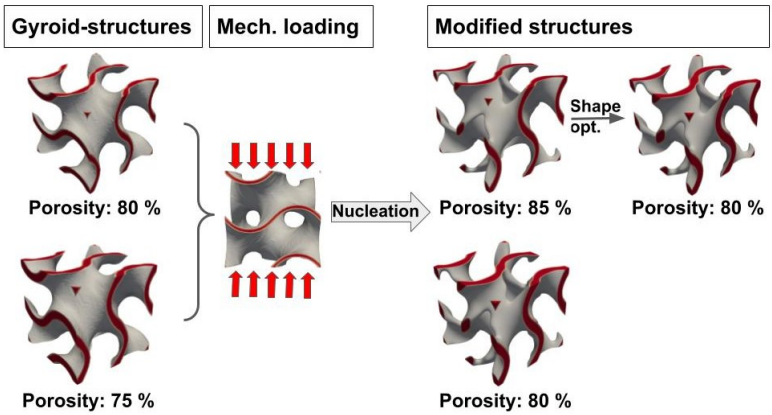

Figure 6.1: Illustration of the two load-specific structural modification approaches: 1. Topological modification of a gyroid structure with an initial porosity of 75 %; 2. Topological modification followed by shape optimization of a gyroid structure with an initial porosity of 80 %.

the phase-field based shape optimization, please refer to Subchapter 2.2.3. These two approaches to load-specific structural modification are summarized in Figure 6.1.

Subsequently, an experimental validation is conducted. The fabrication of the structures, testing, and evaluation are oriented according to the ASTM D1621 standard. The results are presented in Chapter 7.3.1.

6.1.2 Results and Discussion

Two gyroidal, topologically modified unit cells with a porosity of approximately 80 %, as shown in Figure 6.1, are compared both numerically and experimentally with an initial gyroid structure, which

also has a porosity of around 80 %. All three structures are subjected to a stress of $\sigma = -7$ in $y-$direction.

$$\bar{\sigma}_{\text{loadCase}} = \begin{bmatrix} 0 & -\sigma & 0 \\ -\sigma & 0 & 0 \\ 0 & 0 & 0 \end{bmatrix} \tag{6.1}$$

For topology modification, material is removed from the structure in less stressed areas according to the considered loading criteria. The process of volume reduction is described as *Hole Nucleation* in Chapter 2.2.4.

The gyroidal modified unit cells differ in their creation process. The first structure, referred to as $Gyroid75_{Nuc}$ (Fig. 6.2(a)), is based on a gyroidal unit cell with an initial porosity of approximately 75 %. Through the previously described hole nucleation process, the volume is reduced by 5 % under unidirectional loading in the y-direction, resulting in a final porosity of 80 % after the modification. The second modified unit cell, $Gyroid80_{NucShape}$ (Fig. 6.2(b)), originates from a gyroidal reference structure with an initial porosity of approximately 80 %. Similar to the first structure, the volume is initially reduced by 5 % through the hole nucleation process. Subsequently, the volume-reduced structure undergoes shape optimization under load in the y-direction. Since no volume-preserving method is applied during this shape optimization, the process leads to an increase in volume. The optimization is concluded once the initial

porosity of around 80 % is restored.
Figure 6.2 represents the two resulting modified structures.

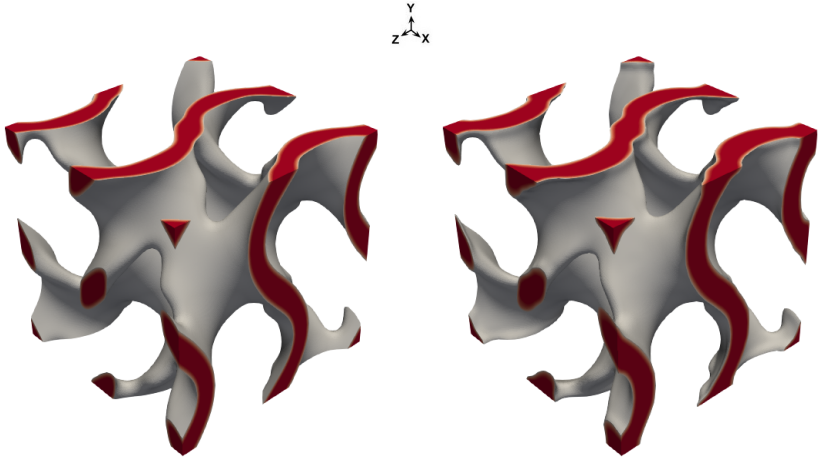

(a) $Gyroid75_{Nuc}$ **(b)** $Gyroid80_{NucShape}$

Figure 6.2: Representation of the modified structures with initial porosities of a) 75 % and b) 80 %.

Although two different topology-modification approaches were used, both structures exhibit remarkable similarities in the final outcome. Since the differences between the modified gyroid structures are barely noticeable, the volume fraction along the x-axis is plotted for a clearer representation of the structural modifications. Figure 6.3 compares the $Gyroid75_{Nuc}$ and $Gyroid80_{NucShape}$ structures with the unmodified gyroid unit cell.

In the diagram, the solid black line represents the gyroid unit cell with a porosity of 80 %, while the blue dashed line corresponds to the $Gyroid75_{Nuc}$ structure, and the green dotted line represents the

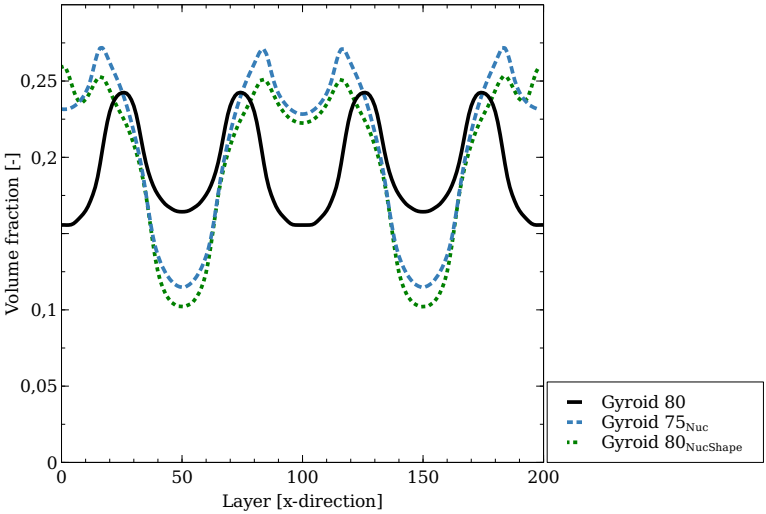

Figure 6.3: Volume redistribution of the structure-modified $Gyroid75_{Nuc}$ and $Gyroid80_{NucShape}$ compared to the gyroid unit cell (black solid line).

$Gyroid80_{NucShape}$ structure. Upon analyzing the topologically modified structures, it becomes evident that the volume reduction in both structures primarily occurs in the layers positioned along the x-axis at approximately 50 and 150, which correspond to the locations of the crossbars. This reduction in the crossbars is clearly observed in Figure 6.2. For better visualization, the areas where material was removed from the initial gyroid unit cell are highlighted in Figure 6.4.

Additionally, the volume distribution in Figure 6.2 shows that the vertical columns, loaded in the y-direction, remain intact in the $Gyroid75_{Nuc}$ structure and are reinforced in the $Gyroid80_{NucShape}$

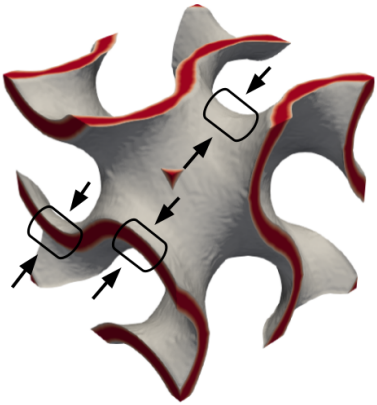

Figure 6.4: Highlighted areas of a gyroid structure with 80 % porosity where material was removed during the topology modification process.

structure during the shape optimization process. Despite the similarities in the volume distribution of both structures, slight differences in characteristic features are identified.

As shown in Table 6.1, the structures exhibit a volume fraction of approximately 20 %, corresponding to a porosity of around 80 %. This consistent porosity allows for a better comparison between the structures.

	Gyroid80	$Gyroid75_{Nuc}$	$Gyroid80_{NucShape}$
Volume fraction	0.192	0.207	0.197
Surface Area	6.193	5.151	5.101

Table 6.1: Representation of the surface area and volume fraction of the respective structures.

In the comparative analysis of surface areas, it becomes evident that the initial gyroid unit cell exhibits the largest surface area, followed by the modified structure $Gyroid75_{Nuc}$. This indicates that the phase-field based, load-specific optimization leads to a reduction in surface area.
Despite these differences in surface reduction, a similar increase in the effective elastic modulus in the corresponding loading direction (E_{yy}) is achieved, as shown in Table 6.2. For independent and improved comparability, the simulation results are presented in a non-dimensionalized form. The modulus of elasticity is given in dimensionless form by E/E_s. In Table 6.2, the modulus of elasticity in the main load direction is marked in bold. This highlights the efficiency of phase-field based optimization in enhancing mechanical properties, particularly the elastic modulus, even across different topological structures.

	Gyroid80	$Gyroid75_{Nuc}$	$Gyroid80_{NucShape}$
E_{xx}	0.067	0.023	0.022
E_{yy}	**0.067**	**0.091**	**0.089**
E_{zz}	0.067	0.022	0.020

Table 6.2: Comparison of the effective modulus of elasticity in the $x-$, $y-$ and $z-$ directions.

By topologically modifying the gyroid unit cell with an original porosity of 75 % ($Gyroid75_{Nuc}$), an increase in the effective modulus of elasticity in the load direction (E_{yy}) of about 35 % is achieved compared to the unmodified gyroid unit cell of the same porosity. For

the structure $Gyroid80_{NucShape}$, which initially undergoes a volume reduction of 5 % due to the nucleation process and then a further volume increase of 5 % due to the shape optimization, the increase in the effective modulus of elasticity of 32 % is in a similar range to the structure $Gyroid80_{NucShape}$.
However, it is observed that the optimization process in the non-loaded directions results in a significant reduction in the effective modulus of elasticity, which is more than half of the original value. This reduction is due to the previously described reduction of the transverse beams in the non-loaded directions, which leads to a pronounced anisotropic behavior of the cell. In comparison, the original gyroidal unit cell exhibits almost isotropic behavior, with the effective modulus of elasticity being in a similar range in all load directions.
The next step is to validate the simulatively generated structures and data experimentally, which can be found in Chapter 7.3.1.

6.1.3 Conclusion

Two alternative phase-field based approaches for modifying the topology of complex porous structures under load were investigated. While preserving the periodicity of the unit cells, both approaches yielded similar volume fractions and resulted in an increase of the effective Young's modulus in the respective optimization direction by approximately 32 %. The topological modification led to a reduction in the surface area of the modified structures compared to the initial geometry.
Experimental validation of the numerically optimized structures is

detailed in Chapter 7.3.1.

In addition to the application of phase-field based structural optimization to TPMS structures, the next chapter aims to optimize simple three-dimensional cross-lattice structures under various loading conditions. The objective is to devise novel load-specific three-dimensional periodic cell structures.

6.2 Phase-field based structural optimization of 3D cross-lattice structure to lightweight periodic lattice structures

> This chapter is based on a manuscript that is currently under review: [7]

6.2.1 Approach and Methode

In the following, the periodic cross-lattice structure with a volume fraction of approximately 75 %, shown in Figure 6.5, is structure optimized for load specific shear cases.

Regarding the topology adjustment, the volume of the shear-loaded structures are first reduced to a volume fraction of approximately 35 % through a process called *hole nucleation* (see Subchapter 2.2.4). Subsequently, the volume-reduced and topology-modified structure is shape-optimized while maintaining its volume fraction.

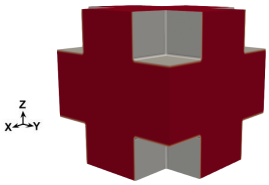

(a) $\rho = 75\,\%$

Figure 6.5: The periodic cross-lattice structure with a volume fraction of 75 % serves as the initial structure for the optimization process.

The goal of this optimization is to achieve load-specific periodic cell structures while simultaneously increasing the shear modulus G for each load case. Both the hole nucleation process and the subsequent shape optimization are treated as a two-phase phase-field problem with a solid phase (ϕ_s) and a porous phase (ϕ_p), to which a zero stiffness is assigned. The porous phase represents the stress-free surrounding structure. For the subsequent shape optimization process, the approach described in Subchapter 2.2.2 will be used.

The cross-lattice structure to be optimized is considered in a three-dimensional domain Ω with 200 cells in each spatial direction. The simulation is conducted within the linear elastic range. Additionally, isotropic material constants are assumed in the simulation process. According to the theory of elasticity, it is sufficient to use two independent constants to describe the stress-strain relationships [55].
In this study, the focus is on the variation of the shear modulus G since the structures are optimized under pure shear loading (uni- and multidirectional).

6.2.2 Results and Discussion

The initial cross-lattice structure, with a volume fraction of 75 %, is subjected to volume reduction under specific shear load criteria. Material is removed from the less-loaded regions, so that the resulting structure achieves a volume fraction of approximately 35 %. Since the structures are subjected to pure shear loading, the aim of the present work is to maximize the effective shear modulus of structures under the given load conditions. After that, a shape optimization of the topology-modified structure takes place.

6.2.2.1 Structure optimization under shear loading scenarios

In order to optimize the structure under scenarios of shear loading, the 3D lattice structures are initially modified exclusively in terms of topology. Subsequently, an additional shape optimization of these topological structures is performed, resulting in a two-stage optimization process. Finally, the optimized cells are compared with reference structures in order to evaluate the effectiveness of the structural optimization.

Topology-modified structures The cross-lattice structure is subjected to three cases of uni- and multidirectional shear loads, defined by the stress tensors in Eq. 6.2, and volume reduction is performed according to the loading scenarios. A stress of $\sigma = -7$ is applied in each respective loading direction.

$$\bar{\sigma}_{\text{case1}} = \begin{bmatrix} 0 & -\sigma & 0 \\ -\sigma & 0 & 0 \\ 0 & 0 & 0 \end{bmatrix}, \quad \bar{\sigma}_{\text{case2}} = \begin{bmatrix} 0 & -\sigma & -\sigma \\ -\sigma & 0 & 0 \\ -\sigma & 0 & 0 \end{bmatrix}, \quad \bar{\sigma}_{\text{case3}} = \begin{bmatrix} 0 & -\sigma & -\sigma \\ -\sigma & 0 & -\sigma \\ -\sigma & -\sigma & 0 \end{bmatrix} \tag{6.2}$$

For volume reduction, material was removed from the cross-lattice structure at less stressed areas according to the three considered loading criteria. The resulting structures are depicted from various perspectives in Figure 6.6.

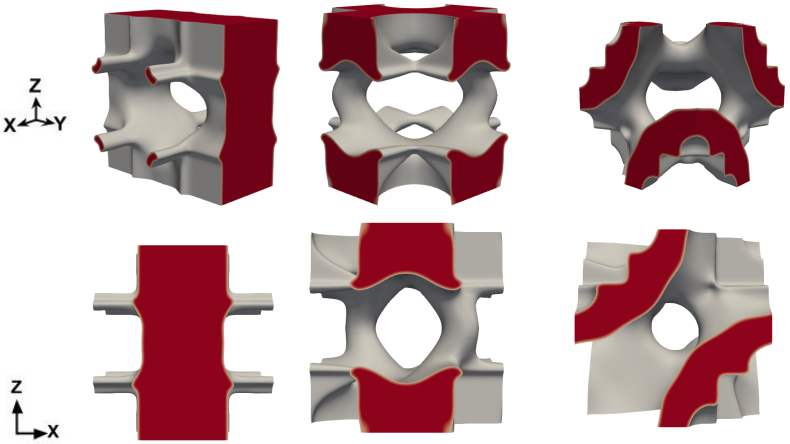

(a) Case 1: Unidirectional shear loading in the x-direction.

(b) Case 2: Multidirectional shear loading in the x- and y-directions.

(c) Case 3: Multidirectional shear loading in the x-,y- and z-directions.

Figure 6.6: Volume-reduced and topologically modified cross structure under different shear loading criteria (xyz- and xz-view).

The volume reduction step leads to periodic and symmetrical structures for the three considered load cases. It is evident that the volume is reduced according to the loading orientation. As can be seen from the topology-modified structure under shear loading conditions of case 1, a more pronounced anisotropic geometry is present and remains at a later stage. In contrast, the multi-directional shear load case 3 results in a curved lattice structure that bears certain similarities to triply periodic minimal surfaces. The structure in case 2 can be identified as an intermediate structure between case 1 and case 3.

These observations highlight the strong dependence of the geometry of the porous structures on the specific loading orientation. In unidirectional loading applications as case 1, where the load is applied in a single direction, the structures tend to develop anisotropic material behavior. This occurs because material is primarily removed from areas not exposed to the main loading direction, leading to an uneven distribution of porosity. In contrast, three-dimensional loading as in case 3, where the load is applied simultaneously in multiple directions, result in a more uniform and symmetric pore structure. These structures often resemble triply periodic minimal surfaces structures, known for their beneficial mechanical properties and even material distribution.

The loading case 2, representing a combination of unidirectional and multidirectional loading, results in an intermediate structure. This structure exhibits characteristics of both unidirectional and three-dimensional loading cases, providing insights into the transitional mechanisms between different loading scenarios.

All structures have a volume fraction of 36 %. The corresponding initial surface areas of the structures are computationally determined and listed in Table 6.3.

Table 6.3: Volume fraction of the porous structures and their corresponding surface area.

Modified structure type	Volume fraction	Surface area
Unidirectional	0.36	2.77
Bidirectional	0.36	3.54
Tridirectional	0.36	3.70

The modified structure type of 'unidirectional' represents the unidirectionally load-modified structure, which is shown in Figure 6.6.a. Similarly, 'bidirectional' corresponds to the bidirectionally load-modified structure (see 6.6.b), and 'tridirectional' describes the modified structure subjected to loading in all directions (see 6.6.c). This labeling will be consistently maintained throughout the following sections.
While the volume fraction of the three structures remains constant, there is a significant difference in the surface area. The resulting porous structure from the unidirectional loading case has the smallest surface area. In contrast, the structure subjected to shear loading from all directions shows approximately a 33 % larger surface area. The value of the surface area determined for case 2 lies between the other two cases.
Following [35], the subsequent results are given in normalized manner. Thereby, the effective shear modulus is normalized by its Voigt bound which represents an upper limit for the effective stiffness in

composite materials [56] and is given by the arithmetic mean of the shear moduli of the involved phases with respect to the corresponding volume fraction ($\bar{G} = G/(5480 * 0.35)$). Table 6.4 lists the normalized effective shear modulus $\bar{G}$ of the structures for the respective loading cases and their average $\bar{G}_{Av}$.

Table 6.4: Behavior of the normalized effective shear modulus $\bar{G}$ of load-modified cross-lattice structures under different loading conditions and the average (av) of all three cases.

Modified structure type \ Shear type	Uni-directional	Bi-directional	Tri-directional	Av
Unidirectional	0.19	0.0098	0.0085	0.069
Bidirectional	0.05	0.06	0.07	0.06
Tridirectional	0.1	0.13	0.22	0.15

Thereby, the modified structure types of the specific loading cases are subjected to all three loads (uni-, bi- and tridirectional) to investigate the influence of the modification regarding one load case on the effective stiffness for other load cases. The adjusted structures for case 1 and case 3 exhibit the highest $\bar{G}$ of $0.19\,[-]$ (Unidirectional) (case 1), Unidirectional) and $0.22\,[-]$ (tridirectional (case 3), tridirectional) for their respective loading conditions compared to the other structures.

The orientation of the volume in response to the specific loading scenario is most clearly demonstrated by case 1. For the adjusted loading case, the normalized effective shear modulus $\bar{G}$ is $0.19\,[-]$ (unidirectional (case 1), Unidirectional), whereas it is significantly lower for multidirectional loading cases, with values of $0.0098\,[-]$ (unidirectional (case 1), bidirectional) and $0.0085\,[-]$ (unidirectional (case 1), tridirectional). Interestingly, the structure modified for the

two-dimensional shear loading case exhibits a higher modulus for the three-dimensional case of $\bar{G} = 0.07$ than for the optimized two-dimensional shear loading case of $\bar{G} = 0.06$. Among the structures analyzed, the structure modified for case 2 exhibits the smallest deviations in the normalized effective shear modulus $\bar{G}$ across the various load cases considered. This suggests that this structure demonstrates the best isotropic behavior, as it provides the most uniform mechanical response under different loading scenarios.
The structure from case 3 with shear moduli of $\bar{G} = 0.1, 0.13, 0.22$ shows the best performance over all three loading scenarios. It has still a relatively high shear modulus for the loads, it was not modified for, and an approximately double as high normalized effective shear modulus in the case 3. This observation is confirmed by the average value ($\bar{G}_{Av}$) across all three loading cases. Overall, the structure modified for case 3 shows the highest mean value. Although the shear modulus for case 1 is relatively high in the modified loading direction, the values in the other loading directions are significantly lower, which explains the correspondingly lower average value.
In the following subsection, the topologically adapted structures will be shape optimized for the respective modified loading directions.

Shape optimization The previously topology-altered structures are now shape-optimized under specific shear loading conditions. The shape optimization process is terminated once the change in the objective function after each simulation step is reduced to less than the fifth decimal place after the decimal point.
The phase-field based shape optimization process aims to further

optimize the structures according to the respective loading directions. During this process, the volumes of the structure keep constant while redistributing the volume. Volume is removed from less-loaded regions and added to more heavily loaded areas. Nevertheless, the structure's periodicity is maintained. In Figure 6.7, the shape-optimized cell structures are shown in their shape-optimized state.

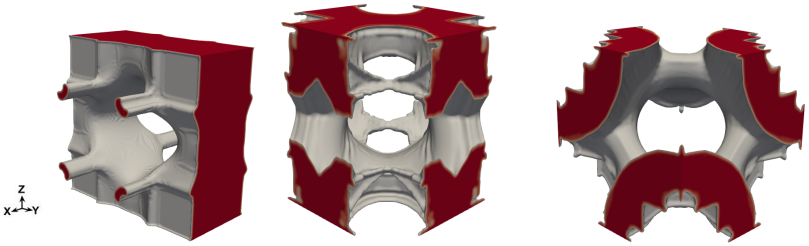

(a) Case 1: Unidirectional shear loading in the x-direction.

(b) Case 2: Multidirectional shear loading in the x- and y-directions.

(c) Case 3: Multidirectional shear loading in the x-,y- and z-directions.

Figure 6.7: Shape optimization of topologically modified cross structure under different shear loading criteria (xyz-view).

Since the volume redistribution is not fully recognizable in Figure 6.7, the volume fraction along the x-axis of the respective structures is presented in more detail in the following Figures 6.8-6.10.

This detailed representation allows for a more precise analysis of the volume distribution within the structures, which has corresponding impacts on the mechanical properties of the structures.
The red dashed line represents the initial topology-adjusted structure, while the subsequent shape-optimized structure is indicated by

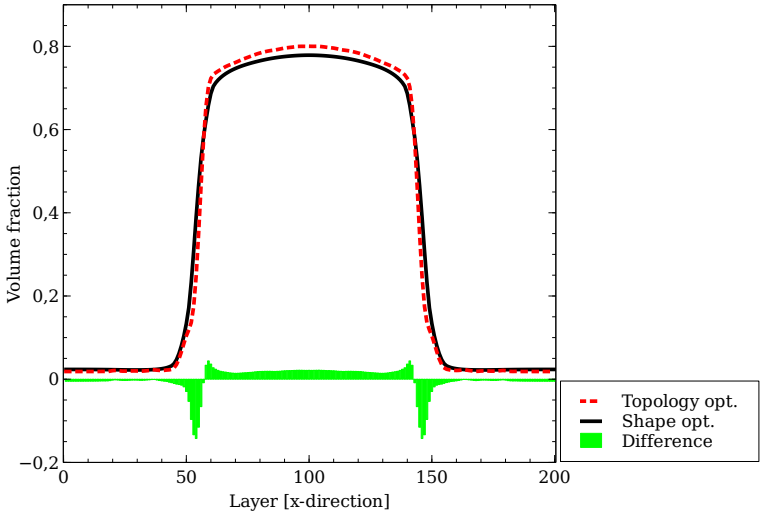

Figure 6.8: Volume redistribution through the shape optimization process of the optimized structure for case 1.

a solid black line. The difference in volume redistribution is illustrated by the bar chart. It is evident that for the structure optimized for the one-dimensional shear loading case (case 1), the volume redistribution due to the optimization process is minimal, whereas the most significant redistribution is observed in case 2. This also explains why the largest percentage change in surface area of about 22 %, from the initial 3.54 (see Tab 6.3) 4.33 (see Tab 6.5), is observed in this case. The table also reveals that the shape-optimized structure for case 2 has the largest surface among the three structures considered.

Upon revisiting the normalized G-modulus from Table 6.4 for the topologically altered structures, it is evident that the topologically altered structure in case 3 exhibits a higher normalized G-modulus

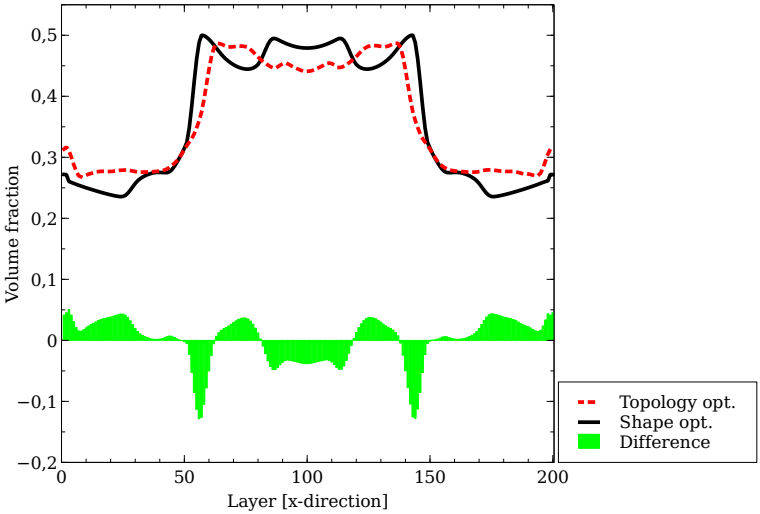

Figure 6.9: Volume redistribution through the shape optimization process of the optimized structure for case 2.

Table 6.5: Volume fraction of the shape optimized porous structures, as well as their corresponding surface area.

Shape modified structure type	Volume fraction	Surface area
Unidirectional	0.36	3.01
Bidirectional	0.36	4.33
Tridirectional	0.36	3.96

for the loading scenario in case 2 than the structure specifically optimized for this loading case. The subsequent shape optimization process enabled all structures to be brought into a more energetically favorable state. Consequently, after the shape optimization process, all three structures represent the most favorable design for their respective optimized loading conditions. The corresponding

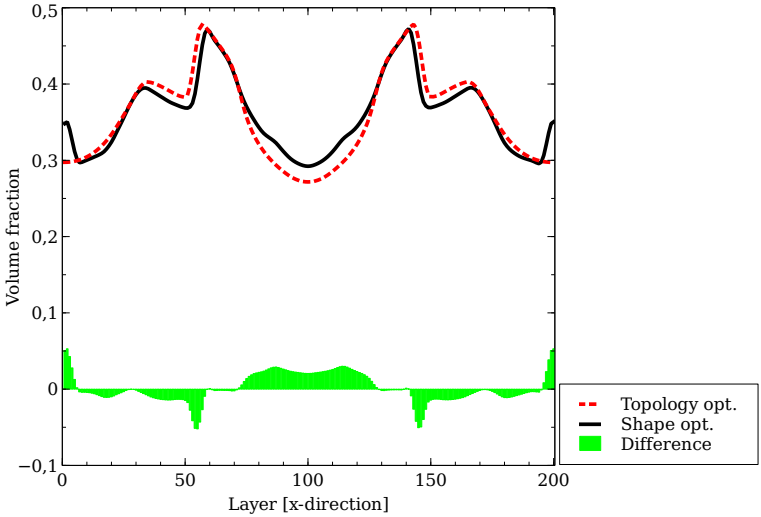

Figure 6.10: Volume redistribution through the shape optimization process of the optimized structure for case 3.

G-modulus for each of the shape-optimized structures and their corresponding loading conditions can be found in Table 6.6.

Table 6.6: Behavior of the normalized shear modulus $\bar{G}$ of the load-altered and subsequently shape-optimized cross-lattice structures under various loading conditions and the average (Av) of all three cases.

Shape modified structure type \ Shear type	Uni-directional	Bi-directional	Tri-directional	Av
Case 1 (Unidirectional)	0.22	0.008	0.007	0.078
Case 2 (Bidirectional)	0.07	0.22	0.09	0.126
Case 3 (Tridirectional)	0.11	0.14	0.26	0.17

Although the volume redistribution is partly relatively minor, an increase in the shear modulus $\bar{G}$ was achieved compared to the topologically altered structure for the respective optimized loading case.

In the structure optimized for the unidirectional loading scenario (case 1), the volume redistribution leads to an increase in the $\bar{G}$-modulus, from 0.19 [−] (see Tab. 6.4; (Unidirectional (case 1), Unidirectional) to 0.22 [−] (see Tab. 6.6; Unidirectional (case 1), Unidirectional), representing an approximate 15 % increase in the direction of optimization. However, this also results in a decrease in the effective shear modulus for multidirectional loading orientations. In contrast, for the other two structures, the volume redistribution results in an enhancement of the shear modulus across all considered shear loading scenarios compared to the load-specific topologically altered baseline structure.
The highest increase was observed in case 2, where the volume redistribution leads to an increase in the shear modulus of more than 200 %.
In the structure optimized for the unidirectional loading scenario (case 1), the volume redistribution leads, on one hand, to an increase in the $\bar{G}$-modulus, but on the other hand, also results in a decrease in the effective shear modulus for multidirectional loading orientations. In contrast, for the other two structures, the volume redistribution results in an enhancement of the shear modulus across all considered shear loading scenarios compared to the load-specific topologically altered baseline structure.
The highest increase was observed in case 2, where the volume redistribution leads to an increase in the shear modulus of more than 200 %.
In case 3, shape optimization achieved an additional increase in the modulus of approximately 18 % in the direction of the applied load. As can be seen from the average value, the shape-optimized structure for loading case 3 still demonstrates the overall most beneficial

behavior across the considered load cases.
From these observations, it can be concluded that topology modification is a promising tool for developing new, load-specific foundational structures. The subsequent shape optimization process serves, depending on the efficiency of the previously determined topology, either for fine-tuning for the specific loading case or for further optimization of the structure. In addition, in the cases considered, shape optimization results in an increase in the surface area, although the surface area is not part of the optimization process.
Besides the optimized lattice structures for pure shear loading cases, it is also important to analyze comparative structures for the previously considered loading scenarios. This allows for a comprehensive assessment of the performance and efficiency of the load-specific, newly generated lattice structures through the relatively unexplored phase-field based structural optimization for lattice structures.
In the next step, these optimized cells will be compared with other structures.

6.2.2.2 Comparative structures

For the comparison of the newly generated periodic structures, which were specifically optimized for various shear loading conditions, two triply periodic minimal surfaces (TPMS) are selected: the sheet-based gyroid (see Fig. 6.11.a) and the sheet-based primitive structure (see Fig. 6.11.b). This selection is based on the observed similarity of the optimized structure with the minimal surfaces case 3. Additionally, a structure derived from the topology-change cross-lattice structure, but optimized for the hydrostatic loading case (see Fig. 6.11.c),

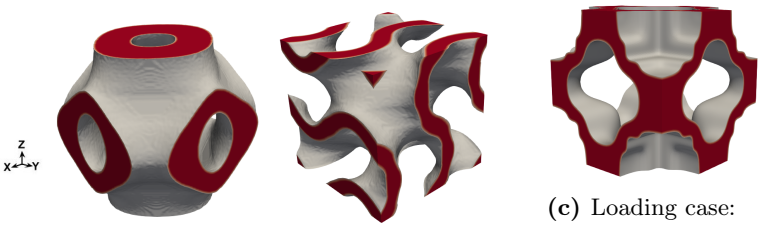

(a) Primitiv-Structure

(b) Gyroid-Structure

(c) Loading case: Hydrostatic loading scenario

Figure 6.11: Comparison structures with a volume fraction of about 35 %

is included in the analysis. This structure also exhibits similarities to triply periodic minimal surface structures. The finding that optimization under uniform loading conditions results in TPMS-like structures is supported by the results of [57]. In this study, a hollow tetrahedral cell structure was optimized with respect to its isotropic effective stiffness, further confirming the similarity of the resulting structure to TPMS structures.

All three structures have a volume fraction of about 35 %, similar to the previously generated structures. However, the surface area of these three structures is higher than that of the structures specifically optimized for shear loading cases, as can be seen from Table 6.7 with the gyroid structure having the largest surface area of 6.16.

The normalized effective $\bar{G}$-moduli of the comparison structures for the uni- and multidirectional shear loading cases applied to the cross-lattice structure are listed in Table 6.8.

In the mechanical analysis of the shear modulus $\bar{G}$ of the comparative structures, it is observed that the primitive structure exhibits the highest values under both, unidirectional and multidirectional

Table 6.7: Volume fraction of the porous comparison structures, as well as their respective surface area.

Comparison structure	Volume fraction	Surface area
Primitive	0.34	4.60
Gyroid	0.34	6.16
Hydrostatic	0.34	4.42

Table 6.8: Normalized effective shear modulus $\bar{G}$ of comparison structures and the average (Av) of all three cases.

Comparison structure \ Shear type	Uni-directional	Bi-directional	Tri-directional	Av
Primitive	0.22	0.22	0.21	0.21
Gyroid	0.17	0.17	0.17	0.17
Hydriostatic	0.15	0.15	0.15	0.15

shear loads compared to the other two examined structures. However, when comparing the primitive structure with the newly generated structures, it becomes evident that the $\bar{G}$-moduli for the newly generated structures in load cases 1 and 2 are in a similar range. This indicates that the new structures perform comparably to the primitive structure in these load cases, and the mechanical properties compete well with already established structures.

Notably, the newly generated and shape-optimized structure for the three-dimensional loading scenario (case 3) can exhibit an effective $\bar{G}$-modulus that is up to 23 % higher. This shows, that the targeted optimization for a specific loading case can achieve the stiffness. However, it must be noted that the shear modulus for other loading cases of the modified structure in case 3 is nearly halved.

Nevertheless, if only the specified loading case is of relevance, this load-specific optimization may still prove advantageous.
When examining the other comparative structures: Gyroid and hydrostatically modified structure are detected no significant fluctuations in the $\bar{G}$-moduli across the different loading cases. Although the structure optimized for case 3 also features a uniformly periodic arrangement, the effective $\bar{G}$-modulus has nearly halved between the optimized loading case (case 3) and the non-optimized loading cases.
To sum up, the phase-field based load-specific optimization enables the generation and optimization of new structures. The superior performance of this newly generated structure under multidimensional loading conditions underscores the potential of phase-field based optimization for developing more efficient structures with improved mechanical performance. While the initial load-specific topology modification creates the base structure, the subsequent shape optimization process refines the structure.
This highlights the potential of the structural optimization process using phase-field based optimization and demonstrates the capability to computationally develop new, load-specifically designed structures. In particular, it underscores the ability of phase-field based optimization to create structures tailored to specific loading requirements.

6.2.3 Conclusion

In the first part of this study, a three-dimensional lattice cross-structure with a volume fraction of about 75 % was both topology-

and shape-optimized for various shear loading cases. Initially, material was removed from the less-stressed areas of the original structure under uni- and multidirectional shear loads, resulting in a new, periodic, and topologically altered structure with a volume fraction of approximately 35 %. Analysis of the shear modulus for the different loading directions revealed that the shear modulus was not optimally aligned for some structures. The subsequent phase-field based shape optimization process led to a stress-specific volume redistribution, resulting in an increased shear modulus for each structure tailored to its respective loading case.
In the second part of the study, two well-established TPMS (Triply Periodic Minimal Surface) structures from the scientific literature, namely the sheet-based gyroid and the primitive structure, as well as a hydrostatically topology-altered lattice cross-structure, were used as comparative structures. It was observed that the primitive structure exhibited the highest shear modulus under one-dimensional and two-dimensional shear loading cases. In contrast, the shape- and topology-optimized structure achieved the highest shear modulus under three-dimensional shear loading conditions.
These results highlight that the combination of phase-field based topology and shape optimization represents a promising approach for creating new mechanical periodic structures tailored to specific loading conditions.
The study effectively demonstrated the approach, concept, and potential for generating stress-specific periodic porous structures using a phase-field based structural optimization process.

To ensure the reliability and effectiveness of phase-field based shape

and structural optimization methods, experimental validation is essential. Therefore, an experimental validation of phase-field based shape and structure optimization is performed in the following chapter.

7 Experimental Consideration

In the following chapter, the TPMS-structures that were created and optimized through simulations in chapters 4 to 6 will be fabricated and experimentally examined.
This study focuses on phase-field based, load-specific structures, with a comparison between simulation-based and experimental data. Initially, the manually optimized structures will be considered, followed by the validation of the phase-field based shape-optimized structures and finally the structure-optimized structures.

7.1 Experimental validation of manual shape optimized structures

The following experimental validation is motivated by the simulation study of the manually optimized gyroid structures presented in Chapter 4.

7.1.1 Energy absorption capability of graded and non-graded sheet-based gyroid structures fabricated by microcast processing

This chapter is based on the publication: [1]

7.1.1.1 Structure generation

This chapter experimentally investigates $10x10x10$-cell gyroid structures that have been modified through porosity gradients. The gyroid cells to be examined here are generated using the MATLAB code presented in Chapter 4. As described before, for structures with gradients, a maximum (starting) porosity and a minimum (target) porosity are specified. Starting from the maximum porosity, the structure is thickened in either a linear or quadratic progression. The quadratic progression represents a quasi inverted parabola (see Figure 7.1).

The diagram shows the target and actual function of the structure, with a linear and quadratic porosity gradient over the cell size (x-axis) and the porosity (y-axis). Here, the actual and target porosity deviate slightly from each other. The course of the function shows that the structure with the quadratic gradient is thickened more slowly than the structure with the linear gradient. The thickening of the structures takes place in the z-direction. The specimens have a size of 25 x 25 x 25 mm^3, with 10 cells per spatial direction.
For the following analysis, the sample dimensions and test method

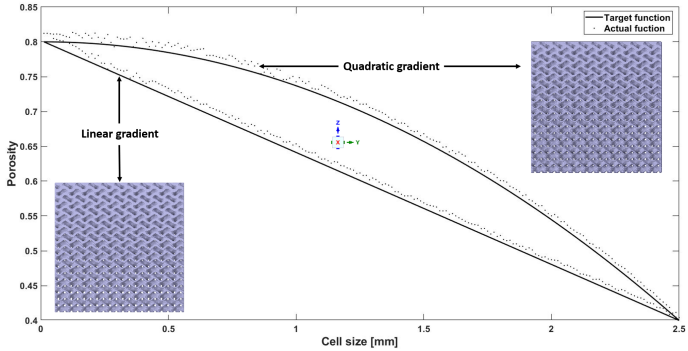

Figure 7.1: Function curve of gyroid structures with a linear and quadratic porosity of the actual (points) and target porosity function (line).

are based on the international standard ISO 13314:2011 [42]. Samples with porosities from 40 % to 80 %, with a quadratic and linear gradient, and with a constant porosity of 40 %, 60 % and 80 % are generated. Table 7.1 shows the calculated porosity from the stl files. Formula 1.4 is used to calculate the porosity.

Table 7.1: Theoretical porosity of the samples.

Sample type	**Calculated average porosity** [%]
Constant 40	42
Linear 40-80	56
Constant 60	57
Quadratic 40-80	63
Constant 80	76

As shown in Table 7.1, three samples within a similar porosity range (linear 40-80, quadratic 40-80 and constant 60) are compared. The structures with a constant porosity of 60 % and the structures with linear porosities from 40 % to 80 % theoretically have an average equal porosity of 60 %. The average porosity of the structures with a quadratic gradient is slightly higher than 60 %, which is due to the fact that the structures with a quadratic gradient thicken more slowly, as shown by the quadratic gradient function in Figure 7.1. In general, the porosity calculated from the stl files deviates from the theoretical porosity by up to 4 percentage points. On the one hand, this is caused by the slight deviation that occurred during the generation of the structures and, on the other hand, by the tessellation of the stl files, which affects the accuracy [58]. In addition, the two extreme values 'constant 40' and 'constant 80' are considered.

7.1.1.2 Structure manufacturing

The gyroid structures are manufactured using the microcasting process as described in Chapter 3.2 by the company *Nonnenmacher GmbH, Ölbronn Dürrn, Germany* and are made of the aluminum alloy *AlSi7Mg0.6* ($\rho = 2.68\,\mathrm{g/cm^3}$, $E = 59\,\mathrm{GPa}$). Figure 7.2 shows the surface of the computer-generated model of the gyroid structure with a linear gradient and porosities from 80 % to 40 %, compared to the corresponding cast model. This shows that the cast is so accurate that the model and the cast can merge seamlessly.

Each casting structure has sprue points from the connection to the casting tree, which are marked in the casting gyroid cube with a

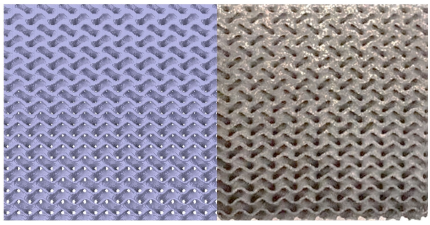

Figure 7.2: Computer-based model compared to the cast model of a gyroid structure, with a linear porosity from 80 % to 40 %.

linear gradient, shown in Figure 7.3. These casting points must be taken into account during the subsequent component inspection.

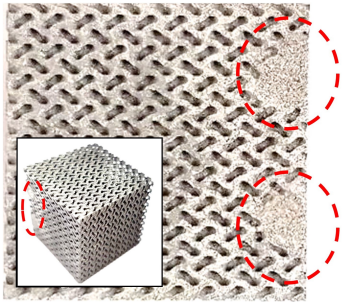

Figure 7.3: Gyroid casting structure with marked sprue points from the casting tree.

The presence of the sprue points partially explains why some samples are slightly heavier than the theoretically calculated weight, as shown in Table 7.2. Table 7.2 shows the theoretical and actual weights of the samples and the weight deviation in percent. Here, the actual weight of the samples either deviates positively, if the sample is heavier than the theoretical weight, or negatively, if the actual weight is lighter than the theoretical weight.

Table 7.2: Theoretical and actual weight of the samples.

Sample type	Sample number	Theoretical weight [g]	Actual weight [g]	Deviation [%]
Constant 40	P1	24.03	24.71	2.82
	P2	24.03	24.78	3.12
	P3	24.03	24.87	3.50
	P4	24.03	24.95	3.83
	P5	24.03	25.49	6.08
Linear 40-80	P1	18.42	17.52	-4,89
	P2	18.42	18.70	1.52
	P3	18.42	17.72	-3.80
	P4	18.42	17.74	-3.69
	P5	18.42	17.92	-2.71
Constant 60	P1	17.77	16.89	-5,21
	P2	17.77	17.74	-0,17
	P3	17.77	17.77	0.00
	P4	17.77	17.05	-4,22
	P5	17.77	17.80	0.17
Quadr. 40-80	P1	15.45	16.10	4.21
	P2	15.45	14.47	-6.77
	P3	15.45	15.30	-0.98
	P4	15.45	15.91	2.98
	P5	15.45	15.68	1.49
Constant 80	P1	9.91	9.28	-6.79
	P2	9.91	8.17	-21.30
	P3	9.91	9.13	-8.54
	P4	9.91	8.83	-12.23
	P5	9.91	7.81	-26.88

When considering the theoretical and actual weight of the samples, the largest percentage difference of about (-) 28 % is found at the constant porosity of 80 %. However, since these samples are also in the low weight range, a percentage deviation of 28 % means an absolute value of 2.1 g. Taking these values into account, the manufacturing process provides test samples with a good quality. For the gyroid structures with a constant porosity of 80 %, the samples all deviate negatively from the theoretical weight. This is due to the fact that, because of their filigree structure, the edges and corners have already broken off before the test (see Fig. 7.4).

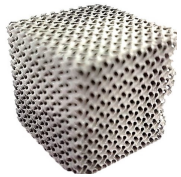

Figure 7.4: Missing mass substance of the gyroid structure with a constant porosity of 80 %.

In contrast, a positive deviation is consistently observed for the gyroid structure with a constant porosity of 40 %, which means that the specimens are heavier than their theoretical value. This may be due to the sprue points, as the visual inspection did not reveal any significant gypsum residues in the structure. The uniform structure with a porosity of 60 % shows the least variation. For the structures with a linear and a quadratic porosity, the deviations from the theoretical values are sometimes negative and sometimes positive.

7.1.1.3 Testing

To investigate the energy absorption capacity, compression tests were carried out with the machine '*inspekt 200*', from the company '*Hegewald & Peschke*'. For all specimens, the crosshead speed was 0.025 mm/s (*initial length (*25 mm*) * compression speed (*$10^{-3}s^{-1}$*)*). Five gyroid structures of each type were tested. The specimens were placed on the lower pressure plate, so that the sprue points were rested vertically on the plate. The compression tests of the structures with a constant porosity of 40 % had to be stopped prematurely, because the punch of the machine got into a one-sided oblique position and wedged. Therefore, it was not possible to calculate the energy absorption capacity of these samples. The wedging during the compression test is shown in Figure 7.5.

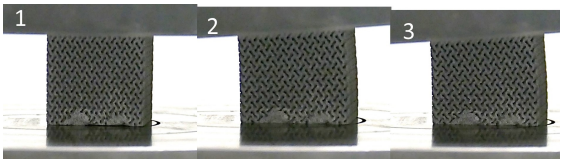

Figure 7.5: Course of the compression test (gyroid; constant 40 %): 1. Initial state; 2. Unilateral fracture; 3. Wedging

7.1.1.4 Results and discussion

The results of the compression test of the stress-strain diagram are shown in Figure 7.6. The figure shows five samples for each gyroid type (see Table 7.2).

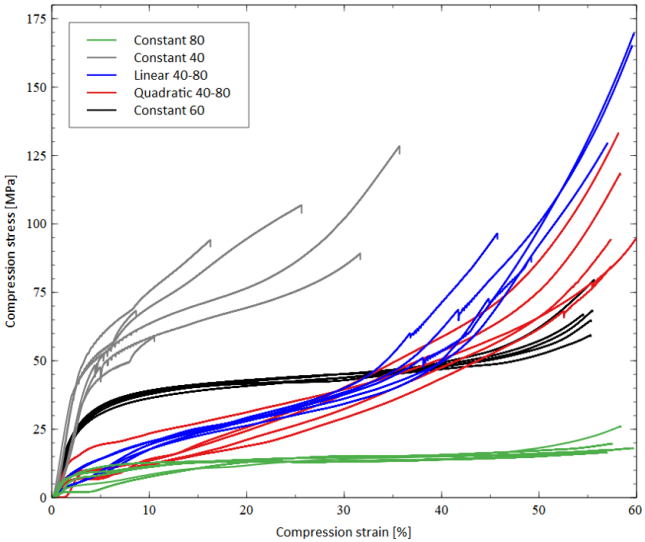

Figure 7.6: Stress-strain diagram of tested structures.

As mentioned above, no statement about the energy absorption capacity could be made for the structures with a low porosity (40 %), because the mechanical tests had to be stopped before reaching the first peak, due to a one-sided failure of the samples. However, statements can be made about the layer collapse in the stress-strain diagrams. Compared to the other structures, the layer collapse occurred more frequently and in a more intense form, even before reaching the first peak of 50 %, which is shown in the stress-strain curve, by the sudden drop in stress. In the other structures, the layer collapsed after this peak. In the gyroid structures with constant porosities of 80 % and 60 %, minor cell collapses are regularly observed on the

plateau. Minor stress drops are also evident in the gradient structures. In Figure 7.7, a structure of each gyroid type is shown for better clarity and the layer collapse is marked.

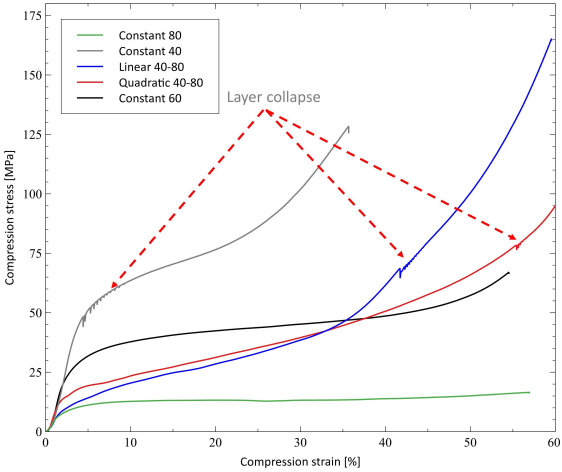

Figure 7.7: Stress-strain diagram - Layer collapse

Ashby's [59] observation that the initial loading curve is not linear can be shared for all samples. This is due to the fact that some cells already fail at low loads. In addition, Ashby describes that an ideal energy absorber is characterized by its long plateau (a long, flat stress-strain curve). In use cases, the plateau stress should be less than the stress of the object being protected [59]. According to the ISO 13314:2011 standard [42], the energy absorption per unit is calculated from the area under the curve up to a strain of 50 %, as shown in the following equation 7.1:

$$W = \int_{\epsilon=0}^{\epsilon(50\,\%)} \sigma(\epsilon) d\epsilon \quad [MJ/m^3] \tag{7.1}$$

The cumulative energy absorption per unit volume, W, is composed of the strain ϵ [%] and the corresponding stress σ $[MPa]$ during the compression test.
According to Ashby, the samples with a constant porosity of 80 % and 60 % show the ideal course of an energy absorber. The function curve of gyroid structures with a quadratic and linear plateau is not as clearly visible, but has a higher energy absorption potential. Table 7.3 shows the calculated energy absorption per unit volume. In addition, the mean value of the total samples is given. It is noticeable that there is an outlier upwards, in the value of the energy absorption of each of the 5 samples, which is written in bold in Table 7.3.

Table 7.3: Theoretical and actual weight of the samples.

Sample type	Sample number	Energy absorption [MJ/m^3]
Constant 80	P1	**309.1**
	P2	116.1
	P3	256.4
	P4	155.2
	P5	150.2
	av.	197.4
Constant 60	P1	560.4
	P2	**951.9**
	P3	745.0
	P4	648.1
	P5	760.7
	av.	733.22
Linear 40-80	P1	2554.7
	P2	2593.8
	P3	**3086.8**
	P4	3037.5
	P5	2879.4
	av.	2830.44
Quadr. 40-80	P1	1103.7
	P2	1734.4
	P3	1838.9
	P4	**2091.3**
	P5	1475.8
	av.	1648.82

The samples with a constant porosity of 80 % show the lowest energy potential capacity, followed by the samples with a porosity of 60 %. The samples with a quadratic and linear curve have the highest energy absorption capacity of the samples listed. When considering the average values, the linear sample has a 40 % higher energy absorption capacity, compared to the quadratic sample. However, it should be noted that the quadratic sample has a higher porosity, see Table 7.1.
The most meaningful comparison is made between the uniform gyroids 'constant 60' and the linear gyroids, since these lie in the same porosity range. When considering the average values, the energy absorption capacity at a strain of 50 % is more than three times lower for the uniform gyroids 'constant 60' than for the linear gyroids.
The different curves of the energy absorption capacity can be found in Figure 7.8, which plots the cumulative energy absorption per unit volume, W, versus strain. Furthermore, the graph is divided into 4 regions. In the respective strain range, each region is dominated by the energy absorption capacity of a different structure.

It can be observed that area I [from 0% to approx. 12%] shows the highest energy absorption of the uniform gyroids 'constant 60', while interval II [from approx. 12% to 20%] shows a dominant linear structure, which is followed by the quadratic structure. In the last interval IV [from 35% to 50%], the linear structure dominates again. The good energy absorption in the lower strain range of the constant structure can be explained by its rapid plateau increase in the stress-strain diagram 7.6. All samples initially have a flat, almost linear region. The linear region of the quadratic and linear samples ends after reaching a compressive load of about 5 %, while the linear

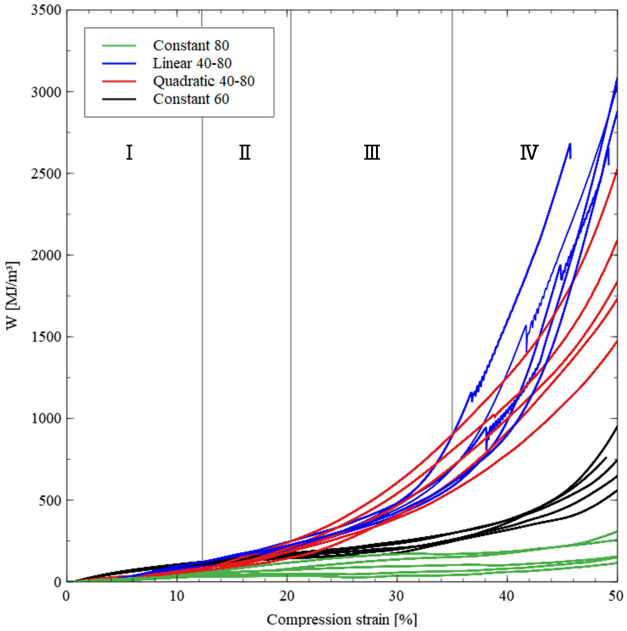

Figure 7.8: Cumulative energy absorption per unit and strain [%]

region of the samples with a constant porosity of 80 % is longer. In the work of Dawei Li [60], it was also found that the linear region of the samples with linear gradients is hardly present. This is due to the more pronounced plateau of the samples with a constant porosity of 80 %, shown in the stress-strain diagram 7.6. When looking at the curves of 'quadratic 40-80' and 'linear 40-80', it can be seen that they are very similar. However, from the beginning of the region IV, the energy absorption of the linear sample increases more rapidly. This can be explained by the fact that the linear sample thickens faster, compared to the quadratic sample, which leads to more stability earlier.

The failure modes of the structures are compared in Figure 7.9. The structures with a constant porosity show a different failure pattern than the structures with gradients.

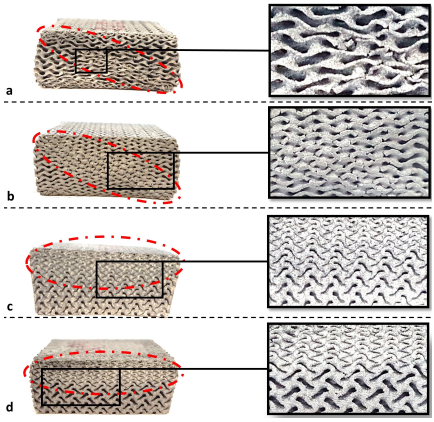

Figure 7.9: Failure modes of gyroid structures - (a) constant 80 % and (b) constant 60 %: diagonal shear failure; (c) linear gradient 40- 80 % and (d) quadratic gradient 40- 80 %: compression in higher porosity area.

For the gyroid structures with a constant porosity of 80 %, diagonal shear is a failure mode, as shown in Figure 7.9. This observation has also been made by Maskery [14] and by Chenxi Lu [61]. They have investigated (sheet-based) gyroid structures made of an aluminum alloy (Al-Si10-Mg), produced by selective laser sintering (SLS).
In the linear (c) and quadratic (d) gyroid structures of Figure 7.9, the layered planes with the higher porosity are compressed like an accordion, while the cells in the lower part of the low porosity samples appear to be unaffected by the forces. This type of failure can be confirmed by the simulation results of the study, which is presented in Chapter 4 [2]. The simulations were performed in the

linear deformation domain, using the simulation software PACE3D. The gyroid structures with linear and quadratic gradients are unit cell structures. It was shown that the stress occurs on the side with the highest porosity, while the structures with a constant porosity show similarly distributed stresses on both sides. In addition, the simulations showed that the 'linear 40-80' and 'quadratic 40-80' gyroid structures have a higher maximum von Mises equivalent stress than the 'constant 60' structures. However, the 'constant 60' structures have a higher normalized von Mises stress than the structures with a gradient. Since the lower part of the structures with gradients was not destroyed (see Figure 7.9 c, d), it can be concluded from the visual observation of the samples and the simulation results that the structure has more unstressed areas in the parts where the porosity is lower. These overlapping results confirm that simulations in the linear deformation domain can show a trend towards a unit cell structure, which allows making a basic statement about the failure of the multicellular structure.

7.1.1.5 Conclusions

In this investigation, gyroid structures with different gradient profiles (constant, linear and quadratic) were considered and their energy absorption capacity was analyzed. For this purpose, the structures were manufactured from an aluminum alloy, using microcast processing, which represents an alternative manufacturing option for complex structures. Compression tests were performed and evaluated to investigate the energy absorption capacity. With regard to the energy absorption capacity, the following could be shown:

I: The gyroid structures with a constant porosity of 80 % and 60 % have a more significant plateau, but the energy absorption capacity is significantly lower than that of the linear and quadratic gradient structures.
II: Overall, the samples with a linear gradient performed best, in terms of energy absorption. These samples were found to have three times the energy absorption capacity, compared to the samples with a constant porosity of 60 %.
III: The samples with a constant porosity of 60 % show the best energy absorption potential in the lower strain range [0% - 12 %].
IV: The samples with a quadratic gradient have good energy absorption in the medium strain range [20% - 35 %].
V: After the compression tests, the individual cells of the constant samples were visibly more damaged than those of the samples with a linear and quadratic gradient.
VI: In the range of linear deformation, simulations of a unit cell structure can show a trend for a fundamental statement about the failure of a multicellular structure.

These results indicate the high potential of structures with gradients and open up the possibility of achieving the desired energy absorption capacity in the future, by optimizing the shape of the gyroid structure. Adaptation to the energy absorption capacity is a central issue in vehicle safety. The gradient structure creates a new lightweight construction and design option with new potential. In addition, the gradient makes it possible to adapt a porous structure to its environment. This is interesting in the field of tissue engineering, when a porous structure needs to be adapted to the bone

structure.

Experimental studies of the behavior of phase-field based shape and structure optimization are discussed in detail in the next chapter.

7.2 Experimental validation of phase-field based shape optimization

In this section, the previously presented phase-field based shape optimization methods of Chapter 5 are experimentally validated. In the first investigation, various TPMS structures were optimized under unidirectional loading, resulting in a loss of periodicity in all spatial directions (see Chapter 5.1). In the second variant, TPMS structures were also optimized, but their periodicity was maintained throughout the optimization process (see Chapter 5.2). Subsequently, the simulation-based and experimental data will be compared.

7.2.1 Experimental evaluation of phase-field based load-specific shape optimization of nature-inspired porous structure

This chapter is based on the publication: [4]

This subsection experimentally validates the initial and phase-field based shape-optimized structures described in Chapter 5.1. For this

purpose, the unit cells are duplicated in the $x-$ and $z-$ directions, as explained in the subsequent sections.

7.2.1.1 Experimental Validation

The experimental validation of the phase-field based shape optimization will be performed according to the ASTM D1621 standard, "Standard Test Method for Compressive Properties of Rigid Cellular Plastics" [43]. The test specimen dimensions, the test procedure, and the subsequent evaluation of the results are adapted to this standard.

Manufacture of Structures The initial and optimized structures were produced using the stereolithography (SL) 3D printer *ELEGOO MARS 2*. The printing material used was the *Standard Photopolymer Resin* (Elegoo Inc) in white color. The single-cell structures were duplicated with a cell size of 30 mm in the $x-$ and $z-$directions. Each specimen has dimensions of 60 mm × 30 mm × 60 mm (in the x, y, and z directions). Five samples were tested for each specimen. Figure 7.10 illustrates a representative candidate of each type of the printed structures.

The theoretically calculated weight for the printed diamond structure with a density of $1.2\,\mathrm{g/cm^3}$, as specified in Table 5.1, is 19.18 g. Accordingly, the weights of the gyroid and primitive structure are 18.92 g and 18.53 g, respectively.
The average values ($\bar{m}$) of the printed samples and their standard deviations ($\widetilde{m}$) are listed in Table 7.4.

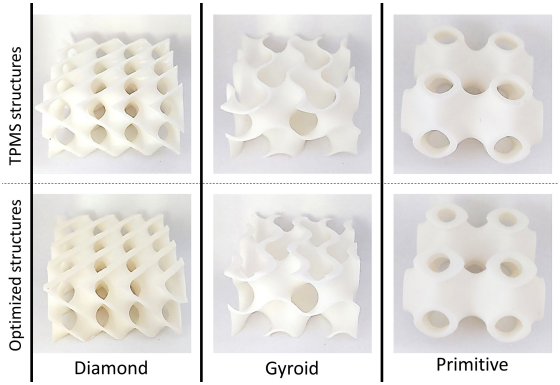

Figure 7.10: Printed Structures: Top the original TPMS-structures; bottom: The optimized TPMS-structures.

Table 7.4: Average weight ($\bar{m}$) and standard deviation ($\widetilde{m}$) of the printed structures.

		Diamond		**Gyroid**		**Primitive**	
		initial	**optimized**	**initial**	**optimized**	**initial**	**optimized**
$\bar{m}$	[g]	19.281	19.018	18.917	18.889	18.572	18.530
$\widetilde{m}$	[g]	0.108	0.420	0.056	0.123	0.085	0.016

Overall, the mean value for each sample deviates from the theoretically calculated sample weight by less than 1 %. As can be seen from the standard deviation, the samples show only minimal variations. It can be observed that the primitive samples show the smallest deviations in both the optimized and non-optimized cases. In contrast, the optimized diamond structure has the highest variation at 0.47 g. One possible reason for these weight fluctuations could be the presence of excess material residues that remained attached to the surface of the samples, despite subsequent acetone treatment. Since the

diamond and gyroid structures have the highest surface-to-volume ratios, as shown in Table 5.1, this could explain why the primitive structure has the least weight variation among the structures.

Mechanical Testing and Evaluation For the experiments, the *inspekt 200* machine from *Hegewald & Peschke* is used. The compression is initiated with a pressure of 0.03 kPa, and the testing speed is set to 2.95 mm/min. The test is terminated as soon as approximately 13 % of the original thickness is reached. For subsequent evaluations, the values are zeroed from a force load of 10 N. The Table 7.11 illustrates at the example of the diamond structure the development of the initial state and the linear-elastic and plastic ranges. At the beginning of the structural collapse, i.e., the failure in the plastic range, the data were truncated for better comparability.

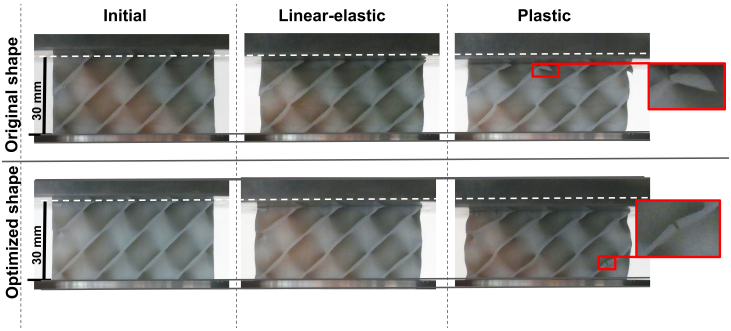

Figure 7.11: The diamond structure (top) and the shape-optimized diamond structure (bottom): Representation of the initial structure, as well as the structure in the linear-elastic and plastic range during the compression test.

The determination of the effective modulus of elasticity is based on the ASTM D1621 standard. The modulus of elasticity was calculated as follows:

$$E = \frac{WH}{AD}, \tag{7.2}$$

with the load W [N], the initial specimen height H [m], the initial horizontal cross-sectional area in A [m^2], and the deformation D [m]. For the determination of D and W, two localized areas of the sample from the linear-elastic range were chosen. However, it should be noted that there are no specific guidelines for the selection of these locations. The local area of each sample at which the strain is at 0.1 % was chosen to determine the value D. To obtain a consistent determination of the quantity W, the respective values at which the strain is 30 % of the difference between the strain at 0.1 % and the strain at the maximum stress were considered. Furthermore, it must be emphasized that for the horizontal cross-sectional area in A [m^2], the area of the samples was treated as if it were a solid material.

7.2.1.2 Results and discussion

The following section compares the simulation-based data with the experimental results, followed by an examination in the plastic regime. Volume conservation during the optimization process ensures that the volume of the initial and optimized structures remains the same, which guarantees a better comparability of the structures. Overall, the experimental validation of the phase-field based shape-optimized TPMS structures demonstrates that the optimization has improved the linear-elastic range and change in the plastic regime.

In Figure 7.12, the load-displacement curves are recorded, and for each cell type ("Type = D": Diamond; "Type = G": Gyroid; "Type = P": Primitive), the respective samples have been averaged. Additionally, their standard deviation is shown in the diagram, where the orange line represents the optimized shape, and the blue line represents the original shape.

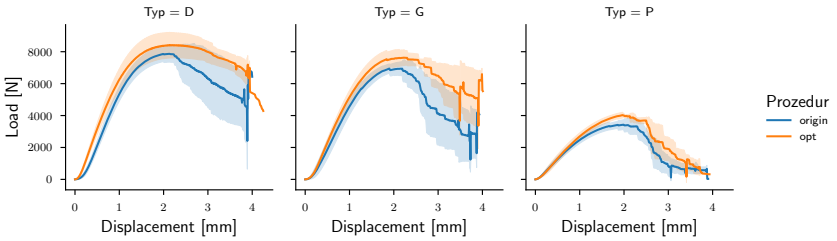

Figure 7.12: Load-Displacement Curve: Average values of compression test for diamond (D), gyroid (G), and primitve (P).

Validation of the phase-field shape optimization model Purely linear-elastic behavior cannot be achieved in porous structures [1, 62–64]. However, Figure 7.12 clearly visualizes the quasi-elastic range. In [64], CuCrMo structures with gyroid, diamond, and primitive topology and different volume fractions (ranging from 0.2 to 0.4) perform elastic behavior at low strain, followed by a sudden collapse. The diamond structures exhibit the highest load-bearing capacity, followed by the gyroid structures, and, finally, the primitive structures [64]. Our shape-optimized structures reveal improvements in the linear-elastic and plastic ranges, compared to the original structures. By design, shape optimization reduces stress concentrations, producing more uniform stress distributions in the component and

reducing material failure.
For the experiments, the average elastic modulus $\bar{E}$ and the standard derivation $\widetilde{E}$ can be found in the top two rows of Table 7.5. These values were determined from the experimental results using equation 7.2, described in Chapter 7.2.1.1.
When considering the standard deviation, the optimized diamond structures have the highest variance, while the optimized primitive structures have the lowest variance.
With 57.377 %, the optimization of the diamond structure achieves the highest increase in the effective modulus of elasticity in the linear elastic range, followed by the gyroid structure with 23.04 %. For the primitive structure, this increase averages 13.37 %. To establish comparability between the simulation-based dimensionless modulus (E_{Sim}) and the experimental data, the dimensionless modulus is converted into a corresponding dimensional modulus E_{SimDim} [MPa], by calculating the effective unit stress for each sample. The density of the material [kg/m^3] and the cross-sectional area [m^2] of each sample are physically predetermined. Consequently, the time [s] represents the adjustable characteristic parameter to be determined based on the experimental data. In the present case, the characteristic time is about 0.915 s, which yields a unit stress of 14.32 MPa. The bottom rows of Table 7.5 compare the dimensionless moduli of elasticity E_{Sim} and the dimensionalized moduli of elasticity E_{SimDim} with the average experimental moduli of elasticity for each topology and optimization state.

Table 7.5: Comparison of the effective modulus of elasticity from the experiments (mean: $\bar{E}$, standard deviation: $\widetilde{E}$) and simulations (dimensionless: E_{Sim}, dimensionalized: E_{SimDim}).

		Diamond		**Gyroid**		**Primitive**	
		initial	**optimized**	**initial**	**optimized**	**initial**	**optimized**
$\bar{E}$	[MPa]	33.369	52.515	27.491	33.826	14.470	16.404
$\widetilde{E}$	[MPa]	4.664	7.142	4.753	4.881	2.531	1.710
E_{Sim}	[-]	2.186	3.403	1.748	2.444	0.989	1.190
E_{SimDim}	[MPa]	31.314	48.748	25.040	35.010	14.164	17.047

For better comparability, the determined values of Young's modulus, belonging to the respective samples from the experimental assessment, are presented in a box plot, and the dimensionalized simulated data are marked in red within the respective box plots Figure **??**.

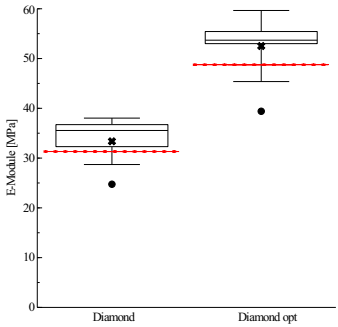

Figure 7.13: Diamond structure: Comparison of the experimental data with the dimensionalized (red dashed line) simulated data. Representation of the experimental data in a box plot: With upper and lower quantile and median, with the standard deviation labeled by the whiskers. The mean value of the experimental data is indicated by a cross and the outliers by circles.

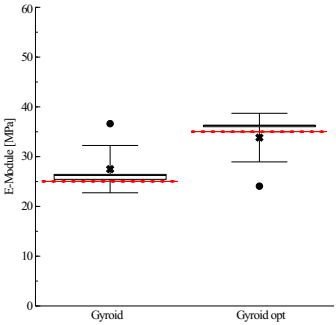

Figure 7.14: Gyroid structure: Comparison of the experimental data with the dimensionalized (red dashed line) simulated data. Representation of the experimental data in a box plot: With upper and lower quantile and median, with the standard deviation labeled by the whiskers. The mean value of the experimental data is indicated by a cross and the outliers by circles.

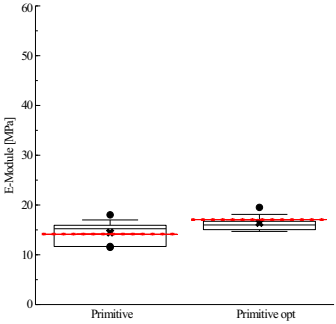

Figure 7.15: Primitive structure: Comparison of the experimental data with the dimensionalized (red dashed line) simulated data. Representation of the experimental data in a box plot: With upper and lower quantile and median, with the standard deviation labeled by the whiskers. The mean value of the experimental data is indicated by a cross and the outliers by circles.

The arithmetic mean of the experimental data is indicated by a black bold cross, while the outliers of the samples are marked by a black circle. It is evident that there is at least one outlier in the experimental data. The whiskers represent the standard deviation from the mean value. The dimensionalized simulated data are represented by a red dashed line in each box plot. The box plots show that the simulated values lie within the standard deviation of the experimental values. In some cases, this value is also within the quartiles and close to the mean value (black cross) of the experimental data. The dimensionalized Young modulus of the optimized diamond structure is farthest from the mean value of the experimental data, while that of the primitive structure is almost the same. The box plots show that scaling establishes a clear correlation between the simulation and the experimental data.

The ability to convert dimensionless data into dimensional data is crucial for future research. It is also important to emphasize that the conversion can be applied even if the simulation data relate to different material properties and cell dimensions (see [3]). This underlines that a load-specific shape optimization of complex cell structures is possible by using dimensionless data with the phase-field method. In the field of linear elasticity, shape optimization leads to a structure that is independent of material properties and dimensions. This can also be confirmed if a different base material is used for dimensionalization. For example, this investigation considered polylactide (PLA) under equal load conditions.

Table 7.6 lists the simulated effective modulus of PLA which can also be scaled to the experimental modulus by a constant material-specific factor. Furthermore, a comparison of the two dimensionless parameters (modulus calculated from the aluminum alloy and

modulus based on PLA) is also possible. These parameters can be converted into each other with a factor of 0.1. This suggests that the simulation is in this case independent of the material. This observation is consistent with previous results of 2D studies.

Table 7.6: Comparison of the originally simulated effective modulus of elasticity (E_{Sim}) and the experimentally determined modulus of elasticity ($\bar{E}$) with modified simulative material properties (E_{Sim_PLA}).

		Diamond		**Gyroid**		**Primitive**	
		initial	**optimized**	**initial**	**optimized**	**initial**	**optimized**
E_{Sim_PLA}	[MPa]	0.315	0.521	0.255	0.380	0.147	0.188
E_{Sim_PLA}/E_{Sim}	[-]	0.01	0.01	0.01	0.01	0.01	0.01
$\bar{E}/E_{Sim\_PLA}$	[-]	105.93	100.797	107.808	89.016	98.435	87.255

Overall, it is demonstrated that shape optimization in the linear-elastic range is accompanied by an increase in the effective modulus of elasticity (Young's modulus) and, consequently, an increase in stiffness. This result has been presented with convincing agreement in both simulations and experiments.

Influence on Plastic Deformation Apart from the linear-elastic range, the plastic range is considered. In addition to the increase in the effective elastic modulus of elasticity, a change in the plastic deformation range can be observed. This aspect becomes apparent from the analysis of the load-displacement curves (Figure 7.12) and the average maximum stress values ($\mu_{stress}[MPa]$) in Table 7.7. An increase in the effective modulus of elasticity consequently leads to a shift in the plastic deformation range.

Table 7.7: Average maximum stress ($\bar{\sigma}_{\max}$) and standard deviation ($\tilde{\sigma}_{\max}$) of TPMS structures in MPa.

		Diamond		**Gyroid**		**Primitive**	
		initial	**optimized**	**initial**	**optimized**	**initial**	**optimized**
$\bar{\sigma}_{\max}$	[MPa]	12.732	13.488	11.38	12.326	5.636	6.558
$\tilde{\sigma}_{\max}$	[MPa]	0.779	1.264	0.492	0.846	0.412	0.226

It can be observed that the optimization of the primitive structure in the linear-elastic range has the greatest effect on the maximum stress by about 16.40 %, despite the smallest increase in the effective modulus of elasticity by 13.37 %. While the increase in the effective modulus of elasticity has a direct effect on the overall stiffness of the structures, changes in the maximum stress can be attributed to the volume redistribution during the shape optimization process. Similar to the standard deviation of the effective Young modulus from Table 7.5, the standard deviation of the maximum stress has the highest value for the diamond structure, while the standard deviation of the optimized primitive structure shows the lowest variation between the samples.

Furthermore, the individual shape-optimized structures exhibit fewer sudden failure patterns than the non-optimized structures. In conjunction with the shift in the plastic deformation range, this results in a higher energy absorption capacity of the optimized structure, making it more suitable for additional applications such as crash structures. The improved mechanical performance of the optimized

structures makes them particularly promising for deployment in various engineering applications where energy absorption and resistance to plastic deformation are crucial factors.

7.2.1.3 Conclusion

This work has focused on the experimental validation of load-specific shape-optimized TPMS unit cells. In previous work, TPMS unit cells were shape-optimized under unilateral compression, using a novel phase-field method integrated with shape optimization scheme. The present experimental validation reveals a correlation between the simulation and experimental data. To achieve this, the original and optimized individual TPMS unit cell structures were replicated in the x- and z-directions and manufactured using SLA 3D printing. Compression tests showed that the simulation results match well with the order of magnitude of the experimental data. As a result, shape optimization leads to an increase in the effective modulus of elasticity, on average, compared to the original structure. For better comparability, the dimensionless data were scaled between simulation-based dimensionless data and experimental data. This scaling results in a correspondence between the simulated scaled effective modulus and the calculated modulus, with a maximum deviation of 6 %. Furthermore, it is discussed that optimization in the linear elastic regime shifts the plastic range. Despite the smallest increase in the effective modulus of elasticity observed when optimizing the primitive structure, this type of structure exhibits the highest percentage increase in maximum stress. In addition, the load-displacement curves illustrate that the shape-optimized structures

collapse less abruptly, which leads to a longer plateau in the plastic range and thus to a greater energy absorption capacity. In summary, the matching comparison presented between experimental and simulated data confirms evidence that the computational shape optimization based in a phase-field approach is a valuable and reliable tool to optimize the morphology of porous structures under mechanical loading. This provides a resource-efficient method for virtual materials design with a versatile and extensive application potential. Despite the use of dimensionless data for the simulation with different material parameters and structure sizes, the subsequent scaling reveals a correlation between the experimental and simulation-based data. Using dimensionless data in a single phase material simulation resulting in material- and dimension-independent load-specific shape optimization, while maintaining the volume, is achievable. These results underline the potential of the phase-field method as a promising tool for load-specific optimization of complex porous structures. The optimization of multicellular structures or under different load conditions is also possible. This novel design approach is important in various fields, such as bone scaffold design, where shape optimization maintains a high surface-to-volume ratio and a curved surface that is favorable for bone growth, while introducing load-specific gradients that improve mechanical properties. Furthermore, these structures are promising in crash applications, as the shape optimization extends the plastic plateau and enables higher energy absorption.

The following chapter 7.2.2 presents the experimental validation of the gyroid structures optimized in Chapter 5.2 under unidirectional loading. It has been ensured that the periodicity in all spatial

directions is maintained throughout the optimization process of the structures.

7.2.2 Experimental validation of shape-optimized gyroid structures while maintaining periodicity

This chapter is based on the publication: [5]

The following section will experimentally validate the unidirectionally shape-optimized structures under unidirectional loading.
The main objective of the experimental validation is to confirm, that the computed candidates are indeed structurally optimized for the imposed mechanical loading treatments.
For the experimental validation, the unidirectionally shape-optimized gyroid structures of Chapter 5.2 are used. Therefore, the initial structures and the unidirectionally loaded, shape-optimized gyroid structures are manufactured using additive manufacturing and subsequently tested by applying mechanical loads.

7.2.2.1 Structure manufacturing

The original and optimized unit cells are replicated four times in each of the three dimensions (x, y, and z- direction) for experimental validation, resulting in a total size of $4x4x4$ cells. The specimen size of about 50.8 mm in each spatial direction meets the minimum requirements of the standard presented in Subsection 7.2.2.2.
The test specimens are manufactured using Standard Photopolymer

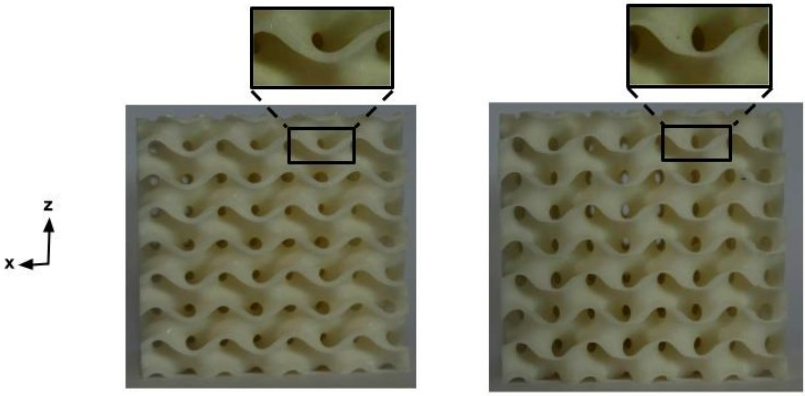

(a) Ini. structure: $V^* = 0.25\,[-]$

(b) Opt. structure: $V^* = 0.25\,[-]$

Figure 7.16: xz-plane of the initial (a) and optimized (b) printed sheet-based gyroid structure with a volume fraction of $V^* = 0.25\,[-]$.

Resin (Elegoo Inc) in white color on the Stereolithography (SL) 3D printer ELEGOO MARS 2. For slicing the structures, the software Chitubox Version 1.9.5 was used. Each test specimen is printed five times and subsequently tested. Figure 7.16 illustrates the initial and optimized gyroid structure with a volume fraction of $0.15\,[-]$, serving as an exemplary case for the other test specimens.

The xz-plane of the printed test specimens is shown to illustrate the geometric changes resulting from the shape optimization process. Upon examining the xz-plane with the highlighted region, it becomes evident that the original structure exhibits regular wave-like struts with consistent thickness in the x-direction, whereas the strut thickness in the x-direction is reduced after the shape optimization process, as depicted in Figure 5.9. This geometric alteration is observed in all three structures. The reason for this lies in the fact

that the transverse struts in the x-direction are minimally stressed at these points due to the specified deformation, resulting in a reduction in volume.
Furthermore, it is noteworthy that manufacturing the optimized structures posed a challenge at times, as the walls of the shape-optimized gyroid structures became very thin and fragile in certain areas due to the optimization process. Therefore, a loss of accuracy in replicating the digital structures by 3D printing is introduced.

7.2.2.2 Mechanical Testing Condition

The experimental validation of the unidirectional shape-optimized gyroidal unit cells based on the phase-field method is conducted according to the ASTM D1621 standard, "Standard Test Method for Compressive Properties of Rigid Cellular Plastics" [43]. Accordingly, the sizing of the samples, as well as the testing conditions and evaluations, are based on the standard. For conducting the compression tests, the *inspekt 200* machine from *Hegewald & Peschke* is utilized. The testing is initiated with compression at a pressure of 0.03 kPa and is conducted at a testing speed of 2.95 mm/min. The test is terminated upon reaching approximately 13 % of the original thickness. For subsequent evaluations, the values are zeroed from a force load of 10 N.

7.2.2.3 Results and discussion

In comparison to homogeneous materials, local stress peaks are more pronounced in porous structures, leading to a relatively small range

of linear elastic behavior due to local plastification being established at relatively small macroscopic strains. This can also be seen from the stress-strain diagram in Figure 7.17 of the three considered structure types. In the stress-strain diagram, the average measurement curves with their respective standard deviations are depicted. The dashed blue lines refer to the initial structures (I), while the solid green lines represent the shape-optimized (O) structures.

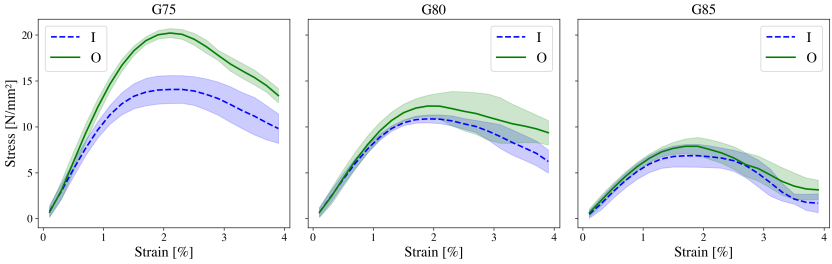

n

Figure 7.17: Stress-strain curve of averaged experimental data including standard deviation for the initial and optimized gyroid structures with porosities of 75 % (G75), 80 % (G80), and 85 % (G85).

From the stress-strain diagram, it is evident that the average measurement curve of the optimized structures lies above the course of the initial sample types. This clearly shows that the shape optimization results in increased stiffness within the linear elastic regime. Furthermore, also in the plastic range, improvements are observed compared to the original structures. Therefore, improvements from the elastic optimization can also be transferred to plastic properties. The gyroid structure with a volume fraction of 0.25 [−] (G75) records the highest load capacity, followed by the structure with a porosity of volume fraction of 0.20 [−] (G80) and 0.15 [−] (G85). The greatest

optimization success is clearly achieved with the G75 structure. This is because the largest volume redistribution occurred in the structure with a porosity of 75 %. From the respective force-displacement diagrams, the Young's moduli for each individual sample are determined using the formula suggested in the ASTM D1621 standard. The modulus of elasticity (E) is calculated as

$$E = \frac{WH}{AD}, \tag{7.3}$$

where W [N] is the load, H [m] the height of the undeformed sample, A [m^2], the horizontal cross-sectional area, and D [m] denotes the deformation. For the determination of D and W, two localized areas of the sample from the linear-elastic range are selected. Since the guideline does not provide specific details about the choice of points, the local area of each sample where the strain is 0.1 % is selected. To ensure a consistent determination of the W size, the respective values at which the strain is 30 % of the difference between the strain at 0.1 % and the strain at maximum stress are considered. As these are porous specimens, the horizontal cross-sectional area in A [m^2], the area of the samples is treated as if it was a solid material. In Table 7.8 the average calculated effective Young's modulus from the experimental data $\bar{E}$, as well as their standard deviation $\widetilde{E}$, are listed. For a better overview and comparison between the experimental and simulation data, the dimensionless Young's moduli from Table 5.2 are dimensionalized and also listed ($\bar{E}_{\mathrm{Sim}}$).

When examining the average Young's modulus, it is clear that the optimized structures all exhibit a higher Young's modulus compared to their original structures. The highest variations in the calculated

Table 7.8: Comparison of the effective modulus of elasticity from the experiments (mean: $\bar{E}$, standard deviation: $\widetilde{E}$) and simulations (dimensionalized: $\bar{E}_{\mathrm{Sim}}$).

Sample	**75% initial**	**75% optimized**	**80% initial**	**80% optimized**	**85% initial**	**85% optimized**
$\bar{E}$ [MPa]	70.726	99.511	59.107	64.026	42.327	46.200
$\widetilde{E}$ [MPa]	11.426	2.750	3.133	6.589	3.980	2.533
$\bar{E}_{\mathrm{Sim}}$ [MPa]	69.395	101.974	50.672	70.995	39.773	53.427

Young's modulus are seen in the initial structures of 75 %, while its optimized counterpart with a deviation of 2.750 MPa shows a minor deviation. On average, the effective Young's modulus could be increased by about 40 %. For the gyroid structure with a porosity of 80 %, the optimization process achieved an increase of 9.8 % and the structure with the highest porosity of 85 % achieved the smallest increase in the effective Young's modulus with an increase of 2.4 %. For further comparison, the values are illustrated in box plots in Figures 7.18-7.20. The red, thick bar symbolizes the dimensionalized Young's modulus. The cross marks the mean, and the round dots denote the outliers of the respective sample series. Additionally, the whiskers indicate the standard deviation. When comparing the box plots between samples with different porosities, attention should be paid to the scaling of the y-axis.

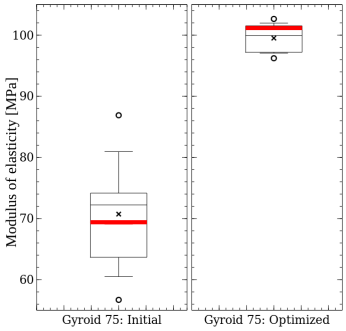

Figure 7.18: Comparison of simulated and experimentally determined elastic moduli from compression tests of the gyroid structure with a volume fraction of 0.25 [−]. The solid red bar represents the dimensionalized Young's modulus obtained from simulation, while the cross denotes the mean of the experimentally obtained data. Whiskers indicate the standard deviation, and outliers are marked by points.

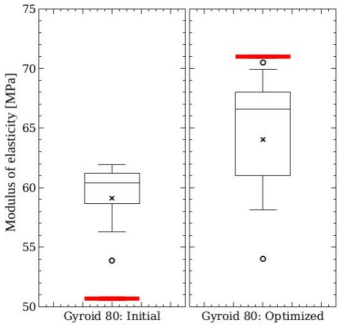

Figure 7.19: Comparison of simulated and experimentally determined elastic moduli from compression tests of the gyroid structure with a volume fraction of $0.20\,[-]$. The solid red bar represents the dimensionalized Young's modulus obtained from simulation, while the cross denotes the mean of the experimentally obtained data. Whiskers indicate the standard deviation, and outliers are marked by points.

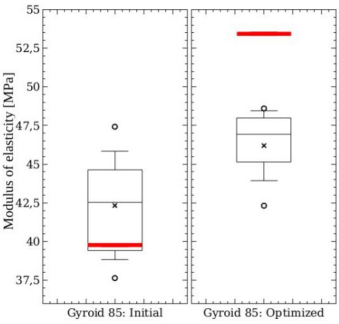

Figure 7.20: Comparison of simulated and experimentally determined elastic moduli from compression tests of the gyroid structure with a volume fraction of $0.15\,[-]$. The solid red bar represents the dimensionalized Young's modulus obtained from simulation, while the cross denotes the mean of the experimentally obtained data. Whiskers indicate the standard deviation, and outliers are marked by points.

When examining the box plots, it is noticeable that the experimental and simulation data of the gyroid structure with volume fraction of 0.25 [−] match the best, while the simulation data for the gyroid structures with volume fractions of 0.2 [−] and 0.15 [−] do not always fall within the experimentally determined data ranges. The highest deviation is observed in the samples with a volume fraction of 0.2 [−] and optimized structures with a volume fraction of 0.15 [−], with an average deviation of approximately 15 %. The samples with higher volume fraction (G75) show the smallest deviation from the simulation results, possibly due to challenging manufacturing quality caused by thin walls and small cell size. Nonetheless, the experimental validation confirmed that a load-specific optimization using the phase-field method while maintaining the periodicity of complex porous structures is successfully feasible. This confirmation not only opens up the possibility to optimize gyroid structures but also other complex structures. Thanks to the successful maintenance of periodicity in all spatial directions during the optimization process, there is the option to optimize unit cells and then multiply them accordingly in the respective directions. This opens up a multitude of design possibilities for various industrial applications where stability and low weight are important.

7.2.2.4 Conclusion

After demonstrating the feasibility of load-specific phase-field based shape optimization simulations in Chapter 5.2, the unidirectionally loaded shape-optimized structures are experimentally validated. Experimental validation followed the ASTM D1621 standard. The

evaluation of the test specimens shows that, on average, the shape-optimized structures exhibit higher stiffness in the respective loading directions. The optimization of the structures influence both the linear elastic and plastic range. As evident from the simulations, the optimized gyroid structure with a porosity of 75 % achieves an average increase in the effective modulus of elasticity of 40 %.
Overall, the load-specific shape optimization based on the phase-field approach offers promising prospects for various applications across different industries. By preserving key structural characteristics such as periodicity throughout the optimization process, complex structures can be tailored to specific loading scenarios. This capability holds immense potential for developing efficient and customized solutions in fields such as medical engineering.

The final subsection of the experimental validation is the experimental investigation of the phase-field based, structure-modified gyroid structures presented in Chapter 7.3.1.

7.3 Experimental validation of phase-field based structural optimization

Previous investigations have shown that numerical simulations of shape-optimized structures accurately reflect experimental results. To examine the transfer ability of this correlation to more complex optimization strategies, topology-optimized structures will be considered in the following. The aim is to determine whether the simulations can also reliably predict the experimental results in this case.

7.3.1 Experimental validation of phase-field-based load-specific structural optimization of sheet-based gyroid-structures

This chapter is based on a manuscript that is currently under review.

In the following, topology optimized gyroid structures with a final porosity of 80 % are compared to an unmodified gyroid reference structure. The structure modification was performed using the phase-field method with the aim of maximizing stiffness in a specific loading direction. The results of the numerical simulations, including the generated structures and their mechanical characterization, are summarized in subchapter 6.1.
For the experimental validation of the topologically modified unit cells described above, they are multiplied four times in the respective spatial directions and printed out. The unmodified gyroid structure with a porosity of 80 % is used as the reference structure. As a result, all three structures have a volume fraction of approximate 20 %.
The production of the samples and their subsequent testing are based on the ASTM D1621 standard "Standard Test Method for Compressive Properties Of Rigid Cellular Plastics" [43].

7.3.1.1 Structure manufacturing

The previously considered unit cells are multiplied 4 times in each spatial direction for the experimental validation, so that the test specimens have a required minimum side length of 25.4 mm.

For each sample type, 5 samples are printed using the steriolithography (SL) process. The SL printer from Elegoo Mars 2 and the white standard photopolymer from Elegoo are used for this purpose.
In Figure 7.21, one sample type is shown as a representative of the other samples.

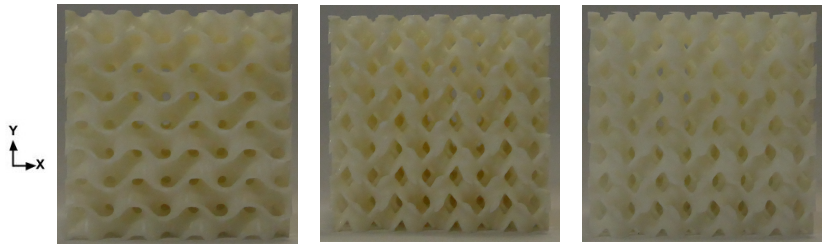

(a) Gyroid80 **(b)** $Gyroid75_{Nuc}$ **(c)** $Gyroid80_{NucShape}$

Figure 7.21: Planar representation of a) the unmodified gyroid structure of porosity 80 %, the modified structures with the initial porosity of b) 75 % and c) 80 %.

Similar to the topology-modified unit cells shown, the difference between the multiplied and printed $Gyroid75_{Nuc}$ and $Gyroid80_{NucShape}$ is barely recognizable. The planar $xy-$direction shows the previously described reduction of the crossbars due to the modification process.
The weight of the respective test specimens, their average weight and the theoretically calculated weight $\bar{g}$ with the volume fractions determined from Table 6.1 are listed in Table 7.9.

The table shows that the test specimens exhibit slight weight fluctuations. When comparing the average values (Av) with the theoretically calculated weight values ($\bar{g}$), it becomes clear that they are in a similar range.

	S1	S2	S3	S4	S5	Av	$\bar{g}$
Gyroid80	31.312	31.616	32.019	31.771	30.836	31.5108	31.09
$Gyroid75_{Nuc}$	33.201	33.299	32.515	33.384	33.074	33.0946	33.52
$Gyroid80_{NucShape}$	30.869	31.847	31.915	31.807	31.994	31.6864	31.90

Table 7.9: Weight of the printed samples, their average value (Av) and the theoretically calculated weight value $\bar{g}$.

7.3.1.2 Mechanical Testing Condition

The *Inspekt 200* machine from *Hegewald & Peschke* is used to carry out the compression tests for the experimental validation of the unidirectional topology-modified gyroid structures and their reference structure. The initial pressure load starts at 0.03 kPa and is applied at a test rate of 2.95 mm/min. When about 13 % of the original thickness is reached, which corresponds to a distance of about 6.60 mm, the test is terminated. For standardized data evaluation, the values are zeroed from a force load of 10 N.
The calculation of the effective modulus of elasticity (E) from the experimental data is also based on the ASTM D1621 standard, which is calculated as follows:

$$E = \frac{WH}{AD}, \tag{7.4}$$

where W[N] is the load, H[m] is the height of the undeformed sample, and D[m] is the deformation. A[m^2] denotes the horizontal cross-sectional area. Since the samples are porous, the horizontal cross-sectional area in A[m^2], i.e. the area of the samples, is treated as if it were a solid material. The points D and W indicate two

points from the linear-elastic range. Since the guideline does not provide specific details on the selection of the points, the local area of each sample is selected where the strain is 0.1 %. To determine the value W, the point at 30 % of the maximum stress is selected. In the following section, the effective modulus of elasticity of the structures will first be determined experimentally from equation 7.4 and then compared with the simulation data obtained in Chapter 6.1.

7.3.1.3 Results and discussion

First, the elastic moduli will be determined based on the experimentally obtained load-displacement curves, and then compared with the data derived from simulations.

Experimental result The load-displacement curves of the five different samples per specimen type resulting from the compression tests are shown side by side in Figure 7.22.

Each sample type is represented by one line type:
$Gyroid80NucShape$ (black solid line), $Gyroid75Nuc$ (blue dashed line) and $Gyroid80NucShape$ (green dotted line) structure. For better comparability, the curves of the individual samples are overlaid. It can be seen from the diagrams that the comparative structure (black solid line) shows the smallest increase in the linear elastic range compared to the optimized structures, which is reflected accordingly in the effective modulus of elasticity. It is also recognizable that the maximum load is also lower on average. However, the curve after the load peak is flat and more controlled. Table 7.10 presents

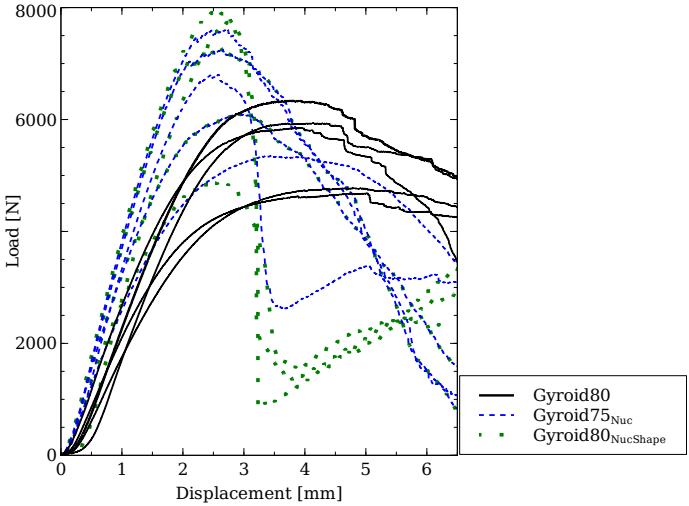

Figure 7.22: Load-displacement curves for the five tested samples of the unmodified gyroid structure with a porosity of 80 % (black solid line) compared to the modified structures with the initial porosity of 75 % (blue dashed line) and 80 % (green dotted line).

the mean value of the effective E-moduli ($\bar{E}$) of the tested samples calculated according to Equation 7.4 and standard deviation (σ).

	$Gyroid80$ [MPa]	$Gyroid75_{Nuc}$ [MPa]	$Gyroid80_{NucShape}$ [MPa]
$\bar{E}$	47.950	67.695	66.809
σ	6.929	9.673	12.937

Table 7.10: Calculated mean value of the effective moduli of elasticity ($\bar{E}$) and standard deviation (σ) of the specimens.

The increase in the load-displacement curves of the modified structures (Figure 7.22), compared to the unmodified gyroid structure,

already indicates a higher average modulus of elasticity ($\bar{E}$). This is further confirmed by the calculation of the effective modulus of elasticity in Table 7.10, where the average modulus for the modified gyroid structures is approximately 20 MPa higher than that of the unmodified structure. Additionally, the two modified structures exhibit similar modulus values, but the table also reveals that the modified structures have higher standard deviation. The reasons for the increased standard deviation of the samples must be further validated in future investigations.
The following chapter compares the experimental and simulative data.

Experimental and simulative comparison The previous simulative (E_{yy} in Tab 6.2) and experimental ($\bar{E}$ in Tab 7.10) investigations of the effective modulus of elasticity show that a phase-field-based topology change and optimization in the linear-elastic range leads to an increase in the effective modulus of elasticity. Consequently, the moduli of elasticity for the structures $Gyroid75_{Nuc}$ and $Gyroid80_{NucShape}$ are, on average, higher than that of the reference structure *Gyroid80*. Furthermore, the experimental results also confirmed the previous simulation observation that the effective modulus of elasticity of the structure $Gyroid75_{Nuc}$ is, on average, slightly higher compared to $Gyroid80_{NucShape}$.
To facilitate a better comparison between the experimentally and numerically determined effective moduli of elasticity, the data for each sample type are presented in a box plot Figure 7.23. In the box plot, the cross marks the mean value, and the round dots indicate the outliers of the respective sample series. Additionally, the

whiskers represent the standard deviation. The red bar indicates the dimensionally simulated modulus of elasticity.

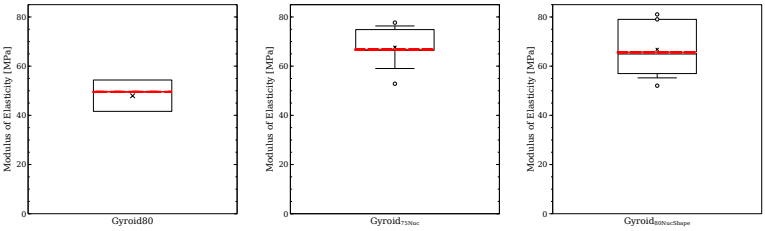

(a) Gyroid80 **(b)** $Gyroid75_{Nuc}$ **(c)** $Gyroid80_{NucShape}$

Figure 7.23: Comparison of the simulatively (red bar) and experimentally (box plot) determined effective moduli of elasticity of a) unmodified gyroid structure with a porosity of 80 %, the modified structures with the initial porosity of b)75 % and c) 80 %.

Accordingly, the dimensionalized moduli of elasticity from the simulation (red bar) and the experimental data are in a similar range. However, it should be noted that the lowest scatter is observed in the comparative structure, as can also be seen from the standard deviation (σ) in Table 7.10. Consequently, no outliers are present in the box plot in Figure 7.23a. Additionally, the determined data range for *Gyroid80* aligns with the simulated effective modulus of elasticity calculated by another study [5] for the gyroid structure with a porosity of 80 %.
Overall, it is demonstrated that optimization in the linear elastic range results in noticeable changes in both, the linear elastic and plastic ranges. A pure topology change leads to an increase in the modulus of elasticity, which has been confirmed both numerically and experimentally.

7.3.1.4 Conclusion

In this study, two gyroid structures with a final porosity of 80 %, which were topology-modified based on the phase-field method, were investigated simulatively and experimentally. An unmodified gyroid structure with a porosity of 80 % also served as a comparative structure.
In the first method, a gyroid structure with an initial porosity of 75 % was reduced by approx. 5 % through targeted volume reduction. In the second method, the gyroid structure has an initial porosity of 80 %, after a volume reduction of also approx. 5 %, a phase-field based shape optimization was then carried out until the initial porosity of 80 % was reached.
It could be shown both simulatively and experimentally that the structural modification in both variants leads to an increase in the effective modulus by 32 %.
The experimental validation also showed that the optimization in the linear elastic range also led on average to an increase in the maximum load, and it was also observed that the structures exhibited a change in the curve in the plastic range. Overall, it was shown that the phase-field method is a promising optimization method for complex three-dimensional structures. The study highlights the significant impact of topology modification and optimization on the mechanical properties of gyroid structures. The observed increase in the modulus of elasticity due to phase-field based modifications underscores the potential of this approach for developing advanced materials with tailored properties.

8 Conclusion

In this work, cellular structures, particularly TPMS structures, were optimized under mechanical loading to improve their stiffness and specific properties. Three different optimization approaches were investigated for this purpose.

First, the manual optimization process was examined. Various porosity gradients were introduced, allowing the porosity to be selectively varied across the structure. This resulted in structures with different porosity distributions. The experimental results showed that structures with quadratic and linear gradients have higher energy absorption capacity compared to structures with constant gradients. Additionally, a correlation between the experimentally determined and simulation-based results was established. These findings demonstrate that a targeted adjustment of porosity can already lead to improvements in mechanical properties.

In the following chapter, a novel approach for load-specific optimization was introduced. The phase-field method provides a way to precisely optimize structures through interface displacement. The TPMS structures were shape-optimized using a modified phase-field method (PFM) under volume conservation, specifically for different loading conditions. Various load-specific boundary conditions

were considered in the simulations to ensure optimal adaptation of the structures to the respective load cases. The initial and shape-optimized structures were experimentally validated. Here, again, a correlation between the experimentally determined and simulation-based data was established, confirming the validity and reliability of the phase-field based optimization. The experimental validations showed that the phase-field based optimizations led to an improvement in mechanical properties.

In the third optimization method, structural optimization, two different cell structures – the gyroid structure and a lattice structure – were optimized under load. The process began with a topological modification of the structures under specific loading conditions. Material was removed from less stressed areas, while the periodicity of the structures was maintained. This approach led to a novel, load-oriented structure with reduced volume. Subsequently, the topologically modified structures underwent shape optimization.
The investigations in both cases showed that the topological modification resulted in a specific load-adapted structure, while the shape optimization allowed for further adjustments to improve load distribution. This approach ultimately led to the development of new periodic lightweight structures. Furthermore, the structurally optimized and modified gyroid unit cells were experimentally validated. Similar to the previously conducted phase-field based shape optimization, the experimental results confirmed that a correlation between the experimentally and numerically obtained data could be established. Among other things, it was shown that the optimization led to an increase in the effective modulus in the respective optimization direction.

Overall, the diverse possibilities of phase-field based structural optimization were comprehensively examined and demonstrated. It was shown that the phase-field based optimization approach is a promising method both for shape optimization and for the creation of new structures. The experimental validations confirmed the improvement of the properties.
The corresponding perspectives and further research approaches are detailed in the following chapter.

9 Outlook

The phase-field based, load-specific structural optimization offers a valid and versatile method in both industry and research, applicable to the creation of new structures as well as the optimization of existing ones. This method enables the adaptation and application of structures in various fields, such as crash structures and bone support structures.

In this work, different loading scenarios, both in single and multi-dimensional loading cases, were investigated and analyzed. These scenarios were experimentally validated, considering various stress boundary conditions. Despite these comprehensive studies and successful validations, there are still numerous opportunities for further development of the method.

One such opportunity is to extend the load-specific phase-field method to develop new structures while considering manufacturing constraints, particularly for additive manufacturing. This could, for example, involve designing structures in such a way that support structures are not necessary. Such an adaptation would make the phase-field method even more attractive for industrial applications.

Another potential lies in adapting the phase-field method to multi-phase systems. So far, two-phase systems have been mainly considered. By extending to multi-phase systems, additional optimizations, such as in material distribution or the combination of different materials, could be explored.

An equally important point of research and development would be the optimization of simulation speed. Faster simulations would not only increase the efficiency of the optimization processes, but also further promote the application of the phase-field method in industry. More efficient algorithms and advanced computational methods could lead to significant improvements in this area.

Overall, it is evident that the phase-field based structural optimization already offers great potential for future developments and applications in various technical and industrial fields. The further development of the method, especially regarding manufacturing constraints, multi-phase systems, and simulation speed, could lead to further breakthroughs and increase the method's attractiveness.

List of Figures

List of Tables

Bibliography

[1] L. Wallat, M. Selzer, U. Wasmuth, F. Poehler, and B. Nestler, "Energy absorption capability of graded and non-graded sheet-based gyroid structures fabricated by microcast processing," *Journal of Materials Research and Technology*, vol. 21, pp. 1798–1810, 2022. [Online]. Available: https://www.sciencedirect.com/science/article/pii/S2238785422015009

[2] L. Wallat, P. Altschuh, M. Reder, B. Nestler, and F. Poehler, "Computational design and characterisation of gyroid structures with different gradient functions for porosity adjustment," *Materials*, vol. 15, no. 10, 2022. [Online]. Available: https://www.mdpi.com/1996-1944/15/10/3730

[3] L. Wallat, M. Reder, M. Selzer, F. Poehler, and B. Nestler, "Shape optimization of porous structures by phase-field modeling with strain energy density reduction," *Materials Today Communications*, vol. 37, p. 107018, 2023. [Online]. Available: https://www.sciencedirect.com/science/article/pii/S2352492823017099

[4] L. Wallat, A. Koeppe, M. Selzer, M. Seiler, F. Poehler, and B. Nestler, "Experimental evaluation of phase-field-based load-specific shape optimization of nature-inspired porous

structures," *Materials Today Communications*, vol. 38, p. 108088, 2024. [Online]. Available: https://www.sciencedirect.com/science/article/pii/S2352492824000680

[5] L. Wallat, N. Kersch, M. Reder, M. Selzer, M. Seiler, F. Poehler, and B. Nestler, "Phase-field based shape optimization of uni- and multiaxially loaded nature-inspired porous structures while maintaining characteristic properties." *Discover Mechanical Engineering*, 2024.

[6] L. Wallat, M. Selzer, M. Seiler, F. Poehler, and B. Nestler, "Phase-field based load-specific structural optimization of sheet-based gyroid-structures."

[7] L. Wallat, M. Reder, M. Selzer, M. Seiler, F. Poehler, and B. Nestler, "Phase-field based structural optimization of 3d cross-lattice structure to lightweight periodic lattice structures."

[8] T. A. Schaedler and W. B. Carter, "Architected cellular materials," *Annual Review of Materials Research*, vol. 46, no. 1, pp. 187–210, 2016. [Online]. Available: https://doi.org/10.1146/annurev-matsci-070115-031624

[9] M. Bodaghi, A. Serjouei, A. Zolfagharian, M. Fotouhi, H. Rahman, and D. Durand, "Reversible energy absorbing meta-sandwiches by fdm 4d printing," *International Journal of Mechanical Sciences*, vol. 173, p. 105451, 2020. [Online]. Available: https://www.sciencedirect.com/science/article/pii/S0020740319336392

[10] K. Michielsen and D. Stavenga, "Gyroid cuticular structures in butterfly wing scales: biological photonic crystals," *Journal of the Royal Society Interface*, vol. 5, no. 18, pp. 85–94, Jan. 2008.

[11] M. Lai, A. N. Kulak, D. Law, Z. Zhang, F. C. Meldrum, and D. J. Riley, "Profiting from nature: macroporous copper with superior mechanical properties," *Chem. Commun.*, pp. 3547–3549, 2007. [Online]. Available: http://dx.doi.org/10.1039/B707469G

[12] N. Kladovasilakis, K. Tsongas, and D. Tzetzis, "Mechanical and fea-assisted characterization of fused filament fabricated triply periodic minimal surface structures," *Journal of Composites Science*, vol. 5, p. 58, 02 2021.

[13] D. Downing, A. Jones, M. Brandt, and M. Leary, "Increased efficiency gyroid structures by tailored material distribution," *Materials & Design*, vol. 197, p. 109096, 2021. [Online]. Available: https://www.sciencedirect.com/science/article/pii/S0264127520306316

[14] I. Maskery, L. Sturm, A. Aremu, A. Panesar, C. Williams, C. Tuck, R. Wildman, I. Ashcroft, and R. Hague, "Insights into the mechanical properties of several triply periodic minimal surface lattice structures made by polymer additive manufacturing," *Polymer*, vol. 152, pp. 62–71, 2018, sI: Advanced Polymers for 3DPrinting/Additive Manufacturing. [Online]. Available: https://www.sciencedirect.com/science/article/pii/S0032386117311175

[15] C. A. Lambert, L. H. Radzilowski, and E. L. Thomas, "Triply periodic level surfaces as models for cubic tricontinuous block copolymer morphologies," *Philosophical Transactions of the Royal Society A: Mathematical, Physical and Engineering Sciences*, vol. 354, no. 1715, p. 2009 – 2023, 1996, cited by: 48. [Online]. Available: https://www.scopus.com/inward/record.uri?eid=2-s2.0-3042891541&doi=10.1098%2frsta.1996.0089&partnerID=40&md5=c9c330c2d7aa7d22af410c88ba29fbad

[16] I. Maskery, N. Aboulkhair, A. Aremu, C. Tuck, and I. Ashcroft, "Compressive failure modes and energy absorption in additively manufactured double gyroid lattices," *Additive Manufacturing*, vol. 16, pp. 24–29, 2017. [Online]. Available: https://www.sciencedirect.com/science/article/pii/S2214860417301203

[17] Z. Chen, Y. Xie, X. Wu, Z. Wang, Q. Li, and S. Zhou, "On hybrid cellular materials based on triply periodic minimal surfaces with extreme mechanical properties," *Materials & Design*, vol. 183, p. 108109, 08 2019.

[18] J. Feng, B. Liu, Z. Lin, and J. Fu, "Isotropic porous structure design methods based on triply periodic minimal surfaces," *Materials & Design*, vol. 210, p. 110050, 2021. [Online]. Available: https://www.sciencedirect.com/science/article/pii/S0264127521006055

[19] H. Zaharin, A.-M. Abdul-Rani, F. Azam, T. Ginta, N. Sallih, A. Ahmad, N. A. Yunus, and T. Z. A. Zulkifli, "Effect of unit cell type and pore size on porosity and mechanical behavior of

additively manufactured ti6al4v scaffolds," *Materials*, vol. 11, p. 2402, 11 2018.

[20] O. Alketan and R. Abu Al-Rub, "Multifunctional mechanical-metamaterials based on triply periodic minimal surface lattices: A review," *Advanced Engineering Materials*, 07 2019.

[21] W. Li, G. Yu, and Z. Yu, "Bioinspired heat exchangers based on triply periodic minimal surfaces for supercritical co2 cycles," *Applied Thermal Engineering*, vol. 179, p. 115686, 2020. [Online]. Available: https://www.sciencedirect.com/science/article/pii/S1359431120331689

[22] S. Torquato and A. Donev, "Minimal surfaces and multifunctionality," *Proceedings of the Royal Society A: Mathematical, Physical and Engineering Sciences*, vol. 460, no. 2047, pp. 1849–1856, 2004. [Online]. Available: www.scopus.com

[23] Z. Dong and X. Zhao, "Application of tpms structure in bone regeneration," *Engineered Regeneration*, vol. 2, pp. 154–162, 2021. [Online]. Available: https://www.sciencedirect.com/science/article/pii/S2666138121000128

[24] S. Zargham, T. Ward, R. Ramli, and I. Badruddin, "Topology optimization: a review for structural designs under vibration problems," *Structural and Multidisciplinary Optimization*, vol. 53, 06 2016.

[25] A. Schumacher, *Optimierung mechanischer Strukturen: Grundlagen und industrielle Anwendungen*, 01 2020.

[26] R. Ansola, J. Canales, J. A. Tárrago, and J. Rasmussen, "An integrated approach for shape and topology optimization of shell structures," *Computers & Structures*, vol. 80, no. 5, pp. 449–458, 2002. [Online]. Available: https://www.sciencedirect.com/science/article/pii/S0045794902000196

[27] L. J. Gibson, "Cellular solids," *MRS Bulletin*, vol. 28, no. 4, p. 270–274, 2003.

[28] L. J. Gibson and M. F. Ashby, *Cellular solids : structure and properties*, 2nd ed., ser. Cambridge solid state science series. Cambridge [u.a.]: Cambridge Univ. Press, 1997.

[29] H. Zhu, J. Hobdell, and A. Windle, "Effects of cell irregularity on the elastic properties of open-cell foams," *Acta materialia*, vol. 48, no. 20, pp. 4893–4900, 2000.

[30] J. Hötzer, A. Reiter, H. Hierl, P. Steinmetz, M. Selzer, and B. Nestler, "The parallel multi-physics phase-field framework pace3d," *Journal of computational science*, vol. 26, pp. 1–12, 2018.

[31] B. Nestler and A. Choudhury, "Phase-field modeling of multi-component systems," *Current Opinion in Solid State and Materials Science*, vol. 15, no. 3, pp. 93–105, 2011, applications of Phase Field Modeling in Materials Science and Engineering.

[32] A. A. Wheeler, W. J. Boettinger, and G. B. McFadden, "Phase-field model for isothermal phase transitions in binary alloys," *Physical Review A*, vol. 45, no. 10, p. 7424, 1992.

[33] E. Schoof, D. Schneider, N. Streichhan, T. Mittnacht, M. Selzer, and B. Nestler, "Multiphase-field modeling of martensitic phase transformation in a dual-phase microstructure," *International Journal of Solids and Structures*, vol. 134, pp. 181–194, 2018.

[34] D. Schneider, F. Schwab, E. Schoof, A. Reiter, C. Herrmann, M. Selzer, T. Böhlke, and B. Nestler, "On the stress calculation within phase-field approaches: a model for finite deformations," *Computational Mechanics*, vol. 60, no. 2, pp. 203–217, 2017.

[35] M. Reder, J. Holland-Cunz, P. Lorson, A. August, and B. Nestler, "Simulative determination of effective mechanical properties for digitally generated foam geometries," *Advanced Engineering Materials*, vol. n/a, no. n/a, p. 2300340, 2023. [Online]. Available: https://onlinelibrary.wiley.com/doi/abs/10.1002/adem.202300340

[36] B. Nestler, H. Garcke, and B. Stinner, "Multicomponent alloy solidification: Phase-field modeling and simulations," *Physical review. E, Statistical, nonlinear, and soft matter physics*, vol. 71, p. 041609, 05 2005.

[37] H. Garcke, B. Nestler, and B. Stoth, "A multiphase field concept: Numerical simulations of moving phase boundaries and multiple junctions," *SIAM Journal on Applied Mathematics*, vol. 60, no. 1, pp. 295–315, 1999. [Online]. Available: https://doi.org/10.1137/S0036139998334895

[38] S. Daubner, P. W. Hoffrogge, M. Minar, and B. Nestler, "Triple junction benchmark for multiphase-field and multi-order parameter models," *Computational Materials Science*, vol. 219, p. 111995, 2023.

[39] A. Prahs, M. Reder, D. Schneider, and B. Nestler, "Thermomechanically coupled theory in the context of the multiphase-field method," *International Journal of Mechanical Sciences*, vol. 257, p. 108484, 2023. [Online]. Available: https://www.sciencedirect.com/science/article/pii/S0020740323003867

[40] S. M. Allen and J. W. Cahn, "A microscopic theory for antiphase boundary motion and its application to antiphase domain coarsening," *Acta Metallurgica*, vol. 27, no. 6, pp. 1085–1095, 1979. [Online]. Available: https://www.sciencedirect.com/science/article/pii/0001616079901962

[41] B. Nestler, F. Wendler, M. Selzer, B. Stinner, and H. Garcke, "Phase-field model for multiphase systems with preserved volume fractions," *Phys. Rev. E*, vol. 78, p. 011604, Jul 2008. [Online]. Available: https://link.aps.org/doi/10.1103/PhysRevE.78.011604

[42] "Mechanical testing of metals - Ductility testing - Compression test for porous and cellular metals," International Organization for Standardization, Geneva, CH, Standard, Dec. 2011.

[43] "Standard test method for compressive properties of rigid cellular plastics," Jan. 2000.

[44] T. M. Ninja, "Sla printing: Its working and technology explained," 2021, accessed: 2024-07-29. [Online]. Available: https://themechninja.com/08/sla-printing-its-working-and-technology-explained/

[45] F. Melchels, "Celebrating three decades of stereolithography," *Virtual and Physical Prototyping*, vol. 7, pp. 173–175, 09 2012.

[46] MATLAB, *version 9.6.0.1072779 (R2019a)*. Natick, Massachusetts: The MathWorks Inc., 2019.

[47] A. John and M. John, "Foam metal and honeycomb structures in numerical simulation," *Annals of the Faculty of Engineering Hunedoara*, vol. 14, no. 4, p. 27, 2016.

[48] G. Planinsic and M. Vollmer, "The surface-to-volume ratio in thermal physics: From cheese cube physics to animal metabolism," *European Journal of Physics*, vol. 29, p. 369, 02 2008.

[49] Ansys, *version 2021 R2*. Canonsburg, Pennsylvania, USA: Ansys Inc., 2021.

[50] A. John and M. John, "The foamed structures in numerical testing," *AIP Conference Proceedings*, vol. 1922, no. 1, p. 050003, 2018. [Online]. Available: https://aip.scitation.org/doi/abs/10.1063/1.5019057

[51] R. Attarzadeh, M. Rovira, and C. Duwig, "Design analysis of the "schwartz d" based heat exchanger: A numerical study," *International Journal of Heat and Mass Transfer*, vol. 177, p.

121415, 2021. [Online]. Available: https://www.sciencedirect.com/science/article/pii/S0017931021005184

[52] Z. Chen, Y. M. Xie, X. Wu, Z. Wang, Q. Li, and S. Zhou, "On hybrid cellular materials based on triply periodic minimal surfaces with extreme mechanical properties," *Materials & Design*, vol. 183, p. 108109, 2019. [Online]. Available: https://www.sciencedirect.com/science/article/pii/S0264127519305477

[53] S. A. Naghavi, M. Tamaddon, A. Marghoub, K. Wang, B. B. Babamiri, K. Hazeli, W. Xu, X. Lu, C. Sun, L. Wang, M. Moazen, L. Wang, D. Li, and C. Liu, "Mechanical characterisation and numerical modelling of tpms-based gyroid and diamond ti6al4v scaffolds for bone implants: An integrated approach for translational consideration," *Bioengineering*, vol. 9, no. 10, 2022. [Online]. Available: https://www.mdpi.com/2306-5354/9/10/504

[54] N. Qiu, J. Zhang, C. Li, Y. Shen, and J. Fang, "Mechanical properties of three-dimensional functionally graded triply periodic minimum surface structures," *International Journal of Mechanical Sciences*, vol. 246, p. 108118, 2023. [Online]. Available: https://www.sciencedirect.com/science/article/pii/S0020740323000206

[55] C. R. C.V. and K. Viswanathan, "The elastic behaviour of isotropic solids," *Proceedings of the Indian Academy of Sciences*, vol. 42, pp. 1–9, 1955.

[56] W. Voigt, "Ueber die beziehung zwischen den beiden elasticitätsconstanten isotroper körper," *Annalen der Physik*,

vol. 274, no. 12, pp. 573–587, 1889. [Online]. Available: https://onlinelibrary.wiley.com/doi/abs/10.1002/andp.18892741206

[57] A. Takezawa, K. Yonekura, Y. Koizumi, X. Zhang, and M. Kitamura, "Isotropic ti–6al–4v lattice via topology optimization and electron-beam melting," *Additive Manufacturing*, vol. 22, pp. 634–642, 2018. [Online]. Available: https://www.sciencedirect.com/science/article/pii/S2214860418300629

[58] S. Hällgren, L. Pejryd, and J. Ekengren, "3d data export for additive manufacturing - improving geometric accuracy," *Procedia CIRP*, vol. 50, pp. 518–523, 12 2016.

[59] M. Ashby, T. Evans, N. Fleck, J. Hutchinson, H. Wadley, and L. Gibson, *Metal Foams: A Design Guide*. Elsevier Science, 2000. [Online]. Available: https://books.google.de/books?id=C0daIBo6LjgC

[60] D. Li, W. Liao, N. Dai, and Y. M. Xie, "Comparison of mechanical properties and energy absorption of sheet-based and strut-based gyroid cellular structures with graded densities," *Materials*, vol. 12, no. 13, 2019. [Online]. Available: https://www.mdpi.com/1996-1944/12/13/2183

[61] C. Lu, C. Zhang, P. Wen, and F. Chen, "Mechanical behavior of al–si10–mg gyroid surface with variable topological parameters fabricated via laser powder bed fusion," *Journal of Materials Research and Technology*, vol. 15, pp. 5650–5661, 2021. [Online]. Available: https://www.sciencedirect.com/science/article/pii/S2238785421012874

[62] K. Nelson, C. N. Kelly, and K. Gall, "Effect of stress state on the mechanical behavior of 3d printed porous ti6al4v scaffolds produced by laser powder bed fusion," *Mater Sci Eng B Solid State Mater Adv Technol*, vol. 286, p. 116013, 2022. [Online]. Available: https://www.sciencedirect.com/science/article/pii/S0921510722004019

[63] D. Qin, L. Sang, Z. Zhang, S. Lai, and Y. Zhao, "Compression performance and deformation behavior of 3d-printed pla-based lattice structures," *Polymers*, vol. 14, no. 5, 2022. [Online]. Available: https://www.mdpi.com/2073-4360/14/5/1062

[64] O. Gülcan, U. Simsek, O. Cokgunlu, M. Özdemir, P. Şendur, and G. G. Yapici, "Effect of build parameters on the compressive behavior of additive manufactured cocrmo lattice parts based on experimental design," *Metals*, vol. 12, no. 7, 2022. [Online]. Available: https://www.mdpi.com/2075-4701/12/7/1104

List of own publications

[1] L. Wallat, M. Selzer, U. Wasmuth, F. Poehler, and B. Nestler, "Energy absorption capability of graded and non-graded sheet-based gyroid structures fabricated by microcast processing," Journal of Materials Research and Technology, vol. 21, pp. 1798–1810, 2022. [Online]. Available: https://www.sciencedirect.com/science/article/pii/S2238785422015009

[2] L. Wallat, P. Altschuh, M. Reder, B. Nestler, and F. Poehler, "Computational design and characterisation of gyroid structures with different gradient functions for porosity adjustment," Materials, vol. 15, no. 10, 2022. [Online]. Available: https://www.mdpi.com/1996-1944/15/10/3730

[3] L. Wallat, M. Reder, M. Selzer, F. Poehler, and B. Nestler, "Shape optimization of porous structures by phase-field modeling with strain energy density reduction," Materials Today Communications, vol. 37, p. 107018, 2023. [Online]. Available: https://www.sciencedirect.com/science/article/pii/S2352492823017099

[4] L. Wallat, A. Koeppe, M. Selzer, M. Seiler, F. Poehler, and B. Nestler, "Experimental evaluation of phase-field-based load-specific shape optimization of nature-inspired porous structures," Materials Today Communications, vol. 38, p. 108088, 2024. [Online]. Available: https://www.sciencedirect.com/science/arti

cle/pii/S2352492824000680
[5] L. Wallat, N. Kersch, M. Reder, M. Selzer, M. Seiler, F. Poehler, and B. Nestler, "Phase-field based shape optimization of uni- and multiaxially loaded nature-inspired porous structures while maintaining characteristic properties." Discover Mechanical Engineering, 2024.
[6] **In Review:** L. Wallat, M. Selzer, M. Seiler, F. Poehler, and B. Nestler, "Phase-field based load-specific structural optimization of sheet-based gyroid-structures."
[7] **In Review:** L. Wallat, M. Reder, M. Selzer, M. Seiler, F. Poehler, and B. Nestler, "Phase-field based structural optimization of 3d cross-lattice structure to lightweight periodic lattice structures."